ANALYSIS OF ELASTIC AND ELECTRICAL FIELDS IN QUANTUM STRUCTURES BY NOVEL GREEN'S FUNCTIONS AND RELATED BOUNDARY INTEGRAL METHODS

A Dissertation

Presented to

The Graduate Faculty of The University of Akron

In Partial Fulfillment

of the Requirements for the Degree

Doctor of Philosophy

Yan Zhang

December, 2010

Report Documentation Page

Form Approved
OMB No. 0704-0188

1. REPORT DATE	2. REPORT TYPE	3. DATES COVERED
DEC 2010		**00-00-2010 to 00-00-2010**

4. TITLE AND SUBTITLE	5a. CONTRACT NUMBER
Analysis of Elastic and Electrical Fields in Quantum Structures by Novel Green's Functions and Related Boundary Integral Methods	5b. GRANT NUMBER
	5c. PROGRAM ELEMENT NUMBER
6. AUTHOR(S)	5d. PROJECT NUMBER
	5e. TASK NUMBER
	5f. WORK UNIT NUMBER
7. PERFORMING ORGANIZATION NAME(S) AND ADDRESS(ES) **University of Akron,The University of Akron,Akron,OH,44325**	8. PERFORMING ORGANIZATION REPORT NUMBER
9. SPONSORING/MONITORING AGENCY NAME(S) AND ADDRESS(ES)	10. SPONSOR/MONITOR'S ACRONYM(S)
	11. SPONSOR/MONITOR'S REPORT NUMBER(S)

12. DISTRIBUTION/AVAILABILITY STATEMENT
Approved for public release; distribution unlimited

13. SUPPLEMENTARY NOTES

14. ABSTRACT

Quantum structures made of components with at least one dimension being at nanoscale, show great potential for future optoelectronic device applications. The elastic fields in quantum structures affect their physical and mechanical properties, and also play a significant role in their fabrication. Therefore, it is crucial that the induced elastic fields in quantum structures be modeled accurately and efficiently. In Chapter II, a rigorous analysis on the elastic and electric fields in 2-dimensional quantum wire (QWR) structures is presented using the novel Green?s functions and related boundary element method (BEM). The elastic and electric fields in embedded QWR structures for both the inclusion and inhomogeneity models are investigated. The electric field distribution in polygonal QWRs with different sides is also studied and it is found that the electric field in triangle and square QWRs can be very different to those in polygonal QWRs with sides larger than 4. In Chapter III, a bimaterial BEM is developed for the calculation of the strain energy density and the relative strain energy in free-standing/embedded QWR structures. The required bimaterial Green?s functions are derived in terms of the Stroh formalism. The boundary of the QWR is discretized with constant elements for which the involved Green?s function kernels can be exactly integrated. We found that the magnitude of the relative strain energy increases with increasing depth of the QWR with respect to the surface of the substrate. Strain energy density inside the QWR is also plotted to show its close relation to the QWR shape. In Chapter IV, an analytical method for calculating the 3-dimensional quantum dot (QD) induced elastic field in the half-space substrate is presented. The QD is assumed to be of any polyhedral shape, and its surface is approximated efficiently in terms of a number of flat triangles so that the Green?s function kernels can be integrated analytically over the flat triangles. Numerical examples are presented for cubic, pyramidal, truncated pyramidal and point QDs in half-space substrate. The strain energy distribution on the surface of the substrate indicates clearly the strong influence of the QD shape and position on the induced strain energy. This long-range strain energy on the surface is the main source for controlling and modulating the overgrown QD pattern and size. At last, a detailed theoretical calculation of the elastic and electric fields in and around nitride-based QDs which are buried in anisotropic half-space substrate is developed. Results are presented for a single dot as well as coupled dots. We consider in detail the case of AlN QDs in the shape of hexagonal truncated-pyramids. The calculated strain and piezoelectric

15. SUBJECT TERMS

16. SECURITY CLASSIFICATION OF:			17. LIMITATION OF ABSTRACT	18. NUMBER OF PAGES	19a. NAME OF RESPONSIBLE PERSON
a. REPORT	b. ABSTRACT	c. THIS PAGE			
unclassified	**unclassified**	**unclassified**	**Same as Report (SAR)**	**113**	

ANALYSIS OF ELASTIC AND ELECTRICAL FIELDS IN QUANTUM STRUCTURES BY NOVEL GREEN'S FUNCTIONS AND RELATED BOUNDARY INTEGRAL METHODS

Yan Zhang

Dissertation

Approved:	Accepted:
_____	_____
Advisor Dr. Ernian Pan	Department Chair Dr. Wieslaw K. Binienda
_____	_____
Committee Member Dr. Atef. F Saleeb	Dean of the College Dr. George K. Haritos
_____	_____
Committee Member Dr. Wieslaw K. Binienda	Dean of the Graduate School Dr. George R. Newkome
_____	_____
Committee Member Dr. Alex Povitsky	Date
_____	
Committee Member Dr. Kevin L. Kreider	

ABSTRACT

Quantum structures made of components with at least one dimension being at nanoscale, show great potential for future optoelectronic device applications. The elastic fields in quantum structures affect their physical and mechanical properties, and also play a significant role in their fabrication. Therefore, it is crucial that the induced elastic fields in quantum structures be modeled accurately and efficiently.

In Chapter II, a rigorous analysis on the elastic and electric fields in 2-dimensional quantum wire (QWR) structures is presented using the novel Green's functions and related boundary element method (BEM). The elastic and electric fields in embedded QWR structures for both the inclusion and inhomogeneity models are investigated. The electric field distribution in polygonal QWRs with different sides is also studied and it is found that the electric field in triangle and square QWRs can be very different to those in polygonal QWRs with sides larger than 4.

In Chapter III, a bimaterial BEM is developed for the calculation of the strain energy density and the relative strain energy in free-standing/embedded QWR structures. The required bimaterial Green's functions are derived in terms of the Stroh formalism. The boundary of the QWR is discretized with constant elements for which the involved Green's function kernels can be exactly integrated. We found that the magnitude of the relative strain energy increases with increasing depth of the QWR with respect to the

surface of the substrate. Strain energy density inside the QWR is also plotted to show its close relation to the QWR shape.

In Chapter IV, an analytical method for calculating the 3-dimensional quantum dot (QD) induced elastic field in the half-space substrate is presented. The QD is assumed to be of any polyhedral shape, and its surface is approximated efficiently in terms of a number of flat triangles so that the Green's function kernels can be integrated analytically over the flat triangles. Numerical examples are presented for cubic, pyramidal, truncated pyramidal and point QDs in half-space substrate. The strain energy distribution on the surface of the substrate indicates clearly the strong influence of the QD shape and position on the induced strain energy. This long-range strain energy on the surface is the main source for controlling and modulating the overgrown QD pattern and size.

At last, a detailed theoretical calculation of the elastic and electric fields in and around nitride-based QDs which are buried in anisotropic half-space substrate is developed. Results are presented for a single dot as well as coupled dots. We consider in detail the case of AlN QDs in the shape of hexagonal truncated-pyramids. The calculated strain and piezoelectric potential distributions induced by a single QD are presented. Large piezoelectric potential can be observed in the structures. The results are compared to those of simplified model in which the QD is assumed to be a point. Very similar trends are observed. Strain and piezoelectric potential distributions induced by coupled QDs are also shown along line scans or on the surface.

ACKNOWLEDGEMENTS

This thesis can be considered as the end journey of my PhD life in Civil Engineering, The University of Akron. There are many people who have contributed in many ways during my PhD period of life. It's my pleasure to have this chance to express my deepest gratitude to all of them.

Thanks to my PhD committee members: Prof. Ernian Pan (Chair), Prof. Wieslaw K. Binienda, Prof. Kevin L. Kreider, Prof. Alex Povitsky and Prof. Atef F. Saleeb (in alphabetical order) for their time and helpful suggestions.

Thanks to my colleagues, Dr. Ronghua Zhu, Prof. Xiaojuan Liu, James Ramsey, Mingkun Sun, Yuanguo Chen, Ruifeng Wang and Yu Zou, for their useful discussions and for giving me the nice and inspiring working atmosphere.

Thanks to my family for giving me encouragement and energy to finish this dissertation.

Special thanks to Army research office for their kind and generous support.

TABLE OF CONTENTS

Page

LIST OF TABLES

LIST OF FIGURES

Figure Page

CHAPTER I

BACKGROUND

1.1 Introduction and Motivation

Quantum confined nanostructures have drawn great attention due to their potential application in the fabrication of a wide variety of optoelectronic, microelectronic and fluorescence devices, such as photovoltaic cells, light emitting diodes and quantum semiconductor lasers.

1.1.1 Carrier Confinement

Quantum confined structures include quantum well (QW), quantum wire (QWR) and quantum dot (QD) (shown in Figure 1.1), of which, the QWR and QD are the most popular topics and they are also the center subjects of this thesis. A key feature of these structures is carrier confinement (electrons or holes are trapped in a region with typical dimensions ranging from a few nanometers to several hundred nanometers):

1. Quantum wells, which confine electrons or holes in one dimension and allow free propagation in two dimensions.
2. Quantum wires, which confine electrons or holes in two spatial dimensions and allow free propagation in the third.
3. Quantum dots, which confine electrons or holes in all three spatial dimensions.

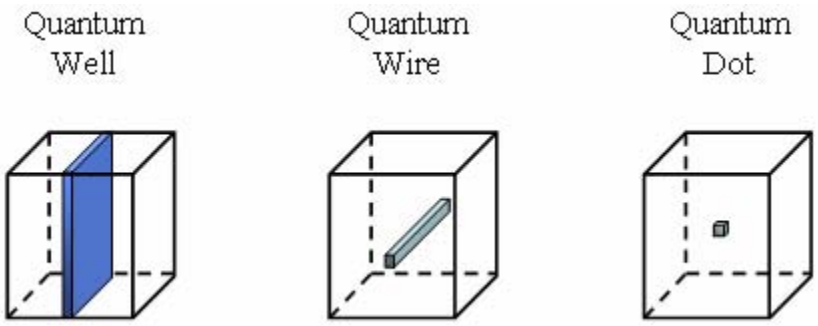

Figure 1.1 Schematic illustrations for QW, QWR and QD

The capability to confine carriers is based on a difference in bandgap between two materials (shown in Fig. 1.1 the blue material and its surrounding material) that are brought in contact with each other. Fig. 1.2 shows the bandgap difference between different materials. Free electrons and holes preferentially stay in the material with the lowest bandgap, where their potential energy is minimal. The idea of reducing dimensionality (Fig. 1.1) is leading to increasing confinement. This reduction of dimensionality is directly reflected in the density of states, as shown in Fig. 1.3. The density of states has very different shapes as a function of energy depending on the reduction of the dimensionality: the density of states in a QW system has a step function; the density of states in a QWR system has an inverse energy relationship. Of all these quantum structures, QDs comprise the ultimate in carrier confinement, trapping electrons and holes in all three spatial dimensions. It is this fundamental property that gives rise to the discrete energy spectrum and the density of states in QD system is continuous and independent of energy.

The strain field in quantum structures can change the bandgap, cause trapping of holes and electrons, and also cause electrical fields in some piezoelectric materials. In short,

strain is a crucial factor to impact the electronic and hence the optoelectronic properties in quantum based devices.

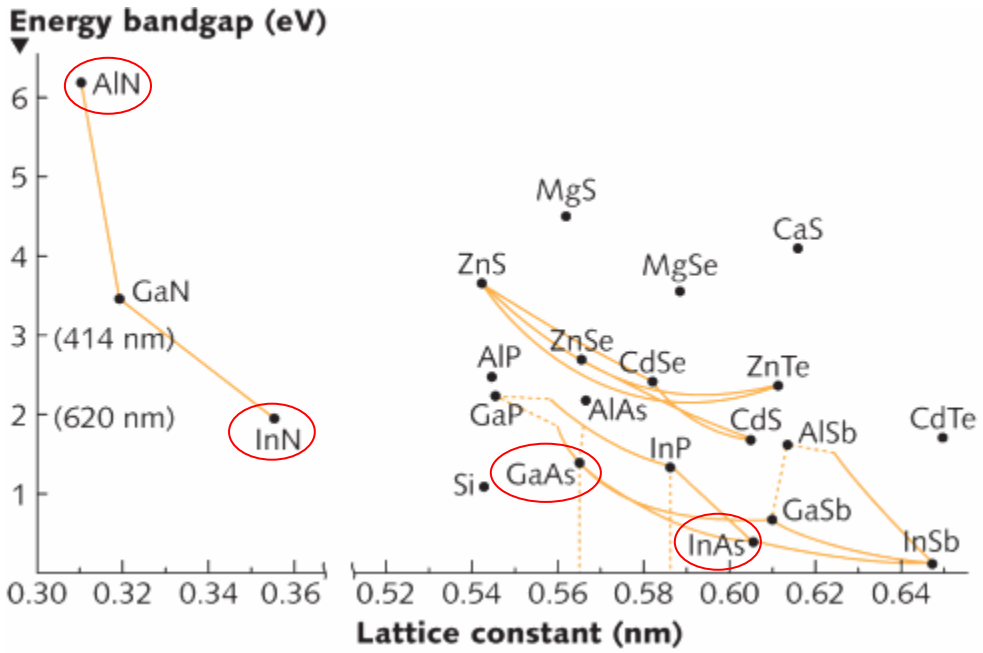

Figure 1.2 Bandgap energy and lattice constant for different materials

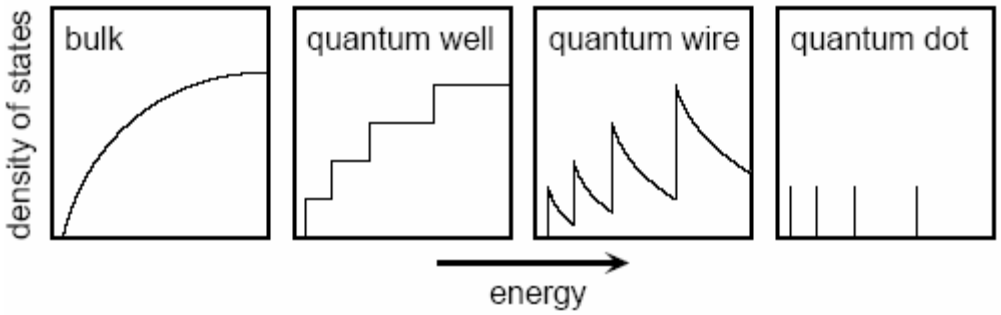

Figure 1.3 Density of states for bulk material, QW, QWR and QD.

1.1.2 Fabrication of Quantum Structures

In general, quantum structures are fabricated with an intrinsic elastic field arising from the lattice mismatch between the quantum island and substrate material. Take the InAs

quantum dots on GaAs substrate as an example. The lattice constant for InAs is a_{InAs}=6.058 Å, while GaAs is a_{GaAs}=5.653 Å (Figure 1.4). Their natural lattice constants difference is the so-called misfit strain which can be calculated as $\gamma_{ij}^{*} = \frac{a_{GaAs} - a_{InAs}}{a_{InAs}} \delta_{ij} \equiv \gamma_0 \delta_{ij}$. Therefore, for InAs/GaAs quantum system, the misfit strain is around 7%.

When a material is deposited on another material (substrate) with different bandgap and lattice constant, the difference in lattice constant induces strain between the two materials. Spontaneous strain relaxation lowers the potential energy of this system, and leads to the formation of islands on the substrate (Fig. 1.5). QDs/QWRs grown by this process are usually called 'self-organized' QDs/QWRs. In the growth process, the strain plays a key role in determining the size uniformity and the spatial ordering of the deposited material.

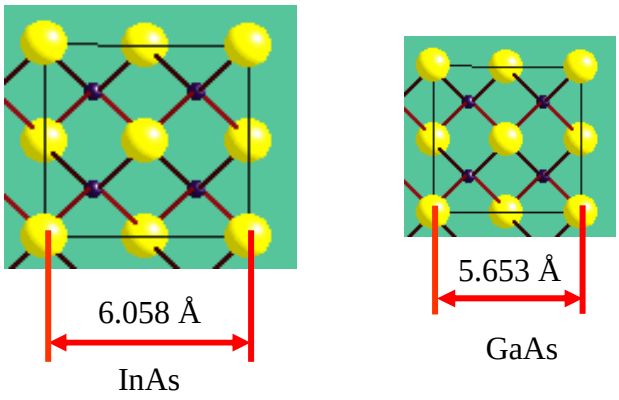

Figure 1.4 Lattice constants for InAs and GaAs

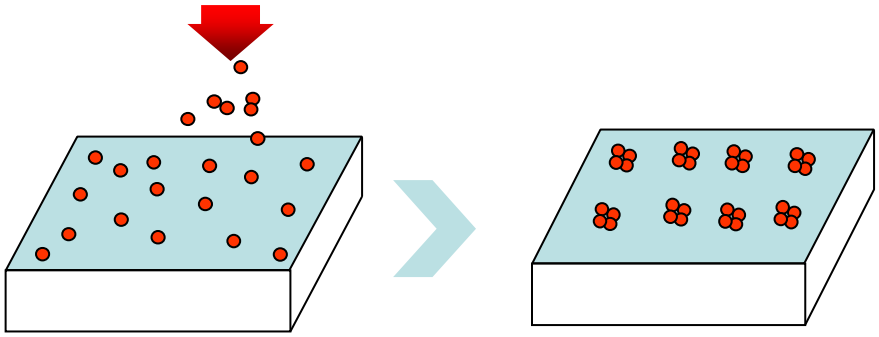

Figure 1.5 Schematic representation of quantum dots growth.

In this thesis, we have used two typical crystal lattice structures (Fig. 1.6) which are representative for many quantum structures: The cubic structure and the hexagonal structure. The latter has a huge built-in electric field.

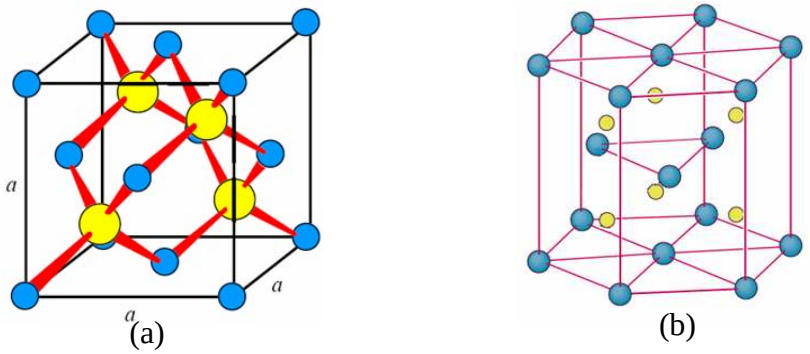

Figure 1.6 Two typical crystal structures: (a) cubic and (b) hexagonal

1.2 Literature Review

It is well known that the elastic and electric fields in quantum structures substantially modify the electronic band structure and thus strongly affect the performance of the electronic devices. One could control/optimize the electronic and optical properties of quantum structures by altering the elastic and electric fields [Con00, Med02, Not95]. Also, a detailed knowledge of the strain field can serve as a useful tool to understand the growth of these structures in order to control the size, shape and distribution of the

wires/dots, to achieve good repeatability. Hence, it is crucial that the induced elastic and electric fields should be modeled accurately and efficiently in order to obtain a well ordered quantum structure and to improve the performance of the electronic devices.

Mathematical and numerical simulations play an important role in the study of quantum confined nanostructures. At the research point of view for exploring the physics, computational simulation is an instrument in interpreting related data and guiding for future developments. At the engineering stage of optimization, it can provide quantitative analysis quickly and economically.

There are a variety of techniques been developed by many researchers to study the elastic and electric fields in the quantum nanostructures, such as the finite element method (FEM) and finite difference method [Ben96, Kre99, Pei03, Gru95, Liu02, Jon06], atomistic approach [Pry98, Cal00, Kik01, Mak01], continuum approaches [Jog00, Gla01, Zha05]. Jiang and Singh determined the strain field for InAs QD embedded in GaAs substrate using a valence force field model (one of the atomistic models) [Jia98]. But when a large number of atoms are required for accuracy in the study, this method appears computationally intensive and subjects to convergence problems. Furthermore, the atomistic approach depends crucially on the quality of the interatomic potential model. The key advantage for this technique is that displacements are evaluated at the atomistic level which can provide potentially greater accuracy than other methods at the QD edges and the QD/substrate interface.

The FEM approach is the most commonly used method in engineering fields. Grundmann et al used the FEM to analyze a pyramidal dot [Gru95]. Pei et al. investigated the elastic fields in the self-organized quantum dot structures by a three-dimensional

FEM [Pei03]. Liu et al., also using the FEM, reported the stress and strain of the heterosystem of InAs quantum dots embedded in GaAs [Liu02]. Jonsdottir et al used the FEM to assess the effect of lattice mismatch, dot volume and dot surface contact area on the induced stresses and elastic energies [Jon06]. The FEM approach could be also computationally intensive since it requires discretization of the problem domain.

Analytical continuum methods for calculating the strain distribution induced by a uniformly lattice mismatched inclusion were based on the classic work of Eshelby [Esh57]. Elastic field induced by QDs are determined by performing an integral over the surface of QDs. Davies extended the elastic field evaluation to electroelastic field and determined the piezoelectric potential [Dav98]. The advantages of the analytical continuum methods are quick and portable, and accurate. However, there are some restrictions associated with them. These include assumption of isotropic material properties, same properties for both QD and substrate, and of the infinite substrate.

It is well-known that any pure continuum method cannot account for atomistic scale distortion. Andreev et al. then proposed an exact analytical solution for the lattice relaxation associated with a variation of lattice constant [And99]. The analytical solutions, in particular those related to the Green's function solutions, have been developed and applied to the quantum structure modeling [Pan01]. Because of their accuracy and efficiency, these analytical methods, particularly the Green's function method, could be more appealing to experimentalists and physical device designers in the studies of quantum structures [Pea00]. More recently, the multiscale Green's functions have been also introduced to model QD induced strain field [Yan05, Rea07], which has been shown to be very computationally efficient.

From the above literature review, it can be concluded that at least one or more of the following simplifications are made through the calculations.

1. Purely elastic field. Most previous studies considered only the strain field in the quantum structures although the electric field is also a crucial factor.
2. An infinite substrate. Most previous analyses assumed that the QD was buried in an infinite matrix although the QD could be buried immediately below a free surface.
3. A single isolated quantum wire or dot.
4. A simple shaped quantum wire or dot.

Recently, Pan [Pan02c] has employed the equivalent body-force concept of Eshelby inclusion problem [Esh57, Mur87] and succeeded in extending the Green's function approach to anisotropic substrates [Jog03, Pan01, Pan02a, Pan02b, Yan03]. The new Green's function takes into account quantum wire or dot of arbitrary shape and substrate with the most general class of anisotropy and piezoelectricity. In this thesis, we use the extended Green's function and the corresponding BEM to study the elastic and electric fields in or around quantum wire or dot systems.

1.3 Thesis Outline

The thesis is organized as follows: In Chapter II we propose a simple BEM formulation to investigate the elastic and electric fields in QWR structures. In Chapter III the bimaterial Green's functions in anisotropic elastic media are derived in terms of the Stroh formalism. The strain energy density and the relative strain energy in free-standing QWR or in QWR embedded in half-space substrate are calculated. An analytical method

for calculating the QD-induced strain fields in half-space substrates are presented in Chapter IV. In Chapter V, a detailed calculation of the elastic and electric fields in and around nitride-based QDs is developed. Finally, the conclusions and contributions of this research, as well as future research opportunities are discussed in Chapter VI.

CHAPTER II

ELASTIC AND ELECTRIC FIELDS INDUCED BY QWR IN FULL-PLANE: INCLUSION VS. INHOMOGENEITY

2.1 Summary

The well-known Eshelby inclusion method [Esh57] has been successfully applied to study the induced elastic and electric fields in QWR structures. In this treatment the lattice misfit between the QWR and substrate is allowed but the QWR material is assumed to be the same as its substrate [Fau96, Dav98, Ru00, Gla03, Pan04, Mar06]. The most advantage of the Eshelby inclusion method is its simplicity by which the induced fields can be estimated analytically.

Recently, the accuracy of the inclusion model has been studied using the inhomogeneity model. Different material property for the QWR and substrate was applied [Yan02, Pan05], instead of assuming the same material property. For instance, the issue of the homogeneous inclusion vs. inhomogeneity in the context of QWR structures was studied in detail for the purely elastic structures by Pan et al [Pan05]. Numerical examples were given for InAs/GaAs QWR structures in both (001) and (111) growth directions for QWRs in shape of square and trapezoid. There are some main observations from their analysis: (i) In the substrate and far away from the QWR, both the inclusion and inhomogeneity models give similar results. (ii) For points within or near

the QWR, the difference between the inclusion and inhomogeneity models can be as high as 10% for these materials. (iii) Although the singular behavior near the corners of the QWR looks similar for both the inclusion and inhomogeneity models, the amplitudes of the singularity are different. So far, however, the difference on the electric field based on both the inclusion and inhomogeneity in the corresponding InAs/GaAs (111) QWRs and in QWR made of any nitride III group material has not been reported in any literature, which is the main motivation of this study.

This chapter is organized as follows. In Section 2.2, we describe the associated basic equations. In Section 2.3, we present the problem to be solved. In Section 2.4, the BEM and the corresponding constant element discretization are presented. While in Section 2.5 we present various numerical examples, conclusions are drawn in Section 2.6.

2.2 Basic Equations

The basic equations for a linear and generally anisotropic piezoelectric solid under a static deformation condition conclude the constitutive relations

$$\sigma_{ij} = C_{ijmn}\gamma_{mn} - e_{kij}E_k \tag{2.1a}$$

$$D_i = e_{ijk}\gamma_{jk} + \varepsilon_{ij}E_j \tag{2.1b}$$

where σ_{ij} is stress and D_i is electric displacement; γ_{ij} is strain and E_i is electric field; C_{ijmn}, e_{ijk} and ε_{ij} are elastic moduli, the piezoelectric constants and dielectric constants respectively.

The strain-displacement relations

$$\gamma_{ij} = \frac{1}{2}(u_{i,j} + u_{j,i}) \tag{2.2}$$

$$E_i = -\phi_{,i} \tag{2.3}$$

where u_i and Φ are the elastic displacement and electric potential respectively. And the equilibrium equations

$$\sigma_{ij,i} + f_j = 0 \tag{2.4}$$

$$D_{i,i} - q = 0 \tag{2.5}$$

where f_i and q are body force and electric charge respectively.

For the seek of convenience, we adopt the extended notations for the stress and electric displacement, elastic strain and electric field, elastic displacement and electric potential, body force and electric charge, and all the three kinds of material constants in piezoelectric problems [Bar75, Dun93] as

$$\sigma_{iJ} = \begin{cases} \sigma_{ij}, & J = j = 1, 2, 3 \\ D_i, & J = 4 \end{cases} \tag{2.6}$$

$$\gamma_{Ij} = \begin{cases} \gamma_{ij}, & I = 1, 2, 3 \\ -E_j, & I = 4 \end{cases} \tag{2.7}$$

$$u_I = \begin{cases} u_i, & I = i = 1, 2, 3 \\ \phi, & I = 4 \end{cases} \tag{2.8}$$

$$F_I = \begin{cases} f_i, & I = i = 1, 2, 3 \\ -q, & I = 4 \end{cases} \tag{2.9}$$

$$C_{iJKl} = \begin{cases} C_{ijkl}, & J,K = j,k = 1,2,3 \\ e_{lij}, & J = j = 1,2,3;\ K = 4 \\ e_{ikl}, & J = 4;\ K = k = 1,2,3 \\ -\varepsilon_{il}, & J = K = 4 \end{cases} \tag{2.10}$$

In this definition, it can be noted that the original symbols are kept just with the fourth components related to electric fields. In terms of this extended notation, the constitutive relations can be simplified to a single equation

$$\sigma_{iJ} = C_{iJKl}\gamma_{Kl} \tag{2.11}$$

Similarly, the equilibrium equations can be unified as

$$\sigma_{iJ,i} + F_J = 0 \tag{2.12}$$

2.3 Problem Description for QWR in Full-plane

Consider a general QWR problem, which is illustrated in Figure 2.1. The QWR can be arbitrarily shaped. Let us assume that the general misfit strain γ_{Ij}^{*} (I=1,2,3,4 and j=1,2,3) is uniform within the QWR domain and is zero outside.

The total extended strain is the sum of

$$\gamma_{Ij} = \gamma_{Ij}^{e} + \gamma_{Ij}^{*} \tag{2.13}$$

where γ_{Ij}^{e} the extended strain that appears in the generalized constitutive relation in Eq. (2.11) as

$$\sigma_{iJ} = C_{iJKl}\gamma_{Kl}^{e} \tag{2.14a}$$

or

$$\sigma_{iJ} = C_{iJKl}(\gamma_{Kl} - \chi\gamma_{Kl}^{*}) \tag{2.14b}$$

In Eq. (2.14), χ is equal to 1 if the observation point is within the QWR domain *V* and to 0 outside.

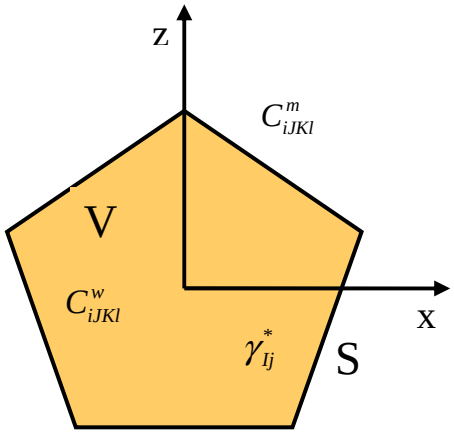

Figure 2.1 An arbitrarily shaped polygon QWR inclusion/inhomogeneity with eigenstrain γ^*_{Ij} in an anisotropic substrate.

The interface between the QWR and matrix is labeled *s*. We also denote C^w_{iJKl} and C^m_{iJKl} as the general moduli of the QWR and matrix materials, respectively (Figure 2.1). For the homogeneous inclusion problem, $C^w_{iJKl} = C^m_{iJKl}$.

Assuming that there is no body force and electric charge within the QWR system, one can easily show that, for the matrix domain,

$$C^m_{iJKl} u^m_{K,li} = 0 \tag{2.15}$$

and for the QWR domain,

$$C^w_{iJKl} u^w_{K,li} = C^w_{iJKl} \gamma^*_{Kl,i} \tag{2.16}$$

It is clear that the right hand side of Eq. (2.16) is equivalent to a body force defined as

$$f^{(w)}_J = -C^w_{iJKl} \gamma^*_{Kl,i} \tag{2.17}$$

which is also called the equivalent body force of the eigenstrain [Mur87, Pan04a]. This equivalent body force will be employed in the next section to convert the contribution of the eigenstrain to a boundary integral along the interface of the QWR and its substrate. Again, the superscripts *m* and *w* denote quantities associated with the matrix and QWR, respectively.

2.4 Boundary Integral Equations in Terms of Green's Function

To solve the problem in Figure 2.1, BEM is applied to both the QWR and its matrix/substrate. The boundary integral formulation can be expressed as [Yan02, Pan05]

$$b_{IJ}(\mathbf{X})u_J^m(\mathbf{X}) = \int_S \left[U_{IJ}^m(\mathbf{X},\mathbf{x})t_J^m(\mathbf{x}) - T_{IJ}^m(\mathbf{X},\mathbf{x})u_J^m(\mathbf{x})\right]ds(\mathbf{x}) \tag{2.18}$$

for the matrix, and

$$b_{IJ}(\mathbf{X})u_J^w(\mathbf{X}) = \int_S \left[U_{IJ}^w(\mathbf{X},\mathbf{x})\left(t_J^w(\mathbf{x}) + f_J^w(\mathbf{x})\right) - T_{IJ}^w(\mathbf{X},\mathbf{x})u_J^w(\mathbf{x})\right]ds(\mathbf{x}) \tag{2.19}$$

for the QWR.

In Eqs. (2.18) and (2.19), $\boldsymbol{x}(x, z)$ and $\boldsymbol{X}(X, Z)$ are the coordinates of the field and source points. Coefficients b_{IJ} is equal to δ_{IJ} if $\boldsymbol{X}$ is an interior point and $\frac{1}{2}\delta_{IJ}$ at a smooth boundary point. For points at complicated geometry locations, these coefficients can be determined by the rigid-body motion method [Bre92]. t_J and u_J are the traction and displacement components, respectively. Furthermore, in Eq. (2.19), f_J^w is the traction induced by the misfit eigenstrain inside the QWR whose expression is given by Eq. (2.17).

The Green's functions U_{IJ} and T_{IJ} in Eqs. (2.18) and (2.19) are taken to be the special 2D Green's functions for the full plane [Tin96, Pan02a]. The indexes *I* and *J* indicate the *J*-th Green's (general) displacement/traction (at $\boldsymbol{x}$) in response to a (general) line-force in the *I*-th direction (applied at $\boldsymbol{X}$). Note that the Green's functions are in exact closed form, and thus their integration over constant elements can be carried out exactly as discussed below. This is computationally desirable as it is very efficient and accurate for the calculation.

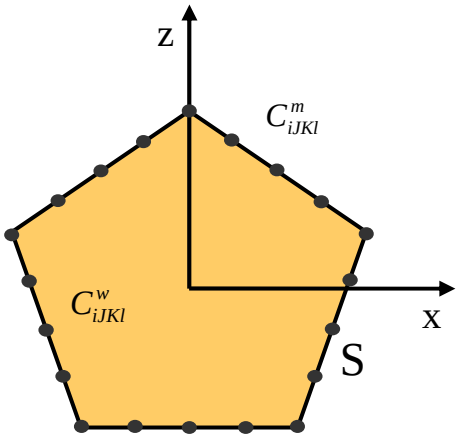

Figure 2.2 QWR boundary discretization

To employ the above Green's Functions, we divide the boundary of QWR into *N* segments with the *n*-th element being labeled as s_n (shown in figure 2.2). The constant values u_{Jn} and t_{Jn} on the *n*-th element equal to the displacement and traction at the center of the element. Under this assumption, the boundary integral equations (2.18) and (2.19) for the surrounding matrix and QWR domains are reduced to the following algebraic equations

$$b_{IJ}u_J^m + \sum_{n=1}^{N}\left(\int_{s_n} T_{IJ}^m ds\right)u_{Jn}^m = \sum_{n=1}^{N}\left(\int_{s_n} U_{IJ}^m ds\right)t_{Jn}^m \tag{2.20}$$

for the matrix, and

$$b_{IJ}u_J^w + \sum_{n=1}^{N}(\int_{s_n} T_{IJ}^w ds)u_{Jn}^w = \sum_{n=1}^{N}(\int_{s_n} U_{IJ}^w ds)(t_{Jn}^w + C_{pJKl}^w \gamma_{Kl}^* n_p) \tag{2.21}$$

for the QWR.

It is obvious that the difference between Eqs. (2.20) and (2.21) is the traction induced by the misfit eigenstrain inside the QWR in Eq. (2.21).

The problem now is reduced to find the suitable Green's functions U_{IJ} and T_{IJ}, as well as their integrals over each element s_n, which are the kernel functions in these equations. We now present the analytical integration of these Green's functions over an arbitrary constant element.

To carry out the line integration of the Green's functions over a constant element, we first look at the Green's functions appeared in Eqs. (2.20) and (2.21). They can be simply expressed as [Pan04b, Tin96, Pan02b]

$$U_{IJ}(\boldsymbol{x}, \boldsymbol{X}) = \frac{1}{\pi}\mathrm{Im}\{A_{JR}\ln(z_R - s_R)A_{IR}\} \tag{2.22}$$

$$T_{IJ}(\boldsymbol{x}, \boldsymbol{X}) = \frac{1}{\pi}\mathrm{Im}\left\{B_{JR}\frac{p_R n_1 - n_3}{z_R - s_R}A_{IR}\right\} \tag{2.23}$$

where "Im" stands for the imaginary part of the complex value, A_{IJ} and B_{IJ} are two constant matrices related to the material property only [Tin96], n_1 and n_3 are the unit outward normal along x- and z-directions, p_R (R=1,2,3,4) are the Stroh eigenvalues, and $z_R=x+p_R z$ and $s_R=X+p_R Z$ are related to the field $\boldsymbol{x}(x, z)$ and source $\boldsymbol{X}(X, Z)$ points, respectively.

The Stroh eigenvalues and eigenmatrices involved in Eqs. (2.22) and (2.23) are obtained by solving the following equations. The eigenvalue p and the corresponding eigenvector a are solved from the equation

$$[\boldsymbol{Q} + p(\boldsymbol{R} + \boldsymbol{R}^T) + p^2\boldsymbol{T}]\boldsymbol{a} = 0 \tag{2.24}$$

where the superscript T denotes matrix transpose. And

$$Q_{IJ}=C_{1IJ1},\ R_{IJ}=C_{1IJ3},\ T_{IJ}=C_{3IJ3} \tag{2.25}$$

where C_{iJKl} are the elastic and electric moduli defined in Eq. (2.10).

After we get eigenvector **a**, the eigenvector **b** can be obtained from

$$\boldsymbol{b} = (\boldsymbol{R}^T + p\boldsymbol{T})\boldsymbol{a} = -\frac{1}{p}(\boldsymbol{Q} + p\boldsymbol{R})\boldsymbol{a} \tag{2.26}$$

Denoting by p_k, $\boldsymbol{a}_k$ and $\boldsymbol{b}_k$ (k=1,2,3,…,8) the eigenvalues and associated eigenvectors, we order them in such a way so that

$$\text{Im } p_I>0,\ \ p_{I+4} = \overline{p}_I\ ,\ \boldsymbol{a}_{I+4} = \overline{\boldsymbol{a}}_I\ ,\ \boldsymbol{b}_{I+4} = \overline{\boldsymbol{b}}_I\ \ (\text{I}=1,2,3,4) \tag{2.27}$$

where an overbar denotes the complex conjugate, and the matrices **A** and **B** are

$$\boldsymbol{A}=[\boldsymbol{a}_1,\boldsymbol{a}_2,\boldsymbol{a}_3,\boldsymbol{a}_4],\ \boldsymbol{B}=[\boldsymbol{b}_1,\boldsymbol{b}_2,\boldsymbol{b}_3,\boldsymbol{b}_4] \tag{2.28}$$

We assume that p_I are distinct eigenvalues, $\boldsymbol{a}_I$ and $\boldsymbol{b}_I$ satisfy the normalization relation

$$\boldsymbol{b}_I^T\boldsymbol{a}_J + \boldsymbol{a}_I^T\boldsymbol{b}_J = \delta_{IJ} \tag{2.29}$$

with δ_{IJ} being the 4 by 4 identity matrix. Remarked that repeated eigenvalues p_I can be avoided by using slightly perturbed material coefficients with negligible errors.

We now consider the integrals of Green's functions over a constant element. Define a generic line segment for any constant element along the interface in the (x,z)-plane, starting from point 1 (x_1, z_1) and ending at point 2 (x_2, z_2). In terms of the parameter t ($0 \le t \le 1$), any constant line element can be expressed as [Pan04b]

$$x = x_1 + (x_2 - x_1)t \tag{2.30a}$$

$$z = z_1 + (z_2 - z_1)t \tag{2.30b}$$

The outward normal components along the line segment are constant, given by

$$n_1 = (z_2 - z_1)/l; \quad n_3 = -(x_2 - x_1)/l \tag{2.31}$$

where $l = \sqrt{(x_2 - x_1)^2 + (z_2 - z_1)^2}$ is the length of the line segment. The variable of integration ds in Eqs. (2.20) and (2.21) is as ds=ldt.

Consider the corresponding integrals $\int_{s_n} U_{IJ} ds$ and $\int_{s_n} T_{IJ} ds$ in Eqs. (2.20) and (2.21). Substitute the Eqs. (2.22) and (2.23) into the above two expressions to get

$$\int_{s_n} U_{IJ} ds = l \int_{s_n} \left(\frac{1}{\pi} \mathrm{Im}\{A_{JR} \ln(z_R - s_R) A_{IR}\}\right) dt \tag{2.32}$$

$$\int_{s_n} T_{IJ} ds = l \int_{s_n} \left(\frac{1}{\pi} \mathrm{Im}\left\{B_{JR} \frac{p_R n_1 - n_3}{z_R - s_R} A_{IR}\right\}\right) dt \tag{2.33}$$

Since p_{R}, A_{JR} and B_{JR} are constant in each segment, Eqs. (2.32) and (2.33) consist of two integrals involving the following integration. For the first integral, we define it, being a function of the source point $\boldsymbol{X}$ =(X, Z), as

$$h_R(X, Z) \equiv \int_0^1 \ln(z_R - s_R) dt \tag{2.34}$$

or,

$$h_R(X,Z)=\int_0^1 \ln\{[(x_2-x_1)+p_R(z_2-z_1)]t+[(x_1+p_Rz_1)-s_R]\}dt \qquad (2.35)$$

Integration of this expression gives

$$h_R(X,Z)=\frac{(x_1+p_Rz_1)-s_R}{(x_2-x_1)+p_R(z_2-z_1)}\ln\left[\frac{x_2+p_Rz_2-s_R}{x_1+p_Rz_1-s_R}\right]+\ln[x_2+p_Rz_2-s_R]-1 \qquad (2.36)$$

Similarly, we define the second integral as

$$g_R(X,Z)\equiv\int_0^1\frac{dt}{z_R-s_R} \qquad (2.37)$$

Integration of this expression gives

$$g_R(X,Z)=\frac{1}{(x_2-x_1)+p_R(z_2-z_1)}\ln\left[\frac{x_2+p_Rz_2-s_R}{x_1+p_Rz_1-s_R}\right] \qquad (2.38)$$

Finally, the integral of the displacement and traction Green's function from the contribution of a constant boundary element can be obtained in the closed form as

$$\int_{s_n} U_{IJ}\,ds=\frac{l}{\pi}\,\mathrm{Im}[A_{JR}h_R(X,Z)A_{IR}] \qquad (2.39)$$

$$\int_{s_n} T_{IJ}\,ds=\frac{l}{\pi}\,\mathrm{Im}[B_{JR}g_R(X,Z)A_{IR}] \qquad (2.40)$$

Therefore, using the constant element discretization the two boundary integral equations (2.18) and (2.19) for the QWR and matrix/substrate can be cast into a system of algebraic equations for the interface points. In matrix form, they can be expressed as

$$\mathbf{U}^w\mathbf{t}^w-(\mathbf{T}^w+b\,\mathrm{I})\mathbf{u}^w=\mathbf{f}^w \qquad (2.41)$$

$$\mathbf{U}^m\mathbf{t}^m-(\mathbf{T}^m+b\,\mathrm{I})\mathbf{u}^m=0 \qquad (2.42)$$

where the coefficient matrices **U** and **T** are the exact integrals of Green's functions on each constant element given in Eqs. (2.39) and (2.40), I is the identity matrix with I(i,j)=δ_{ij}, and *u* and *t* are the general displacement and traction vectors in the center of each constant element. The right-hand side term f^w in Eq. (2.41) is the general equivalent force corresponding to the misfit eigenstrain within the QWR.

We assume that the matrix and QWR are perfectly bonded along the interface *s*, that is, the continuity conditions $u^m = u^w$ and $t^m = -t^w$ hold on the interface. We already know that $b_{IJ}=\frac{1}{2}\delta_{IJ}$ when source point $\boldsymbol{X}$ is on boundary. Then Eqs. (2.20) and (2.21) can be expressed in the matrix form

$$\begin{bmatrix} T^m + \frac{1}{2}\delta_{ij} & U^m \\ T^w + \frac{1}{2}\delta_{ij} & -U^w \end{bmatrix} \begin{bmatrix} u^w \\ t^w \end{bmatrix} = \begin{bmatrix} 0 \\ f^w \end{bmatrix} \tag{2.43}$$

In Eq. (2.43), the number of unknowns is identical to the number of equations so all the nodal (general) displacements and tractions can be determined by Gauss elimination method. Furthermore, making use of the general Somigliana's identity, the general displacement at any location within the QWR can be easily obtained using the solved interface values

$$b_{IJ}u_J = \sum_{n=1}^{N}(\int_{s_n} U_{IJ}^w d\Gamma)t_{Jn}^w + \sum_{n=1}^{N}(\int_{s_n} U_{IJ}^w d\Gamma)\, f_{Jn}^w - \sum_{n=1}^{N}(\int_{s_n} T_{IJ}^w d\Gamma)u_{Jn}^w \tag{2.44}$$

while the displacement at any location within matrix can be obtained as

$$b_{IJ}u_J = \sum_{n=1}^{N}(\int_{s_n} U_{IJ}^m d\Gamma)t_{Jn}^m - \sum_{n=1}^{N}(\int_{s_n} T_{IJ}^m d\Gamma)u_{Jn}^m \tag{2.45}$$

In order to find the strain and electric fields, we need to take the derivation of displacement with respect to the field point $\boldsymbol{x}$ (refer to Eqs. (2.2) and (2.3)). We first write Eqs. (2.22) and (2.23) as

$$U_{IJ}(\boldsymbol{x},\boldsymbol{X}) = \frac{1}{\pi}\mathrm{Im}\left\{A_{JR}d_R(x,X)A_{IR}\right\} \tag{2.46}$$

$$T_{IJ}(\boldsymbol{x},\boldsymbol{X}) = \frac{1}{\pi}\mathrm{Im}\left\{B_{JR}(p_R n_1 - n_3)e_R(x,X)A_{IR}\right\} \tag{2.47}$$

where

$$d_R(x,X) = \ln(z_R - s_R)\,,\ e_R(x,X) = \frac{1}{z_R - s_R} \tag{2.48}$$

The strain field can be obtained by taking the derivative of Eqs. (2.46) and (2.47). Take a point in matrix as an example

$$\gamma_{pq} = \frac{1}{2}\{[\sum_{n=1}^{N}(\int_{s_n} U^m_{pJ,q}d\Gamma)t^m_{Jn} - \sum_{n=1}^{N}(\int_{s_n} T^m_{pJ,q}d\Gamma)u^m_{Jn}] + [\sum_{n=1}^{N}(\int_{s_n} U^m_{qJ,p}d\Gamma)t^m_{Jn} - \sum_{n=1}^{N}(\int_{s_n} T^m_{qJ,p}d\Gamma)u^m_{Jn}]\} \tag{2.49}$$

$$E_p = \sum_{n=1}^{N}(\int_{s_n} U^m_{p4,p}d\Gamma)t^m_{4n} - \sum_{n=1}^{N}(\int_{s_n} T^m_{p4,p}d\Gamma)u^m_{4n} \tag{2.50}$$

where p,q=1 and 3, and

$$U_{IJ,p(q)}(\boldsymbol{x},\boldsymbol{X}) = \frac{1}{\pi}\mathrm{Im}\left\{A_{JR}d_{R,p(q)}(x,X)A_{IR}\right\} \tag{2.51}$$

$$T_{IJ,p(q)}(\boldsymbol{x},\boldsymbol{X}) = \frac{1}{\pi}\mathrm{Im}\left\{B_{JR}(p_R n_1 - n_3)e_{R,p(q)}(x,X)A_{IR}\right\} \tag{2.52}$$

where

$$d_{R,1}(x,X) = \frac{1}{z_R - s_R}\,,\ d_{R,3}(x,X) = \frac{p_R}{z_R - s_R} \tag{2.53}$$

$$e_{R,1}(x,X)=-\frac{1}{(z_R-s_R)^2},\ e_{R,1}(x,X)=-\frac{p_R}{(z_R-s_R)^2} \tag{2.54}$$

Furthermore, utilizing the basic Eq. (2.1), all the internal elastic and electric response in the matrix and QWR can be calculated.

In summary, we have derived the exact boundary integral equations for the QWR and matrix domains by assuming constant elements along their interface. These equations can be used to find the elastic and piezoelectric responses along the interface and at any location within the QWR and its surrounding matrix. Applications of these solutions to QWR systems are discussed in the next section.

2.5 Numerical Examples

Materials used in this numerical section consist of two QWR systems: One is InAs/GaAs with (001)- and (111)-directions, and the other InN/AlN with (1000)- and (0001)-directions. Both the inclusion and inhomogeneity models are studied. For the corresponding inclusion model, the QWR materials will be GaAs, instead of InAs, in the first system, and AlN, instead of InN, in the second system. The material properties and eigenstrains within the QWR in the material coordinates are listed in Tables 1 and 2 [Pan02a, Pan02b].

For InAs (111) and GaAs (111), the coordinate *x*-axis is along [11-2], *y*-axis along [-110], and *z*-axis along [111] directions of the crystalline [Pan02b]. Their material properties can be obtained by simple coordinate rotations. Similarly, for InN (1000) and AlN (1000), the material properties can be obtained by simply exchanging the coordinate directions.

Table 2.1 Material properties & misfit strains in InAs(001)/GaAs (001)

	InAs	GaAs
$C_{11}=C_{22}=C_{33}$ (GPa) $C_{12}=C_{13}=C_{23}$ $C_{44}=C_{55}=C_{66}$	83.29 45.26 39.59	118.8 53.8 59.4
$e_{14}=e_{25}=e_{36}$ (C/m^2)	-0.0456	-0.16
$\varepsilon_{11}=\varepsilon_{22}=\varepsilon_{33}$ ($10^{-9}C^2/Nm^2$)	0.1345808	0.110675
$\gamma_{11}^* = \gamma_{22}^* = \gamma_{33}^*$	0.07	

Table 2.2 Material properties & misfit strains in InN(0001)/AlN (0001)

	InN	AlN
$C_{11}=C_{22}$ (GPa) C_{33} C_{12} $C_{13}=C_{23}$ $C_{44}=C_{55}$ C_{66}	223.0 224.0 115.0 92.0 48.0 54.0	396.0 373.0 137.0 108.0 116.0 129.5
$e_{15}=e_{24}$ (C/m^2) $e_{31}=e_{32}$ e_{33}	-0.22 -0.57 0.97	-0.48 -0.58 1.55
$\varepsilon_{11}=\varepsilon_{22}$ ($10^{-12}C^2/Nm^2$) ε_{33}	132.81 132.81	79.686 97.372
$\gamma_{11}^* = \gamma_{22}^*$ γ_{33}^*	0.1357 0.1267	

2.5.1 Circular and Elliptic QWRs

The first example is for circular and elliptic QWRs in an infinite substrate (Figure 2.3). For this case, exact solutions can be obtained for both the inclusion and inhomogeneity models.

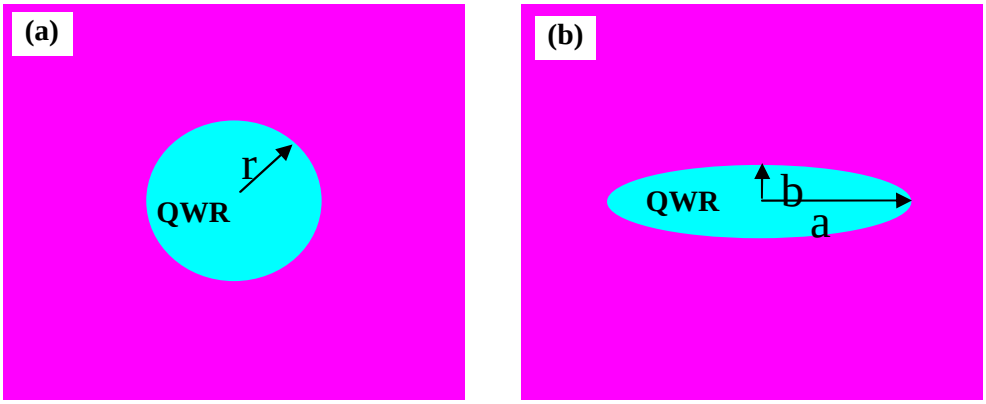

Figure 2.3 A circle QWR of radius r=10nm in an infinite substrate (a), and an ellipse QWR with length of the semi-major axis a=20nm in horizontal x-direction and the semi-minor axis b=5nm in vertical z-direction in an infinite substrate in (b).

Tables 2.3-2.6 compare the strain and electric fields inside both the circular and elliptic inclusion and inhomogeneity (Figure 2.3), using the material properties and eigenstrain listed in Tables 2.1 and 2.2. We point out that for these QWR shapes, the induced fields inside the QWR are uniform for both inclusion and inhomogeneity models. These results can be obtained using the analytical solution for the QWR inclusion problem [Pan04a], combined with the Eshelby inhomogeneity method [Esh57, Esh61, Mur87]. Furthermore, we have also used our BEM formulation presented above for these models. In doing so, we have mutually checked our analytical and numerical solutions.

It is observed from Tables 2.3-2.6 that the relative error, defined as (inclusion solution – inhomogeneity solution)/ (inhomogeneity solution), for the strain and electric field (10^7V/m) between the inclusion and inhomogeneity models is generally around 10%, which is consistent with the recent prediction for the purely elastic QWR semiconductor [Yan02, Pan05]. We also note that for the elliptical QWR case, the horizontal strain γ_{xx} based on the inhomogeneity model can be much different than those based on the inclusion model. Perhaps the most important feature is on the difference of the electric

fields in the InAs/GaAs (111) system. It is observed that the electric field difference based on the inclusion and inhomogeneity models can be more than one order of the magnitude (Table 2.4). This special feature has not been reported in any previous investigation and will be discussed again in the following two examples.

Table 2.3 Strains in inclusion GaAs (001) and inhomogeneity InAs(001)/GaAs (001)

		Inclusion	Inhomogeneity	Relative Error (%)
Circle	$\gamma_{xx}=\gamma_{zz}$	0.0612	0.0566	9
Ellipse	γ_{xx}	0.0208	0.0134	55
	γ_{zz}	0.1058	0.1133	7

Table 2.4 Strains in inclusion GaAs (111) and inhomogeneity InAs(111)/GaAs (111)

		Inclusion	Inhomogeneity	Relative Error (%)
Circle	γ_{xx}	0.0596	0.0551	8
	γ_{zz}	0.0543	0.0500	9
	$2\gamma_{xz}$	-0.0149	-0.0145	2
	E_x ($\times 10^7$V/m)	4.020	0.2738	1368
	E_z ($\times 10^7$V/m)	-2.843	-0.1936	1368
Ellipse	γ_{xx}	0.0260	0.0196	33
	γ_{zz}	0.0829	0.0861	4
	$2\gamma_{xz}$	-0.0081	-0.0075	9
	E_x ($\times 10^7$V/m)	1.235	0.4773	176
	E_z ($\times 10^7$V/m)	-9.770	2.074	571

Table 2.5 Strain in inclusion AlN(0001) and inhomogeneity InN(0001)/AlN(0001)

		Inclusion	Inhomogeneity	Relative Error (%)
Circle	γ_{xx}	0.1184	0.1063	11
	γ_{zz}	0.0984	0.0876	12
	E_z ($\times 10^7$V/m)	-47.05	-42.65	10
Ellipse	γ_{xx}	0.0515	0.0310	66
	γ_{zz}	0.1555	0.1746	11
	E_z	-159.0	-130.1	22

Table 2.6 Strain in inclusion AlN(1000) and inhomogeneity InN(1000)/AlN(1000)

		Inclusion	Inhomogeneity	Relative Error (%)
Circle	γ_{xx}	0.0984	0.0876	12
	γ_{zz}	0.1184	0.1063	11
	E_x ($\times 10^7$V/m)	-47.05	-42.65	10
Ellipse	γ_{xx}	0.0403	0.0223	81
	γ_{zz}	0.1797	0.2008	11
	E_x ($\times 10^7$V/m)	2.435	2.780	12

2.5.2 Square QWR in GaAs and hexagon QWR in AlN

The second example is for a square QWR in GaAs and a hexagon QWR in AlN (Figure 2.4) where the induced strain and electric fields are presented along the horizontal and diagonal (inclined in hexagon) lines (dashed lines in Figure 2.4).

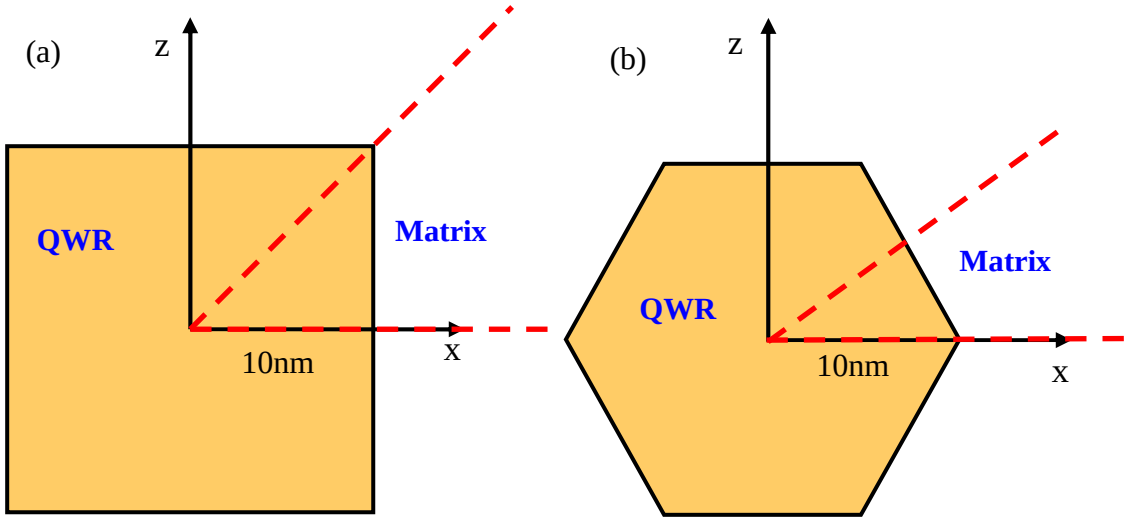

Figure 2.4 A square QWR in GaAs (a) and a hexagon QWR in AlN (b).

We first test the convergence of our program. Take the square InAs/GaAs (111) as an example. The interface of the square is discretized to 100 or 120 segments. The strain (Table 2.7) and electric field (Table 2.8) at some locations along horizontal line in Fig.

2.4(a) are listed. The results show that the errors are negligible when using different mesh sizes and our program has good convergence when the mesh size reaches 100.

Table 2.7 Strain γ_{xx} in inhomogeneity InAs/GaAs(111) for different mesh sizes

Mesh size / x (nm)	100	120	Relative Error (%)
0	0.0572	0.0572	0
1	0.0574	0.0573	0.17452
9	0.0714	0.0715	0.13986
11	-0.0318	-0.0317	0.315457
20	-0.0162	-0.0162	0

Table 2.8 Electric field $E_x(\times 10^7 \text{V/m})$ in inhomogeneity InAs/GaAs(111) for different mesh sizes

Mesh size / x (nm)	100	120	Relative Error (%)
0	0.513	0.515	0.38835
1	0.506	0.508	0.3937
9	0.110	0.111	0.9009
11	0.278	0.281	1.06762
20	-0.171	-0.171	0

Shown in Figures 2.5 and 2.6 are the hydrostatic strain ($\gamma_{xx} + \gamma_{zz}$) along both horizontal and diagonal lines in both InAs/GaAs (001) and InAs/GaAs (111). These results are similar to those for the InAs/GaAs QWR with trapezoidal shape [Pan05]. In general, the elastic strain fields inside the QWR are much larger than those in the substrate and the difference in the strain fields based on the inhomogeneity and inclusion models is apparent, particularly within the QWR.

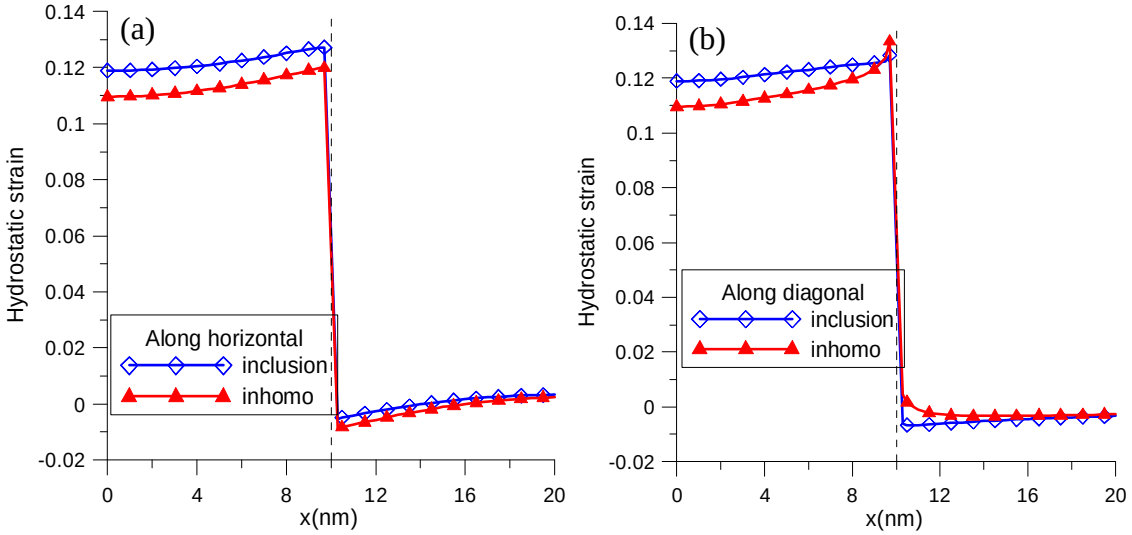

Figure 2.5 Hydrostatic strains ($\gamma_{xx} + \gamma_{zz}$) in a square QWR InAs/GaAs (001) along the horizontal (a) and diagonal (b) lines.

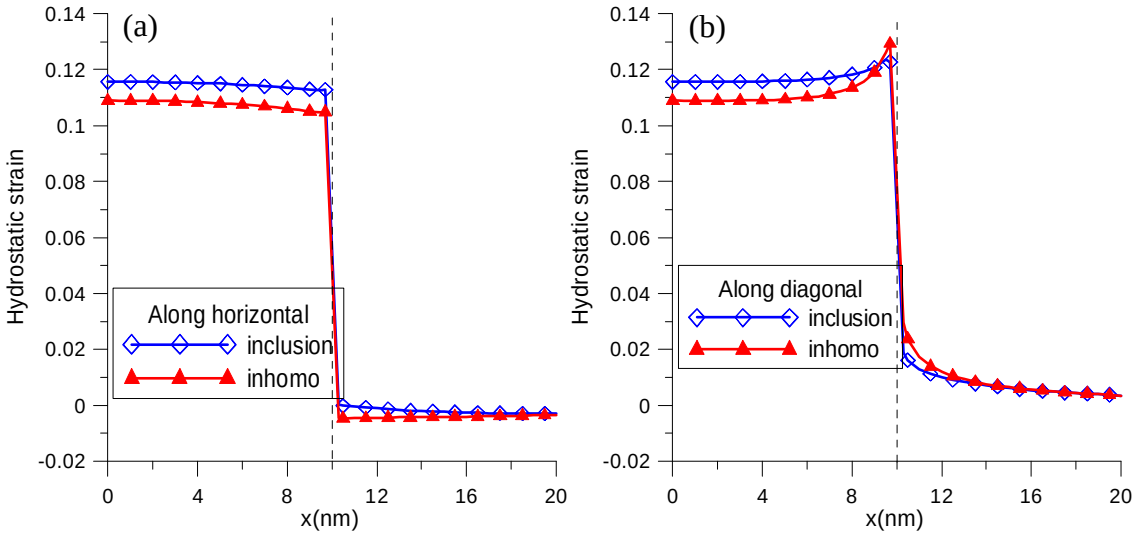

Figure 2.6 Hydrostatic strains ($\gamma_{xx} + \gamma_{zz}$) in a square QWR InAs/GaAs (111) along the horizontal (a) and diagonal (b) lines.

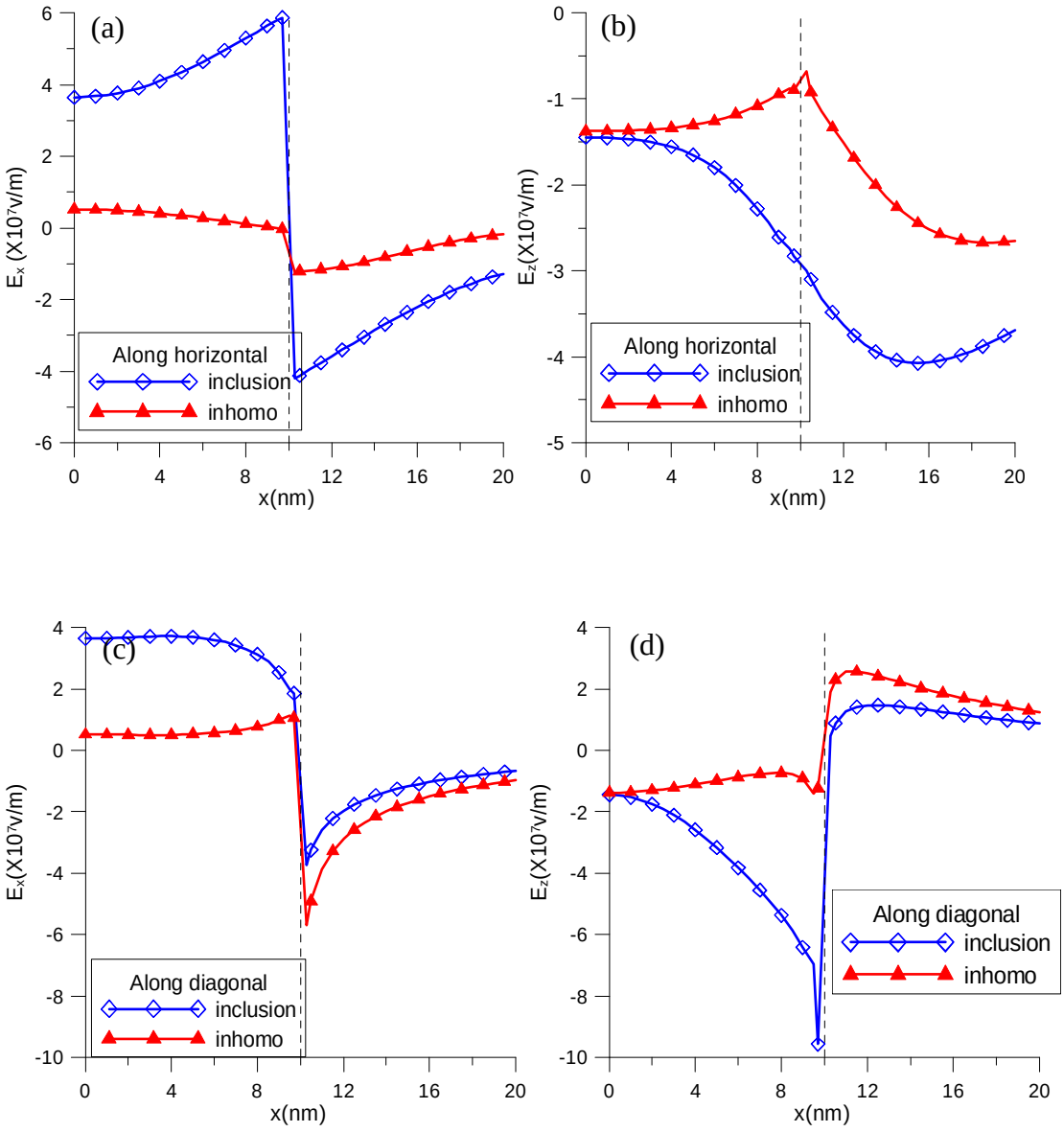

Figure 2.7 E_x (a) and E_z (b) along the horizontal line, and E_x (c) and E_z (d) along the diagonal line, in square QWR InAs/GaAs (111).

It has been well-known that while there is no induced electric field in the InAs/GaAs (001) system, large electric fields can be observed in QWs, QWRs, and QDs (111) systems [Pan02b,Smi86]. Here in Figure 2.7 we show for the first time that the induced electric fields along the horizontal and diagonal lines in InAs/GaAs (111) of a square

QWR can be large and that the difference of the electric fields based on the inclusion and inhomogeneity models can be significant, especially within the QWR. In other words, electric fields in the InAs/GaAs (111) orientation should not be neglected, and it should be considered using the correct inhomogeneity model as the simple inclusion model could be completely wrong. Furthermore, for the induced electric field, its magnitudes both inside and outside the QWR are comparable, in contrast to the corresponding strain field featured in Figures 2.5 and 2.6.

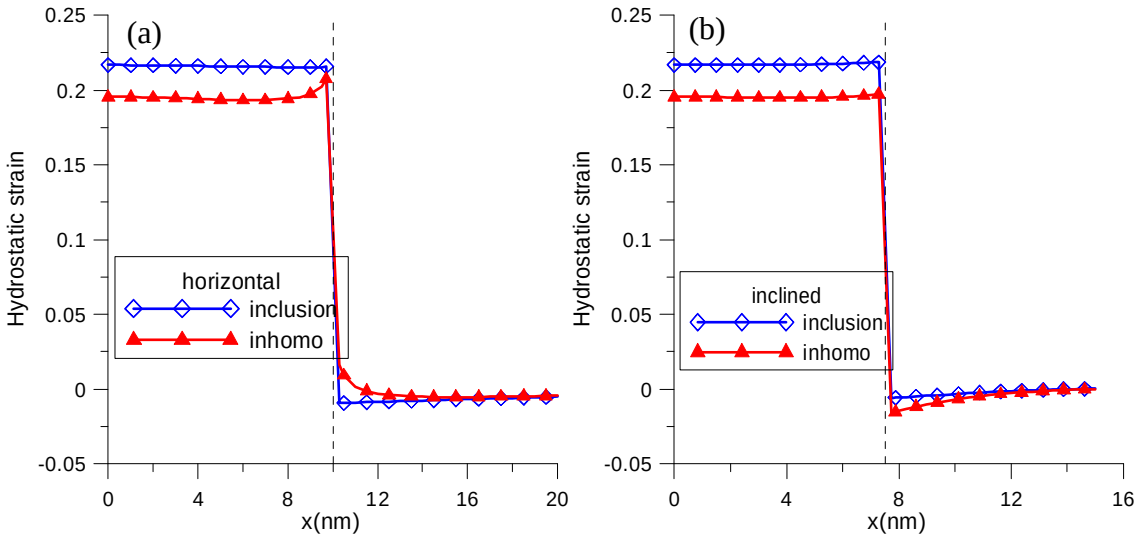

Figure 2.8 Hydrostatic strains (γ_{xx} +γ_{zz}) in hexagon QWR InN/AlN (0001) along horizontal (a) and inclined (b) lines.

Figure 2.8 shows the hydrostatic strain in InN/AlN(0001) along the horizontal and inclined lines. Similar to the hydrostatic strain in the InAs/GaAs system, we observed that, outside the QWR, both the inclusion and inhomogeneity models predict agreeable results, with their magnitudes outside being also much smaller than those inside the QWRs. However, near the interface between the QWR and substrate, apparent difference

can be observed. Furthermore, for the hydrostatic strain inside the QWR, the inclusion model predicts a high value than the inhomogeneity one (about 11%). For the InN/AlN (1000), the hydrostatic strain distribution is similar.

Figure 2.9 shows the electric field distribution along the horizontal line for both InN/AlN (0001) and (1000). For orientation (0001), the only non-zero E-field is E_x whilst for (1000), we have only E_z. It is observed from Fig. 2.9 that the inclusion model predicts very close results as compared to those based on the inhomogeneity one, except for the points close to the interface where the E-field experiences a shape change, resulting in different values based on different models.

Shown in Figures 2.10 and 2.11 are the E-fields E_x and E_z along the inclined line in both InN/AlN (0001) and (1000). It is noted that along the inclined line, both E_x and E_z are different from zero, as compared to Figure 2.9 where one of the electric components is zero. Similar to Figure 2.9, the results predicted by the simple inclusion model are mostly reliable as compared to those based on the inhomogeneity model; however, inside the QWR or close to the interface between the QWR and substrate, the inhomogeneity should be employed.

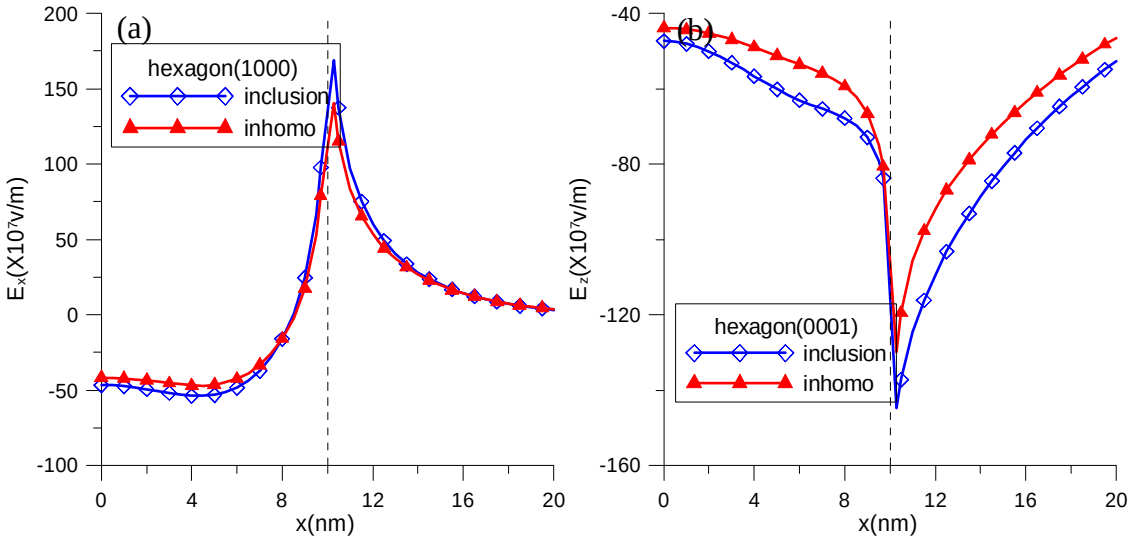

Figure 2.9 E_x in InN/AlN(1000) (a) and E_z in InN/AlN(0001) (b) along the horizontal line.

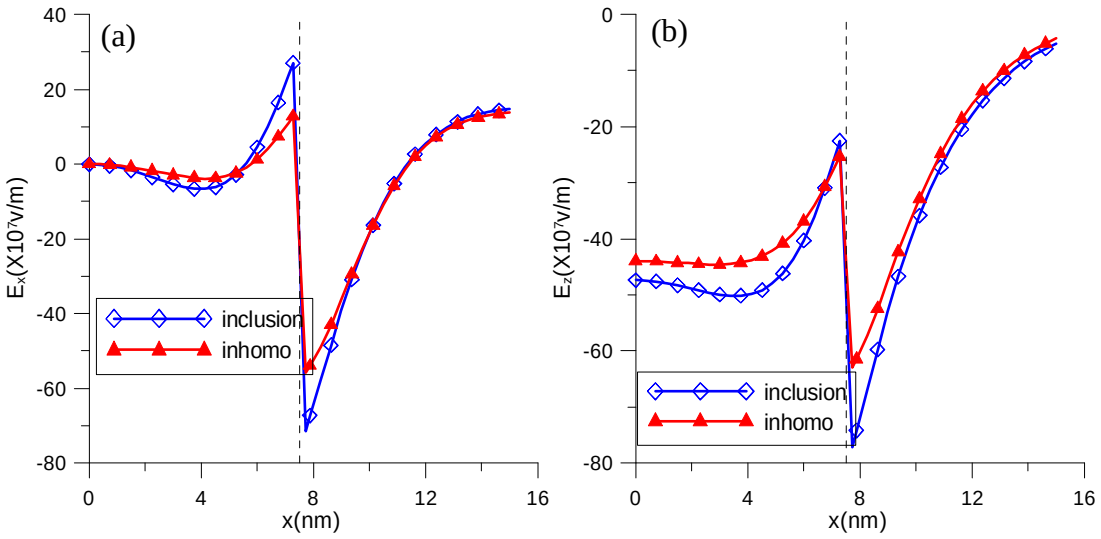

Figure 2.10 E_x (a) and E_z (b) in InN/AlN (0001) along the inclined line.

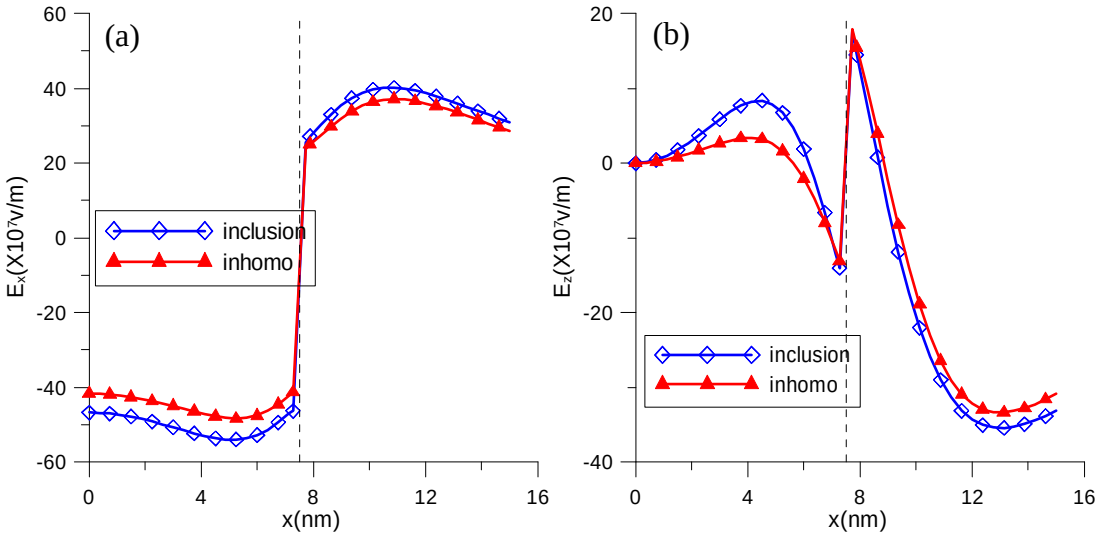

Figure 2.11 E_x (a) and E_z (b) in InN/AlN(1000) along the inclined line.

2.5.3 QWRs of Different Polygonal Shapes

In this example, we study the induced E-fields inside and outside a polygonal QWR with different sides (n=3,4,5,6,10, and infinity), a model used before for the corresponding corner singularity study [Pan06]. The model is shown in Figure 2.12 with the E-fields being calculated along the horizontal x-axis. Only the results from the inhomogeneity models InAs (111)/GaAs (111), InN (0001)/AlN (0001), and InN (0001)/AlN (0001) are presented.

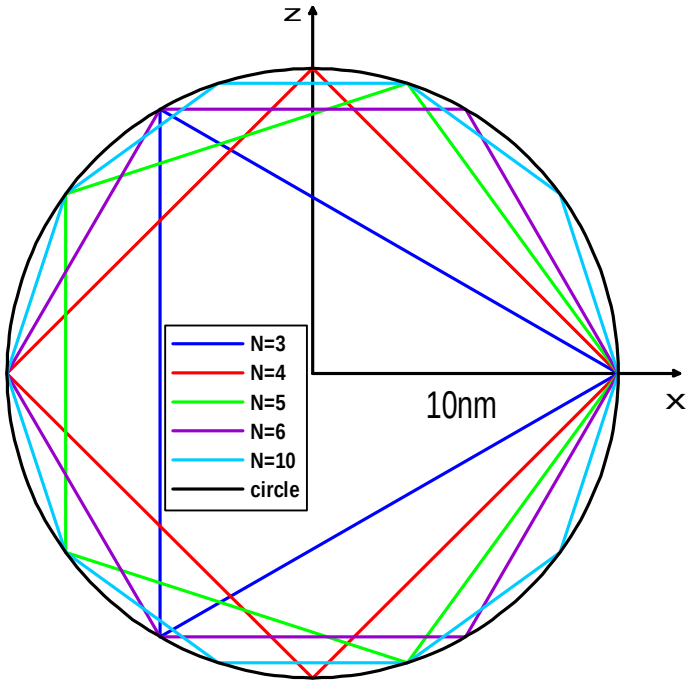

Figure 2.12 The polygons with sides n=3,4,5,6,10 and infinity (circle).

Figure 2.13 shows that inside and outside the QWR, both E-field components are nonzero along the horizontal x-axis and that just as for the second example, the magnitudes of the E-fields are comparable both inside and outside the QWR. We also observe that the results from the regular triangle and square QWRs are completely different from the other polygonal QWRs. This can be seen more clearly from Table 2.9 where the E-fields at the center of the polygons are listed. It is obvious that the signs of E_x and E_z, are respectively the same for both triangle and square QWRs, which have opposite signs as compared to those in other polygons. Furthermore, while the central values of the E-fields are very small for the triangle QWR, the E_z component in square QWR are much larger than those in other polygon (50-100% large).

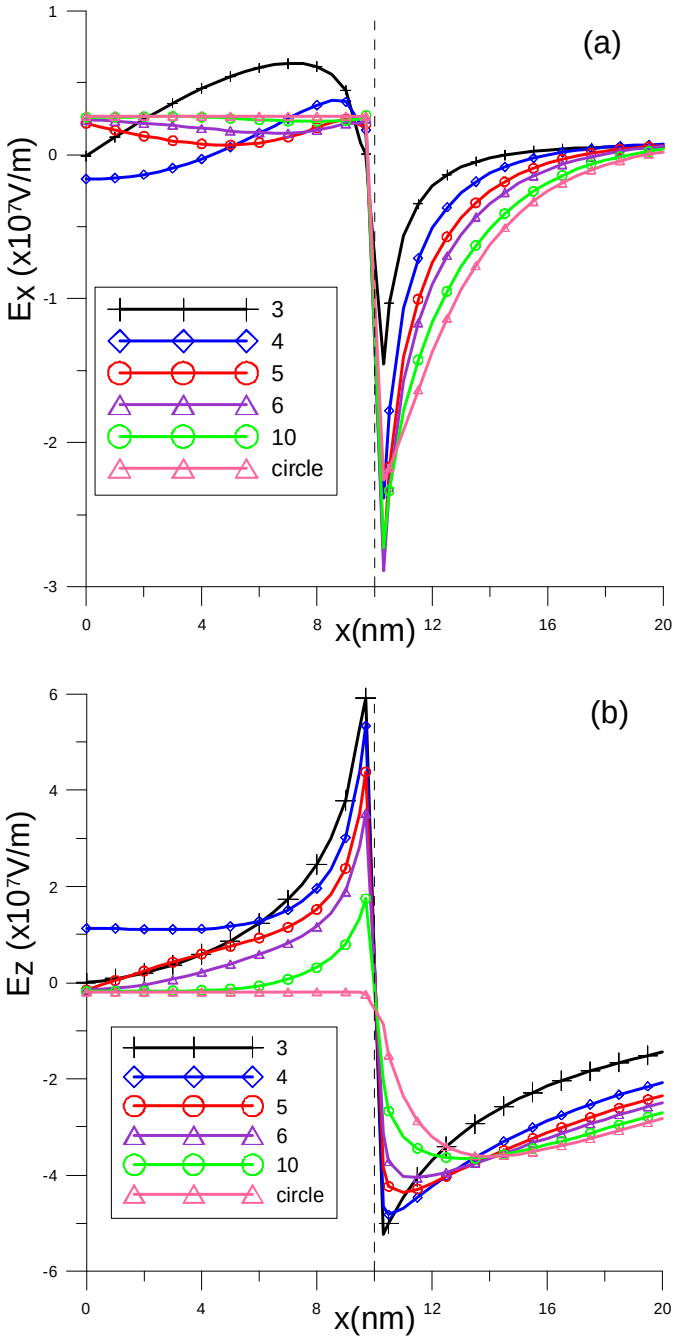

Figure 2.13 E_x (a) and E_z (b) in InAs/GaAs (111) along the horizontal line for n=3,4,5,6,10, and infinity (circle).

Figure 2.14 show the E-field along the horizontal axis in InN/AlN (1000) and (0001). Due to the symmetric property of the problem the only nonzero component is E_x in (1000) orientation and E_z in (0001) orientation. It is noted that:

(1). There is a sharp change in the E-field at the geometric corner point (x=10nm);

(2). The trend of the field variation in triangle QWR is completely different to those in other polygons;

(3). At the center of the polygons, the E-field of the square is much larger than those in other polygons where the results are very close to each other (Table 2.10) except for the square QWR. The difference of the E-field magnitude at the center between square and other polygons is about 25%.

Table 2.9 Electric fields at the center of the polygonal QWRs of InAs/GaAs (111)

Polygon sides/Fields	E_x (MV/m)	E_z (MV/m)
3	-0.0071	0.0012
4	-0.1701	1.1285
5	0.2182	-0.1546
6	0.2396	-0.1430
10	0.2613	-0.1851
Circle	0.2689	-0.1902

Table 2.10 Electric fields ($\times 10^7$V/m) at the center of the polygonal QWRs of InN/AlN

Polygon sides/Fields	E_x in (1000)	E_z in (0001)
3	-42.33	-45.74
4	-56.89	-56.89
5	-42.86	-43.00
6	-41.73	-43.96
10	-42.63	-42.76
Circle	-42.66	-42.66

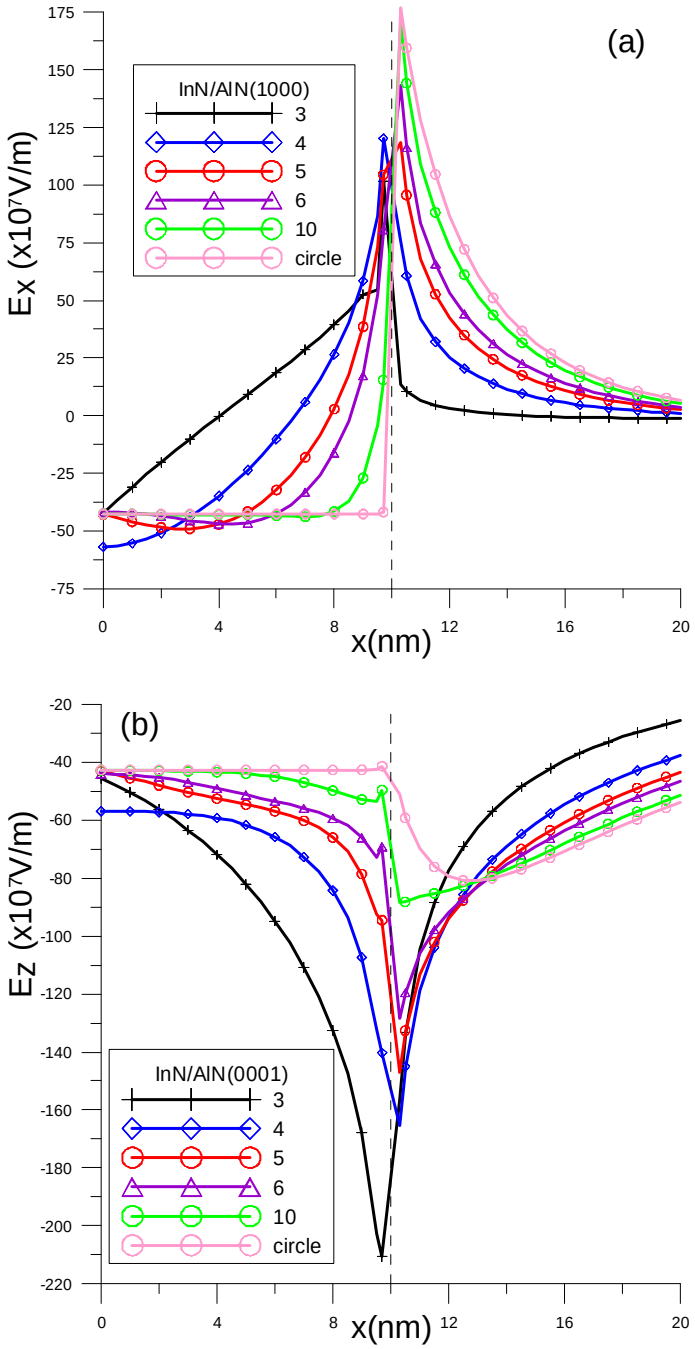

Figure 2.14 E_x (a) in InN/AlN (1000) and E_z (b) in InN/AlN (0001) along the horizontal line for n=3,4,5,6,10, and infinity (circle).

2.6 Conclusions

In this chapter, an accurate BEM modeling is proposed for the strain and electric fields analysis in QWR structures. Constant elements are employed to discretize the interface between the QWR and substrate with the integrand being analytically carried out utilizing the exact close-form Green's functions for anisotropic piezoelectric solids. The material models are both group III-V and nitride III group, and both the well-accepted inclusion and inhomogeneity models are discussed. The elastic and piezoelectric response at any location can be predicted based on the inclusion and inhomogeneity models. From our study, some important features are observed, with those for the strain field being consistent to recent published results: 1). In the substrate and far away from the QWR, both the inclusion and inhomogeneity models predict very close strain field. In other words, the simplified homogeneous inclusion model can be safely applied if one could like to have a quick estimation of the strain field. 2). For points inside or close to the QWR, the strain difference between the two models can be as high as 10% for the test structures, which can result in strong variations of the confined electronic states. 3). While the magnitude of strain inside the QWR is much larger than that outside, the electric fields have the same magnitudes both inside and outside the QWR. 4). While the difference in the electric fields based on both inclusion and inhomogeneity models is small in the InN/AlN system, that in the InAs/GaAs (111) can be large. In other words, the inhomogeneity model should be employed if possible. 5). It is also observed that the electric fields in the QWR depend strongly on the QWR geometry shape; The electric field in triangle and square QWRs is different from those in the polygons made of more than 4 sides.

CHAPTER III

ELASTIC AND ELECTRIC FIELDS INDUCED BY QWR IN BIMATERIAL PLANE

3.1 Summary

Two-dimensional BEM is very convenient in analyzing stress and fracture problems in bimaterial solids. The bimaterial Green's functions in transversely isotropic piezoelectric solids [Din04], anisotropic elastic [Pan99a] and piezoelectric bodies [Pan99b, Gar05, Gro05], and in magnetoelectroelastic solids [Qin05] were studied and applied to different mechanical and piezoelectric problems. We remark that these Green's functions were presented in the Lekhnitskii formalism [Pan99a]. Applications of the 2D BEM also include the determination of stress intensity factors for interfacial rigid line inclusion [Lee02], symmetric BEM formulation for cohesive interface problem [Sal03], and analysis of collinear interfacial cracks interaction [Sun06]. Other extended studies include thermomechanical closure of interfacial cracks [Gia07], fracture problems in magnetoelectroelastic composites [Gar07], and dynamic fracture problems involving bimaterial solids [Lei03, Lei04, Lei07].

In this chapter, we develop the anisotropic bimaterial Green's functions in terms of the efficient and powerful Stroh formalism [Tin96] and the corresponding BEM program for the analysis of the strain energy density and the relative strain energy for a QWR free-standing on or embedded in an anisotropic substrate. The boundary of QWR was

discretized with constant elements so that the involved kernel integration can be carried out in an exact closed form, which is solved for the boundary (interface) values. The induced elastic field inside and outside the QWR can be obtained using the solved interface values. We remark that in order to apply our bimaterial program to the free-standing QWR case, we only need to assume that the material stiffness in the upper half-plane is much smaller than that in the lower half-plane substrate.

Our bimaterial BEM program is first tested against various existing results. It is then applied to calculate the strain energy density and the relative strain energy in the InAs (111) QWR which is free-standing on or embedded in the GaAs substrate.

This chapter is organized as follows: In Section 3.2, the basic problem is presented. In Section 3.3, the boundary integral equation and the required four sets of Green's functions for the bimaterial matrix are presented. In Section 3.4 and 3.5, the integration and derivatives of bimaterial Green's function are obtained. In Section 3.6, the formulation of elastic strain energy density and the relative strain energy are presented. Numerical examples are presented in Section 3.7, and conclusions are drawn in Section 3.8.

3.2 Problem Description for QWR in Bimaterial Substrate

We assume that there is a QWR of arbitrary shape within a bimaterial substrate. A uniform eigenstrain γ_{ij}^{*} field is applied inside the QWR as shown in Figure 3.1. The elastic moduli in the QWR, material 1 and material 2 are denoted, respectively, as c_{ijkl}^{w}, c_{ijkl}^{1} and c_{ijkl}^{2}. In each domain, the basic equations remain the same as in section 2.2.

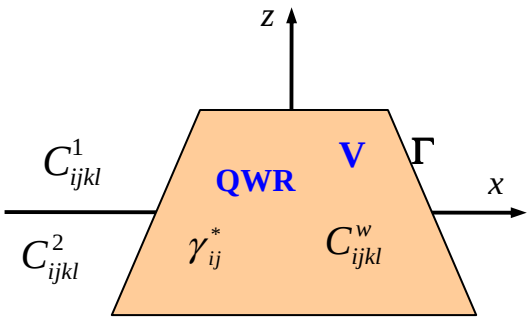

Figure 3.1 A general QWR within a bimaterial substrate: An eigenstrain γ^*_{ij} is applied to the QWR which is an arbitrarily shaped polygon.

3.3 Bimaterial Green's Function

The boundary of QWR is discretized into constant elements. The discretized integral equations remain same as Eqs. (2.20) and (2.21). It is noted that in order to solve the discretized boundary integral equations, the involved Green's functions U_{ij} and T_{ij} and their integrations on each element are required. For the QWR domain, only the full-plane Green's functions are required, which can be expressed as (2.22) and (2.23).

For the matrix domain (i.e., the bimaterial substrate), due to the relative locations of the source and field points, there are four sets of Green's functions. Again, these Green's functions were derived in terms of the Lekhnitskii formalism [Pan99a]. However, the Stroh formulism is more convenient and efficient [Tin96] because the it possesses the eigenrelation that relates the eigenmodes of stress functions and displacement to the material properties. Therefore, we first present these bimaterial Green's functions in the Stroh formulism. We refer to Figure 3.1 where materials 1 and 2 occupy the half-plane z>0 and z<0, respectively.

First, let the source point $\boldsymbol{X}$ =(X, Z) be in material 1 (z>0). Then, if the field point $\boldsymbol{x}$=(x, z) is in the z>0 half-plane, the displacement and traction Green's functions can be expressed as

$$U_{kj}^{1}=\frac{1}{\pi}\mathrm{Im}\{A_{jr}^{1}\ln(z_r-s_r)A_{kr}^{1}+\sum_{v=1}^{4}[A_{jr}^{1}\ln(z_r-\bar{s}_v)Q_{rk}^{11,v}]\} \tag{3.1}$$

$$T_{kj}^{1}=-\frac{1}{\pi}\mathrm{Im}\{B_{jr}^{1}\frac{p_r^1n_1-n_3}{z_r-s_r}A_{kr}^{1}+\sum_{v=1}^{4}[B_{jr}^{1}\frac{p_r^1n_1-n_3}{z_r-\bar{s}_v}Q_{rk}^{11,v}]\} \tag{3.2}$$

On the other hand, if the field point is in the z<0 half-plane, then

$$U_{kj}^{2}=\frac{1}{\pi}\mathrm{Im}\sum_{v=1}^{4}[A_{jr}^{2}\ln(z_r-s_v)Q_{rk}^{12,v}] \tag{3.3}$$

$$T_{kj}^{2}=-\frac{1}{\pi}\mathrm{Im}\sum_{v=1}^{4}[B_{jr}^{2}\frac{p_r^2n_1-n_3}{z_r-s_v}Q_{rk}^{12,v}] \tag{3.4}$$

Now, let the source point (X, Z) be in material 2 (z<0). Then, if the field point (x, z) is in the z>0 half-plane, we have

$$U_{kj}^{1}=\frac{1}{\pi}\mathrm{Im}\sum_{v=1}^{4}[A_{jr}^{1}\ln(z_r-s_v)Q_{rk}^{21,v}] \tag{3.5}$$

$$T_{kj}^{1}=-\frac{1}{\pi}\mathrm{Im}\sum_{v=1}^{4}[B_{jr}^{1}\frac{p_r^1n_1-n_3}{z_r-s_v}Q_{rk}^{21,v}] \tag{3.6}$$

On the other hand, if the field point is in the z<0 half-plane,

$$U_{kj}^{2}=\frac{1}{\pi}\mathrm{Im}\{A_{jr}^{2}\ln(z_r-s_r)A_{kr}^{2}+\sum_{v=1}^{4}[A_{jr}^{2}\ln(z_r-\bar{s}_v)Q_{rk}^{22,v}]\} \tag{3.7}$$

$$T_{kj}^{2}=-\frac{1}{\pi}\mathrm{Im}\{B_{jr}^{2}\frac{p_r^2n_1-n_3}{z_r-s_r}A_{kr}^{2}+\sum_{v=1}^{4}[B_{jr}^{2}\frac{p_r^2n_1-n_3}{z_r-\bar{s}_v}Q_{rk}^{22,v}]\} \tag{3.8}$$

In Eqs. (3.1)-(3.8), the superscript 1 or 2 to p, $\boldsymbol{A}$, and $\boldsymbol{B}$, denotes that these eigenvalues and the corresponding eigenmatrices belong to material 1 or 2. The matrix $\boldsymbol{Q}$ depends on

the relative locations of the source and field points. Assuming that the source point is in the half-plane of material λ (λ=1 or 2). Then $\boldsymbol{Q}$ can be expressed as

$$Q_{rk}^{\lambda\lambda,v} = K_{rj}^{\lambda\lambda}(I_v)_j \overline{A}_{kj}^{\lambda} \tag{3.9}$$

if the field point is in the half-plane of material λ, and

$$Q_{rk}^{\lambda\mu,v} = K_{rj}^{\lambda\mu}(I_v)_j A_{kj}^{\lambda} \tag{3.10}$$

if the field point is in the other half-plane of material μ ($\mu \neq \lambda$). In Eqs. (3.9) and (3.10), the matrix $\boldsymbol{K}$ is given by

$$\boldsymbol{K}^{\lambda\lambda} = (\boldsymbol{A}^{\lambda})^{-1}(\boldsymbol{M}^{\lambda} + \bar{\boldsymbol{M}}^{\mu})^{-1}(\boldsymbol{M}^{\mu} - \bar{\boldsymbol{M}}^{\lambda})\bar{\boldsymbol{A}}^{\lambda} \tag{3.11}$$

$$\boldsymbol{K}^{\lambda\mu} = (\boldsymbol{A}^{\mu})^{-1}(\boldsymbol{M}^{\mu} + \bar{\boldsymbol{M}}^{\lambda})^{-1}(\boldsymbol{M}^{\lambda} + \bar{\boldsymbol{M}}^{\lambda})\boldsymbol{A}^{\lambda} \tag{3.12}$$

with $\boldsymbol{M}^{\lambda} = -i\boldsymbol{B}^{\lambda}(\boldsymbol{A}^{\lambda})^{-1}$ (λ=1 or 2) and the diagonal matrix I_v has the following expression for different indexes v,

$$I_1=\text{diag}[1,0,0];\ I_2=\text{diag}[0,1,0];\ I_3==\text{diag}[0,0,1] \tag{3.13}$$

3.4 Integration of Bimaterial Green's Function

In order to carry out the line integral of the involved Green's functions over each constant element (e.g., along the n-th element Γn), we let the generic element start from point 1 (x_1, z_1) and end at point 2 (x_2, z_2), with length $l = \sqrt{(x_2 - x_1)^2 + (z_2 - z_1)^2}$. Then, the integration of the involved Green's displacements and tractions (only the integral variable-dependent function) for the QWR (which requires only the infinite-plane Green's functions) can be carried out, which has been expressed in section 2.4.

We point out that similar expressions can be found for the integration of the bimaterial Green's functions in the substrate. Let the source point $\boldsymbol{X}$ be in material 1, if the field point $\boldsymbol{x}$ is in material 1, the corresponding integrals are

$$\begin{aligned} h_r^1(x,z) &= \int_{\Gamma_n} \ln(z_r^1 - s_r^1) d\Gamma_n \\ &= l[\frac{(x_1 + p_r^1 z_1) - s_r^1}{(x_2 - x_1) + p_r^1 (z_2 - z_1)} \ln[\frac{(x_2 + p_r^1 z_2) - s_r^1}{(x_1 + p_r^1 z_1) - s_r^1}] + \ln(x_2 + p_r^1 z_2 - s_r^1) - 1] \end{aligned} \tag{3.14}$$

$$\begin{aligned} w_{rv}^1(x,z) &= \int_{\Gamma_n} \ln(z_r^1 - \bar{s}_v^1) d\Gamma_n \\ &= l[\frac{(x_1 + p_r^1 z_1) - \bar{s}_v^1}{(x_2 - x_1) + p_r^1 (z_2 - z_1)} \ln[\frac{(x_2 + p_r^1 z_2) - \bar{s}_v^1}{(x_1 + p_r^1 z_1) - \bar{s}_v^1}] + \ln(x_2 + p_r^1 z_2 - \bar{s}_v^1) - 1] \end{aligned} \tag{3.15}$$

and

$$g_r^1(x,z) = \int_{\Gamma_n} \frac{1}{z_r^1 - s_r^1} d\Gamma_n = l[\frac{1}{(x_2 - x_1) + p_r^1 (z_2 - z_1)} \ln(\frac{x_2 + p_r^1 z_2 - s_r^1}{x_1 + p_r^1 z_1 - s_r^1})] \tag{3.16}$$

$$d_{rv}^1(x,z) = \int_{\Gamma_n} \frac{1}{z_r^1 - \bar{s}_v^1} d\Gamma_n = l[\frac{1}{(x_2 - x_1) + p_r^1 (z_2 - z_1)} \ln(\frac{x_2 + p_r^1 z_2 - \bar{s}_v^1}{x_1 + p_r^1 z_1 - \bar{s}_v^1})] \tag{3.17}$$

When source point $\boldsymbol{X}$ is in material 1, and the field point $\boldsymbol{x}$ is in material 2, the corresponding integrals are

$$\begin{aligned} h_{rv}^{21}(x,z) &= \int_{\Gamma_n} \ln(z_r^2 - s_v^1) d\Gamma_n \\ &= l[\frac{(x_1 + p_r^2 z_1) - s_v^1}{(x_2 - x_1) + p_r^2 (z_2 - z_1)} \ln[\frac{(x_2 + p_r^2 z_2) - s_v^1}{(x_1 + p_r^2 z_1) - s_v^1}] + \ln(x_2 + p_r^2 z_2 - s_v^1) - 1] \end{aligned} \tag{3.18}$$

and

$$g_{rv}^{21}(x,z) = \int_{\Gamma_n} \frac{1}{z_r^2 - s_v^1} d\Gamma_n = l[\frac{1}{(x_2 - x_1) + p_r^2 (z_2 - z_1)} \ln(\frac{x_2 + p_r^2 z_2 - s_v^1}{x_1 + p_r^2 z_1 - s_v^1})] \tag{3.19}$$

When source point $\boldsymbol{X}$ is in material 2, and the field point $\boldsymbol{x}$ is in material 1, the corresponding integrals are

$$h_{rv}^{12}(x,z)=\int_{\Gamma_n}\ln(z_r^1-s_v^2)d\Gamma_n$$
$$=l[\frac{(x_1+p_r^1z_1)-s_v^2}{(x_2-x_1)+p_r^1(z_2-z_1)}\ln[\frac{(x_2+p_r^1z_2)-s_v^2}{(x_1+p_r^1z_1)-s_v^2}]+\ln(x_2+p_r^1z_2-s_v^2)-1] \quad (3.20)$$

and

$$g_{rv}^{12}(x,z)=\int_{\Gamma_n}\frac{1}{z_r^1-s_v^2}d\Gamma_n=l[\frac{1}{(x_2-x_1)+p_r^1(z_2-z_1)}\ln(\frac{x_2+p_r^1z_2-s_v^2}{x_1+p_r^1z_1-s_v^2})] \quad (3.21)$$

When source point $\boldsymbol{X}$ is in material 2, and the field point $\boldsymbol{x}$ is in material 2, the corresponding integrals are

$$h_r^2(x,z)=\int_{\Gamma_n}\ln(z_r^2-s_r^2)d\Gamma_n$$
$$=l[\frac{(x_1+p_r^2z_1)-s_r^2}{(x_2-x_1)+p_r^2(z_2-z_1)}\ln[\frac{(x_2+p_r^2z_2)-s_r^2}{(x_1+p_r^2z_1)-s_r^2}]+\ln(x_2+p_r^2z_2-s_r^2)-1] \quad (3.22)$$

$$w_{rv}^2(x,z)=\int_{\Gamma_n}\ln(z_r^2-\bar{s}_v^2)d\Gamma_n$$
$$=l[\frac{(x_1+p_r^2z_1)-\bar{s}_v^2}{(x_2-x_1)+p_r^2(z_2-z_1)}\ln[\frac{(x_2+p_r^2z_2)-\bar{s}_v^2}{(x_1+p_r^2z_1)-\bar{s}_v^2}]+\ln(x_2+p_r^2z_2-\bar{s}_v^2)-1] \quad (3.23)$$

and

$$g_r^2(x,z)=\int_{\Gamma_n}\frac{1}{z_r^2-s_r^2}d\Gamma_n=l[\frac{1}{(x_2-x_1)+p_r^2(z_2-z_1)}\ln(\frac{x_2+p_r^2z_2-s_r^2}{x_1+p_r^2z_1-s_r^2})] \quad (3.24)$$

$$d_{rv}^2(x,z)=\int_{\Gamma_n}\frac{1}{z_r^2-\bar{s}_v^2}d\Gamma_n=l[\frac{1}{(x_2-x_1)+p_r^2(z_2-z_1)}\ln(\frac{x_2+p_r^2z_2-\bar{s}_v^2}{x_1+p_r^2z_1-\bar{s}_v^2})] \quad (3.25)$$

3.5 Derivatives of Bimaterial Green's Function

In order to obtain the strain and stress fields, we also need to take the derivative of the Green's displacement and traction with respect to the source point, and then find the corresponding integration. The integration of the involved Green's function derivatives for the QWR domain can be written as

$$h_{r,x} = \int_{\Gamma_n} \frac{\partial \ln(z_r - s_r)}{\partial x} d\Gamma_n = -\frac{l}{(x_2 - x_1) + p_r(z_2 - z_1)} \ln\left(\frac{x_2 + p_r z_2 - s_r}{x_1 + p_r z_1 - s_r}\right) \quad (3.26)$$

$$h_{r,z} = p_r h_{r,x} \quad (3.27)$$

$$g_{r,x} = \int_{\Gamma_n} \frac{\partial}{\partial x} \frac{1}{z_r - s_r} d\Gamma_n = \frac{l}{(x_2 - x_1) + p_r(z_2 - z_1)} \left[-\frac{1}{x_2 + p_r z_2 - s_r} + \frac{1}{x_1 + p_r z_1 - s_r}\right] \quad (3.28)$$

$$g_{r,z} = p_r g_{r,x} \quad (3.29)$$

Again, similar expressions can be found for the corresponding bimaterial substrate.

3.6 Strain Energy Density

During growth of QWR nanostructures, strain energy in the QWR plays an important role. Therefore, its calculation and prediction are of great interest. Following [Mur87], the strain energy in the QWR can be expressed as

$$W = \frac{1}{2} \int_V \sigma_{ij} (\gamma_{ij} - \gamma_{ij}^*) dV \quad (3.30)$$

We remark that the integrand $\frac{1}{2}\sigma_{ij}(\gamma_{ij} - \gamma_{ij}^*)$ is the strain energy density within the QWR, which will be also calculated and studied.

Applying the Gauss divergence theorem and assuming that the eigenstrain is uniform inside the QWR, the total elastic strain energy of QWR in Eq. (3.30) can be expressed alternatively as

$$W = \frac{1}{2} \int_\Gamma t_i u_i d\Gamma - \frac{1}{2} \int_\Gamma t_k^{(fw)} u_k d\Gamma + \frac{1}{2} \int_V C_{ijkl} \gamma_{ij}^* \gamma_{kl}^* dV \quad (3.31)$$

where Γ is the boundary of QWR. While the first boundary integration on the right-hand side of Eq. (3.32) represents the work done by the traction acting on the boundary, the

second boundary integration represents the work done by the traction associated with the eigenstrain as we recall that $t_k^{(fw)} = C_{ijkl}\gamma_{ij}^* n_l$. The last volumetric integration corresponds to the initial constant strain energy of the eigenstrain field, i.e., the constant strain energy in the wetting layer (i.e., the thin layer covers the substrate) due to the misfit strain [Hol99].

In QWR growth, one of the important parameters is the relative strain energy Λ [Hol99, Sta04]. Namely, the ratio of the strain energy change relative to the constant strain energy in the wetting layer due to the misfit strain over the constant strain energy, as defined below

$$\Lambda \equiv \frac{W - \frac{1}{2}\int_V C_{ijkl}\gamma_{ij}^*\gamma_{kl}^* dV}{\frac{1}{2}\int_V C_{ijkl}\gamma_{ij}^*\gamma_{kl}^* dV} = \frac{\frac{1}{2}\int_\Gamma t_i u_i d\Gamma - \frac{1}{2}\int_\Gamma t_k^{(fw)} u_k d\Gamma}{\frac{1}{2}\int_V C_{ijkl}\gamma_{ij}^*\gamma_{kl}^* dV} \tag{3.32}$$

where Λ is also called the relative strain energy, which will be numerically examined in the next section. We remark that while various energetic parameters were introduced for characterizing defect dynamics [Phi01], this relative strain energy has been successfully applied in the prediction of new QWR formation and QWR array patterns under the Stranski-Krastanow growth mode [Hol99, Sta04, Yan03b].

3.7 Numerical Examples

Before applying our solution to examine the strain energy in QWR system, we have first checked our program for the reduced cases with existing solutions [Pan04b]. The test example is InAs QWR with size 20nm by 20nm embedded in half-space GaAs substrate. The boundary condition is assumed to be traction free on the half-space surface. The

strain field along the dash line in Fig. 3.2 are calculated and compared with results in [Pan04b]. From Fig. 3.3, we can see the two solutions match each other very well. Other numerical tests have also carried out, all showing that our solution and program are correct.

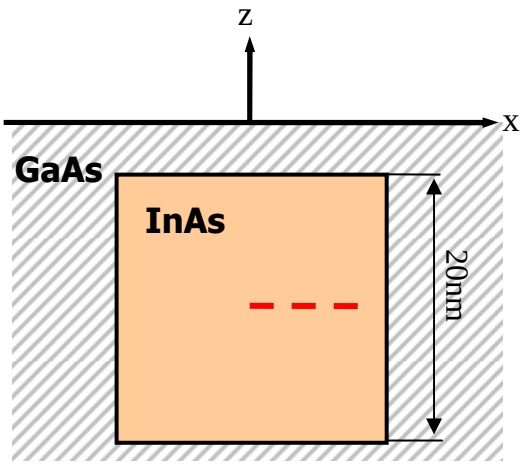

Figure 3.2 A square InAs QWR embedded in GaAs substrate.

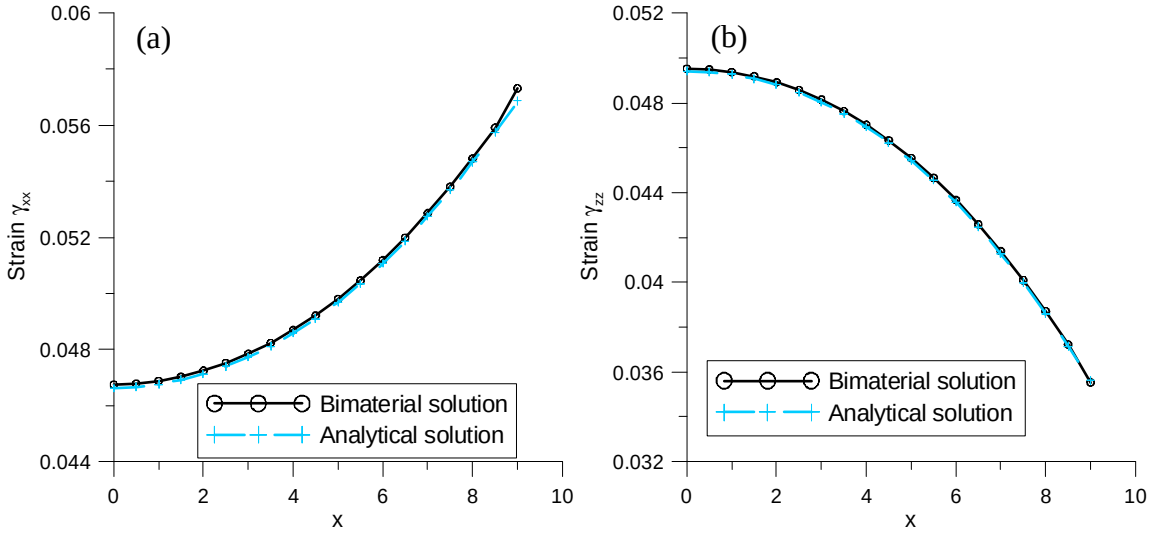

Figure 3.3 Strain comparison of bimaterial solution and analytical solution (a)γ_{xx} (b)γ_{zz}.

Therefore, after validation, we now apply our solution to calculate the relative strain energy and the distribution of the strain energy density. We remark that while our BEM formulation can be applied to more complicated situations, here we only study the reduced case where the QWR is free-standing on or embedded in the half-plane substrate. The half-plane model is reduced from our bimaterial result by setting the upper half-plane (z>0) with very low material stiffness as compared to the lower half-plane substrate (The material stiffness in the upper half-space is equal to 10^{-10} times the material stiffness in the lower half-space).

3.7.1 Variation of Relative Strain Energy with QWR Depth

We first apply our bimaterial BEM program to study the problem where a square InAs(111) QWR growing on a GaAs(111) substrate (Figure 3.4). The material properties of InAs and GaAs in the (111)-direction are obtained by coordinate transform from those in the (001)-directions [Pan07]. The QWR has a dimension of 20nm×20nm and a uniform misfit strain field $\gamma^*_{xx} = \gamma^*_{yy} = \gamma^*_{zz}$ =0.07. The boundary condition on the surface of the substrate is assumed to be traction-free. While a total free-standing QWR on the substrate is illustrated in Figure 3.4a, a fully embedded QWR is shown in Figure 3.4c. We let *d* be the depth of the QWR, measured from the bottom side of the QWR to the surface of substrate (Figure 3.4b). We then calculate the relative strain energy (i.e., Eq. 3.32) of the QWR as a function of depth *d*, varying from -10nm (Figure 3.4a) to 70nm, at the interval of 5nm. Figure 3.5 shows clearly that with increasing depth *d*, the magnitude of the relative strain energy increases, reaching the value when the QWR is within an infinite substrate (=-0.19). In other words, bringing an embedded QWR to the surface will

decrease the relative strain energy. This is true since with increasing surface area of the QWR to the air, more surface energy will be released, resulting in small relative strain energy. This important feature could represent the competition between the surface and bulk energies i.e. [Pao06a, Pao06b], and should be particularly interesting to epitaxial growth.

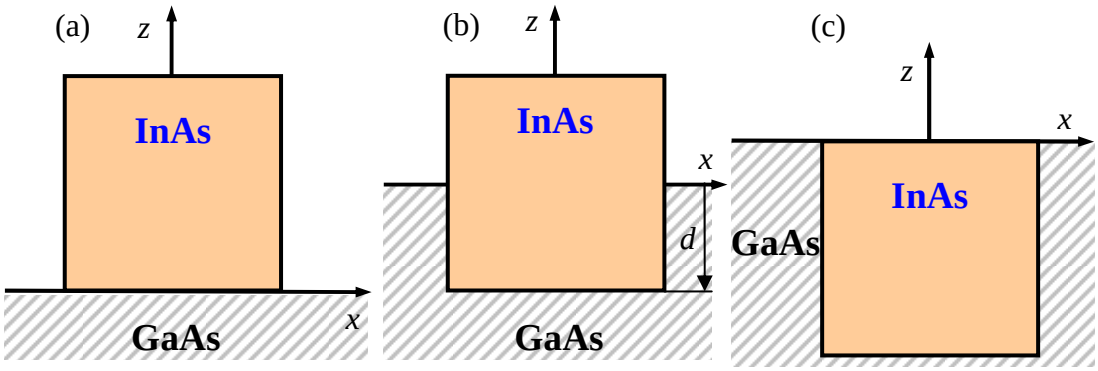

Figure 3.4 Geometry of a square InAs QWR on or inside the GaAs substrate. Shown in (a) to (c) are the three special cases: Namely, totally free-standing (a), half free-standing (half-in and half-out in (b)), and fully embedded (c).

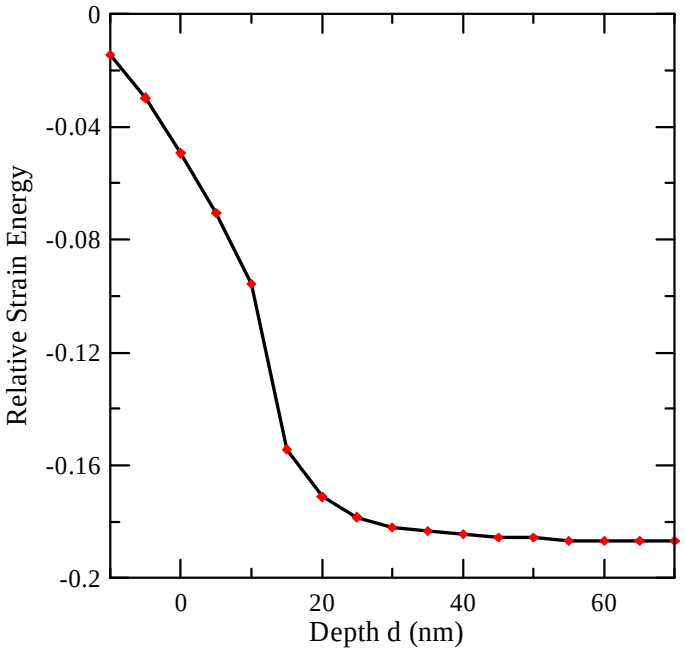

Figure 3.5 Variation of relative strain energy with depth of a square QWR.

3.7.2 Effect of QWR Shape on Relative Strain Energy and Distribution of Strain Energy Density

We assume now that there is an isosceles triangle of InAs (111) QWR, free-standing on the GaAs (111) substrate. The base angle of the triangle varies from 30° to 75° while the area of triangle maintains the same. The misfit strain is again uniform, i.e. γ_{xx}^{*} = $\gamma_{yy}^{*} = \gamma_{zz}^{*}$ =0.07. The boundary condition on the surface of the substrate is traction-free. Both the relative strain energy and strain energy density in the QWR are investigated.

The relative strain energy for the triangular QWR with different base angles are listed in Table 3.1 and its variation with the base angle are also shown in Figure 3.6. It is observed that the magnitude of the relative strain energy increases with increasing base angle of the QWR triangle. In other words, the steeper the QWR is, the larger the magnitude of the relative strain energy becomes.

Table 3.1 Variation of relative strain energy with base angle of the isosceles triangle of InAs (111) QWR, which is free-standing on the GaAs (111) substrate.

Base angle (degree)	Relative strain energy
30	-5.88E-03
37	-6.91E-03
45	-7.90E-03
52	-8.70E-03
60	-9.76E-03
67	-1.11E-02
75	-1.43E-02

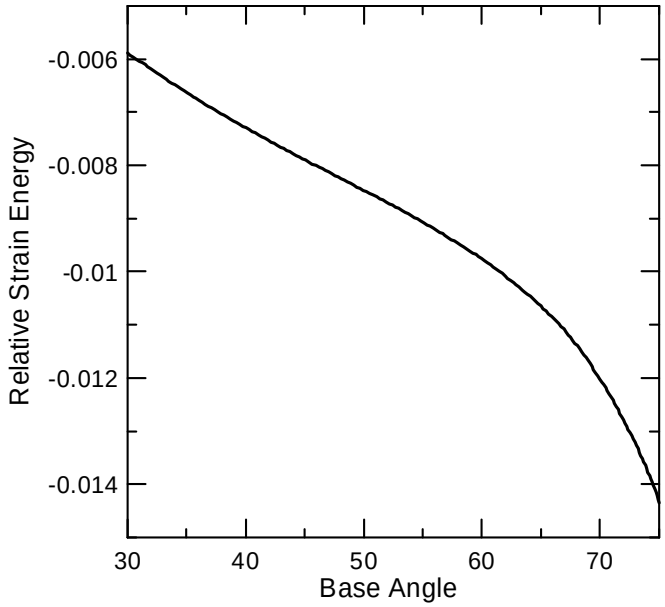

Figure 3.6 Variation of relative strain energy with base angle of isosceles triangle of InAs (111) QWR, which is free-standing on the GaAs (111) substrate.

The contours of the strain energy density for these free-standing triangular QWRs are plotted in Figure 3.7. It is clear that the strain energy density distribution is strongly influenced by the QWR shape. Particularly at the locations near the vertex and base corners, the strain energy densities are quite different among these triangles. We further observed that the strain energy density near the vertex is larger than those near the base corners. The magnitude of strain energy density increases roughly from 2.15 to 2.35 (10^9kg/ms^2) as the base angle varies from 30° to 75°.

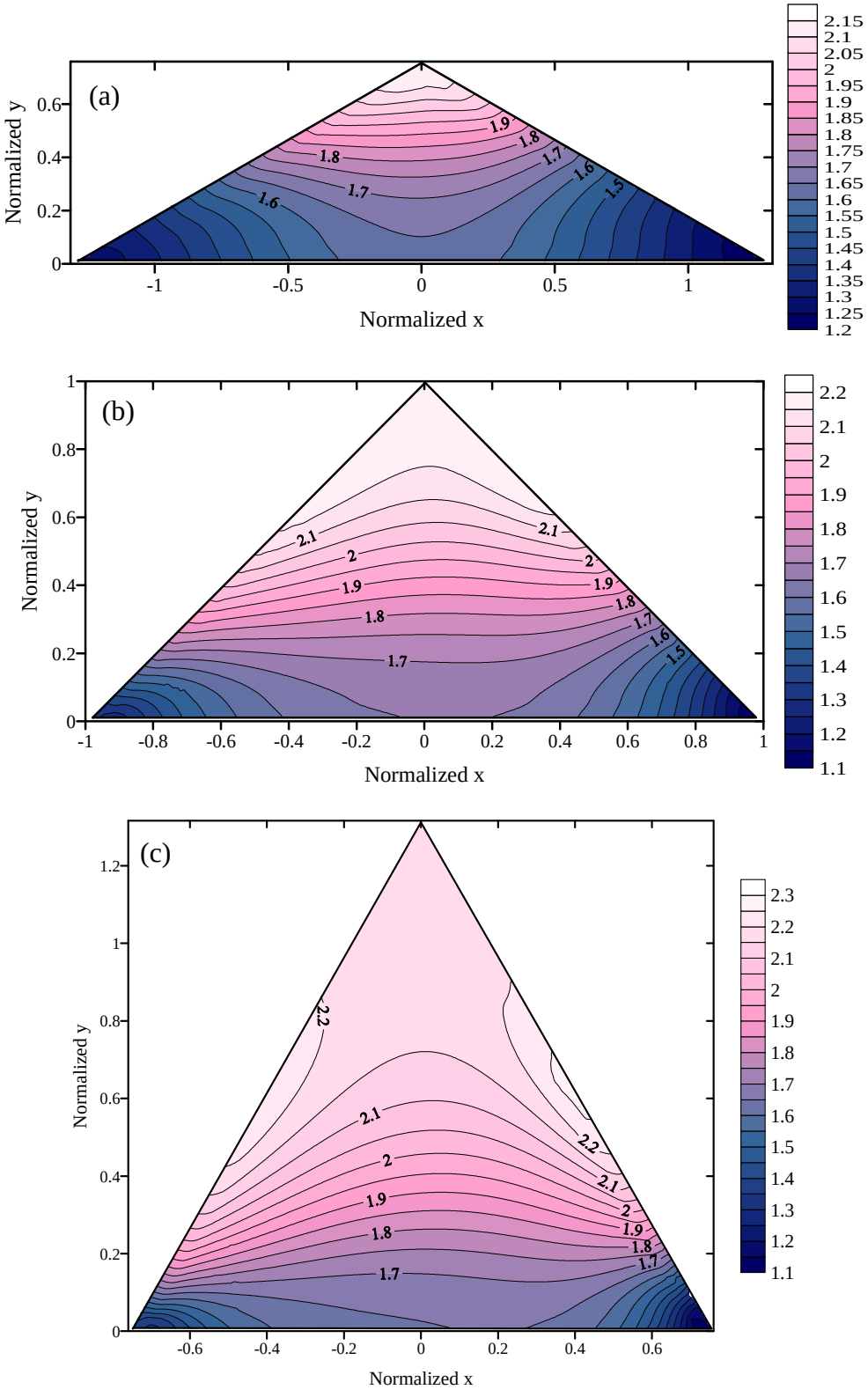
(a)
Normalized y
Normalized x
0
0.2
0.4
0.6
-1
-0.5
0
0.5
1
1.9
1.8
1.7
1.6
1.5
2.15
2.1
2.05
2
1.95
1.9
1.85
1.8
1.75
1.7
1.65
1.6
1.55
1.5
1.45
1.4
1.35
1.3
1.25
1.2
(b)
Normalized y
Normalized x
0
0.2
0.4
0.6
0.8
1
-1
-0.8
-0.6
-0.4
-0.2
0
0.2
0.4
0.6
0.8
1
2.1
2
1.9
1.8
1.7
1.6
1.5
2.2
2.1
2
1.9
1.8
1.7
1.6
1.5
1.4
1.3
1.2
1.1
(c)
Normalized y
Normalized x
0
0.2
0.4
0.6
0.8
1
1.2
-0.6
-0.4
-0.2
0
0.2
0.4
0.6
2.2
2.1
2
1.9
1.8
1.7
2.3
2.2
2.1
2
1.9
1.8
1.7
1.6
1.5
1.4
1.3
1.2
1.1

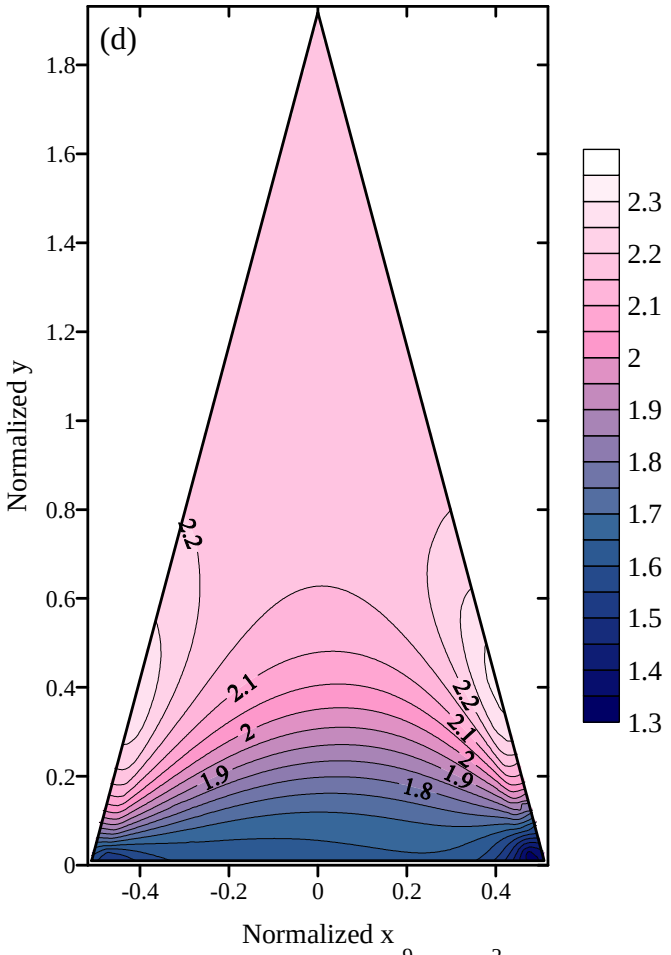

Figure 3.7 Contours of strain energy density (10^9kg/ms^2) in isosceles triangle of InAs (111) QWR with base angle 30°(a), 45°(b), 60°(c), and 75°(d).

3.8 Conclusions

In the chapter, we first derive the bimaterial Green's functions in anisotropic elastic media in terms of the elegant Stroh formalism. The corresponding BEM formulation is then presented. Since the involved Green's functions are in exact closed forms, the kernel integration can be analytically carried out for the constant element discretization. After testing our bimaterial BEM program for various reduced simple cases, we then apply our program to calculate the strain energy density and the relative strain energy in InAs (111) QWR free-standing on or embedded in GaAs (111) substrate. Our numerical results

showed that, for the case of an isosceles triangle of InAs (111) QWR on the substrate, the strain energy density within the QWR strongly depends on the base angle of the triangle. We also observed that the magnitude of the relative strain energy for this case increases with increasing base angle. For a square QWR either free standing on or embedded in the substrate, we found that the magnitude of the relative strain energy increases with increasing depth of the QWR in the substrate, which represents the competition between the surface and bulk energies. Our numerical examples also demonstrate the significant influence of the QWR shape and location on both the strain energy density and the relative strain energy in the QWR, which should be particularly useful to the successful growth of QWRs via epitaxial approach.

CHAPTER IV

STAIN ENERGY ON THE SURFACE OF HALF-SPACE SUBSTRATE INDUCED BY AN ISOLATED QD

4.1 Summary

Novel superlattice-based quantum devices have attracted considerable attention in recent years [Bim98, Sta04, Jal05; Fer07] where quantum dots, nanowires and nanorods have been intensively investigated [Leo93, Gos95, Bax05]. Self-assembled quantum dots have been of particular interest because of their three-dimensional confinement of charge carriers and excitons and hence their potential in nano-scale electronic devices [Pet03, Fri07, Lev07].

It is well known that the elastic fields produced by QDs substantially influence surface feature formations that consequently affect the electronic band structure. As either a detector or emitter of electromagnetic signals, the bandgap energy determines the operational wavelength in say, the photovoltaic mode, of the element. Hence, the elastic fields induced by QDs have to be studied in order to obtain a well ordered QD structure. To analyze the elastic fields in and around the QDs and other quantum structures, several methods have been proposed, such as the finite element and finite difference methods, atomistic modeling, and analytical approaches. In particular, the Green's function solutions have been proposed and applied to QD studies [Pan01)]. Because of their

accuracy and efficiency, the analytical methods, particularly the Green's function method, are arguably more appealing to experimentalists and physical device designers in the studies of QD structures [And99, Pea00]. More recently, the multiscale Green's functions have been also introduced to model QD-induced strain field [Tew04a, Tew04b, Yan05, Rea07], which have been shown to be computationally efficient. However, while the lattice Green's functions have been well-developed so far, the corresponding continuum Green's functions still require further study, particularly when considering semiconductor anisotropy.

In this chapter, we present an analytical method for the QD-induced strain field in half-space semiconductor substrates under the assumption of continuum elasticity. Furthermore, under the epitaxial growth, the misfit strain within the QD could be gradient, instead of uniform distribution [Mal03], and as such, the material property in the QD could be difficult to calibrate [Zhu06]. Thus, the well-know inclusion model will be adopted in this chapter. It was verified recently that the inclusion model could predict slightly different results as compared to the inhomogeneity model using the bulk property of the QD (about 10% within the strained quantum structures, see, e.g., [Yan02, Pan05]). Under these assumptions, we derive our solution based on the Green's function method in terms of the Stroh formalism with the corresponding exact integration of the Green's functions over the QD surface (composed of piece-wise flat triangles).

This chapter is organized as follows: In section 4.2, the strained QD system is described. In section 4.3, the surface of the QD is approximated by a number of flat triangles over which the area integration is carried out exactly so that the induced elastic fields can be expressed in terms of a simple line integral over $[0, \pi]$. If the QD is a point

source, then the QD-induced elastic fields can be analytically expressed by point-force Green's functions in the half-space. In section 4.4, numerical examples are carried out for buried cubic, pyramidal, truncated pyramidal, and point QDs in half-spaces. The effects of QD shape and depth on the strain energy are discussed. Conclusions are drawn in section 4.5.

4.2 Problem description for QD Embedded in Anisotropic Half-space Substrate

We now assume that the 3D point-force Green's functions are given for the half-space substrate, then for the general eigenstrain γ_{ij}^{*} at $\boldsymbol{x}=(x_1,x_2,x_3)$ within the QD domain V, the induced displacement at $\boldsymbol{d}=(d_1,d_2,d_3)$ can be found using the superposition method. That is, the response is an integral, over V, of the equivalent body force defined by (2.17), multiplied by the point-force Green's functions, as

$$u_k(\boldsymbol{d}) = -\int_V U_j^k(\boldsymbol{x};\boldsymbol{d})[C_{ijlm}\gamma_{lm}^{*}(\boldsymbol{x})]_{,i}\,dV(\boldsymbol{x}) \tag{4.1}$$

where $U_j^k(\boldsymbol{x};\boldsymbol{d})$ is the j-th Green's elastic displacement at $\boldsymbol{x}$ due to a point force/ point charge in the k-th direction applied at $\boldsymbol{d}$.

Integrating by parts and noting that the eigenstrain is nonzero only in the QD domain V, Eq. (4.1) can be expressed alternatively as

$$u_k(\boldsymbol{d}) = \int_V U_{j,x_i}^k(\boldsymbol{x};\boldsymbol{d})C_{ijlm}\gamma_{lm}^{*}(\boldsymbol{x})dV(\boldsymbol{x}) \tag{4.2}$$

If we further assume that the eigenstrain is constant within the QD domain V, then the domain integration can be transformed to the boundary integration. That is

$$u_k(\boldsymbol{d}) = C_{ijlm}\gamma_{lm}^{*}\int_{\partial V} U_j^k(\boldsymbol{x};\boldsymbol{d})n_i(\boldsymbol{x})dS(\boldsymbol{x}) \tag{4.3}$$

where $n_i(\boldsymbol{x})$ is the outward normal on the boundary ∂V of the QD.

In order to find the elastic strain, we take the derivatives of Eq. (4.3) with respect to the observation point $\boldsymbol{d}$ (i.e., the source point of the point-force/point charge Green's function), which yields (k,p=1,2,3)

$$\gamma_{kp}(\boldsymbol{d}) = \frac{1}{2}\gamma^*_{lm} C_{ijlm} \int_{\partial V} [U^k_{j,d_p}(\boldsymbol{x};\boldsymbol{d}) + U^p_{j,d_k}(\boldsymbol{x};\boldsymbol{d})] n_i(\boldsymbol{x}) dS(\boldsymbol{x}) \tag{4.4}$$

The stresses inside and outside the QD are obtained from Eq. (2.14).

It is obvious that in order to solve the QD-induced elastic field, the key is to carry out the surface integration involved in (4.3) and (4.4). This requires the integral of the corresponding half-space Green's functions.

4.3 Integration of Half-space Green's Functions over QD Surfaces

We assume that the boundary of the QD can be approximated by a number of flat triangles. We want to analytically integrate the half-space Green's functions over one of the flat triangles. To do so, we first briefly review the half-space Green's functions in general anisotropic semiconductors.

The half-space point-force Green's function with source point at $\boldsymbol{d}$ and field point at $\boldsymbol{x}$ can be expressed as a sum of an explicit infinite-space solution and a complementary part in terms of a line integral over [0,π] [Pan 02b]

$$\boldsymbol{U}(\boldsymbol{x};\boldsymbol{d}) = \boldsymbol{U}^{\infty}(\boldsymbol{x};\boldsymbol{d}) + \frac{1}{2\pi^2}\int_0^{\pi} \overline{\boldsymbol{A}}\boldsymbol{G}_1\boldsymbol{A}^T d\theta \tag{4.5}$$

where overbar means complex conjugate, superscript T denotes matrix transpose, and

$$(\boldsymbol{G}_1)_{ij} = \frac{(\overline{\boldsymbol{B}}^{-1}\boldsymbol{B})_{ij}}{-\overline{p}_i x_3 + p_j d_3 - [(x_1 - d_1)\cos\theta + (x_2 - d_2)\sin\theta]} \tag{4.6}$$

We point out that, on the right-hand side of Eq. (4.5), the first term corresponds to the Green's displacement tensor in an anisotropic infinite space. Its integration over a flat triangle was presented by Wang *et al*. [Wan06]. Also in Eqs. (4.5) and (4.6), the Stroh eigenvalues p_j, and eigenmatrices $\boldsymbol{A}$ and $\boldsymbol{B}$ are all functions of θ, as well as the elastic stiffness tensor of the materials. p_j and $\boldsymbol{A}$ are the solutions of the following eigenrelation

$$[\boldsymbol{Q} + p(\boldsymbol{R} + \boldsymbol{R}^T) + p^2\boldsymbol{T}]\boldsymbol{a} = 0 \tag{4.7}$$

which is exact same as Eq. (2.24), but with

$$Q_{ik} = C_{i\alpha k\beta} n_\alpha n_\beta\,,\ R_{ik} = C_{i\alpha k3} n_\alpha\,,\ T_{ik} = C_{i3k3} \tag{4.8}$$

where

$$(n_1, n_2) = (\cos\theta, \sin\theta) \tag{4.9}$$

and α and β taking the values of 1 and 2. We noted that, due to the positive requirement on the strain energy density, the eigenvalues of Eq. (4.7) are either complex or purely imaginary.

In order to find the misfit strain-induced elastic fields, we also need the derivatives of the Green's displacement tensor with respect to the field point (x_1, x_2, x_3) of the Green's function. They are found to be (j=1, 2, 3)

$$\frac{\partial \boldsymbol{U}(\boldsymbol{x};\boldsymbol{d})}{\partial x_j} = \frac{\partial \boldsymbol{U}^\infty(\boldsymbol{x};\boldsymbol{d})}{\partial x_j} - \frac{1}{2\pi^2}\int_0^\pi \overline{\boldsymbol{A}}\boldsymbol{G}_2\langle g_j\rangle \boldsymbol{A}^T d\theta \tag{4.10}$$

where

$$(\boldsymbol{G}_2)_{ij} = \frac{(\overline{\boldsymbol{B}}^{-1}\boldsymbol{B})_{ij}}{\{-\overline{p}_i x_3 + p_j d_3 - [(x_1 - d_1)\cos\theta + (x_2 - d_2)\sin\theta]\}^2} \tag{4.11}$$

$$\begin{aligned} \langle g_1 \rangle &= diag[\cos\theta, \cos\theta, \cos\theta] \\ \langle g_2 \rangle &= diag[\sin\theta, \sin\theta, \sin\theta] \\ \langle g_3 \rangle &= diag[\overline{p}_1, \quad \overline{p}_2, \quad \overline{p}_3] \end{aligned} \tag{4.12}$$

Again, since the integration on a flat triangle has already been presented for the infinite part of the half-space Green's function [Wan06], we only need to present the integration of the complementary part of the Green's function, i.e., the integration of the second term on the right-hand side of Eq. (4.10).

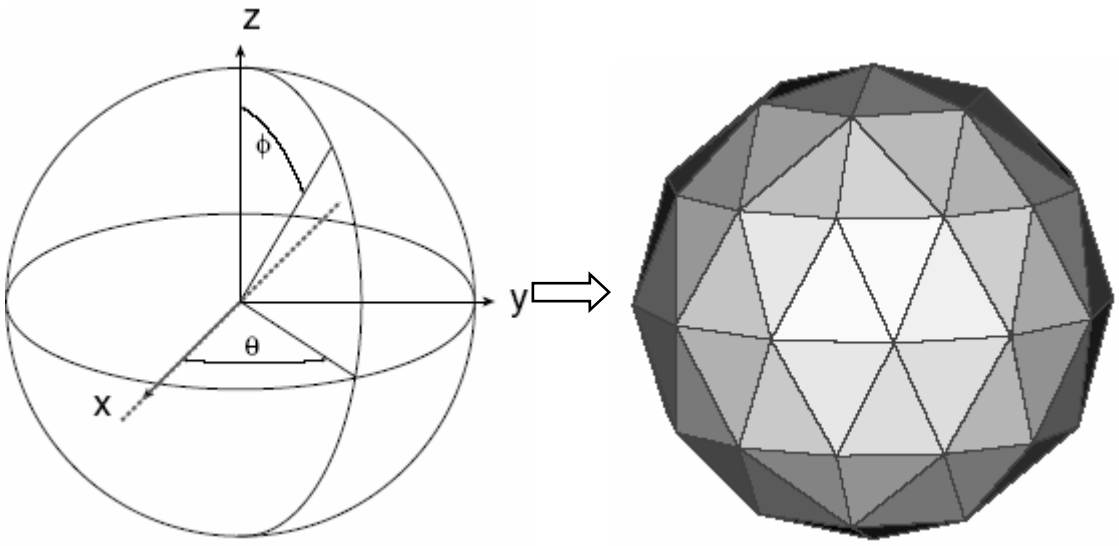

Figure 4.1 Sphere surface approximated by a number of flat triangles.

We consider first the integration of the Green's displacement tensor. Again, we assume that the QD surface can be effectively approximated by a number of flat triangles (Fig. 4.1). Therefore, the integral expression Eq. (4.3) over a flat triangle, Δ, is

$$u_k(\boldsymbol{d}) = C_{ijlm}\gamma^*_{lm} n_i \int_{\Delta} U^k_j(\boldsymbol{x};\boldsymbol{d}) dA(\boldsymbol{x}) \tag{4.13}$$

where n is the outward normal to Δ. Substituting Eq. (4.5) into (4.13) and changing the integration orders, the contribution from the complementary part can be expressed as

$$u_k(\boldsymbol{d}) = \frac{1}{2\pi^2} C_{ijlm} \gamma^*_{lm} n_i \int_0^{\pi} \overline{\boldsymbol{A}} \left[\int_{\Delta} \boldsymbol{G}_1 d\Delta(\boldsymbol{x}) \right] \boldsymbol{A}^T d\theta \tag{4.14}$$

While the outside line integration can be easily carried out by employing Gaussian quadrature, we discuss the area integration over the flat triangle, which can be done analytically as will be shown below. Actually, since in the expression for $\boldsymbol{G}_1$ in Eq. (4.6), its numerator is a function of θ only, the integration over the flat triangle Δ needs to be carried out for the following expression only

$$F_1(d_j, \theta) = \int_{\Delta} \frac{\mathrm{d}\Delta(\boldsymbol{x})}{-\overline{p}_i x_3 + p_j d_3 - [(x_1 - d_1)\cos\theta + (x_2 - d_2)\sin\theta]} \tag{4.15}$$

Similarly, in order to find the QD-induced strain field, (Eqs. (4.4) and (4.10)), one needs only to carry out the following area integration over the flat triangle.

$$F_2(d_j, \theta) = \int_{\Delta} \frac{\mathrm{d}\Delta(\boldsymbol{x})}{\{-\overline{p}_i x_3 + p_j d_3 - [(x_1 - d_1)\cos\theta + (x_2 - d_2)\sin\theta]\}^2} \tag{4.16}$$

The area integration over a flat triangle in Eqs. (4.15) and (4.16) can be carried out exactly. To do so, we introduce the following transformation between the global coordinate system $\boldsymbol{x}$ (x_1, x_2, x_3) and local coordinate system $\boldsymbol{\xi}$ (ξ_1, ξ_2, ξ_3) associated with the flat triangle (Figure 4.2)

$$\begin{bmatrix} x_1 - x_{01} \\ x_2 - x_{02} \\ x_3 - x_{03} \end{bmatrix} = \begin{bmatrix} a_{11} & a_{12} & a_{13} \\ a_{21} & a_{22} & a_{23} \\ a_{31} & a_{32} & a_{33} \end{bmatrix} \begin{bmatrix} \xi_1 \\ \xi_2 \\ \xi_3 \end{bmatrix} \tag{4.17}$$

Then, the integration becomes (n=1,2)

$$F_n(d_j,\theta)=\int_0^h d\xi_2 \int_{-l_1+l_1\xi_2/h}^{l_2-l_2\xi_2/h} d\xi_1 \frac{1}{[\mathrm{f}_1(d_j,\theta)\xi_1+\mathrm{f}_2(d_j,\theta)\xi_2+\mathrm{f}_3(d_j,\theta)]^n} \tag{4.18}$$

where

$$f_1(d_j,\theta)=-(\overline{p}_i a_{31}+a_{11}\cos\theta+a_{21}\sin\theta) \tag{4.19}$$

$$f_2(d_j,\theta)=-(\overline{p}_i a_{32}+a_{12}\cos\theta+a_{22}\sin\theta) \tag{4.20}$$

$$\begin{aligned} f_3(d_j,\theta)=&-\overline{p}_i(x_{03}+a_{33}\xi_3)+p_j d_3+d_1\cos\theta+d_2\sin\theta \\ &-(x_{01}+a_{13}\xi_3)\cos\theta-(x_{02}+a_{23}\xi_3)\sin\theta \end{aligned} \tag{4.21}$$

The integration can now be carried out, and the results are

$$F_1(d_j,\theta)=\frac{1}{f_1}\left[\frac{f_1 l_2+f_3}{f_2-f_1 l_2/h}\ln\left(\frac{f_2 h+f_3}{f_1 l_2+f_3}\right)-\frac{-f_1 l_1+f_3}{f_2+f_1 l_1/h}\ln\left(\frac{f_2 h+f_3}{-f_1 l_1+f_3}\right)\right] \tag{4.22}$$

$$F_2(d_j,\theta)=\frac{1}{f_1}\left[\frac{1}{f_2+f_1 l_1/h}\ln\left(\frac{f_2 h+f_3}{-f_1 l_1+f_3}\right)-\frac{1}{f_2-f_1 l_2/h}\ln\left(\frac{f_2 h+f_3}{f_1 l_2+f_3}\right)\right] \tag{4.23}$$

With these exact expressions, the QD-induced displacement and strain fields can be finally expressed in terms of the line integration over $[0,\pi]$ (e.g., Eq. (4.14) for the induced displacements). Again the line integration can be carried out numerically using 8-point Gaussian quadrature.

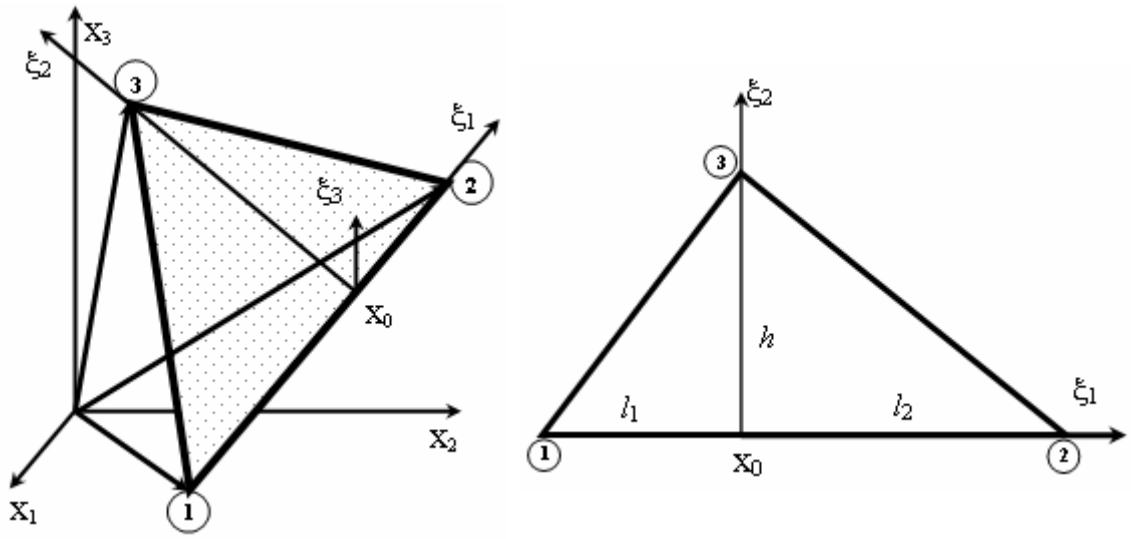

Figure 4.2 Geometry of the flat triangle Δ (with corners 1,2,3), and transformation from the global (x_1,x_2,x_3) to local (ξ_1,ξ_2,ξ_3) coordinates where ξ_3 is along the outward normal direction of the flat triangle.

4.4 Numerical Examples

We now apply our analytical solutions to calculate the strain energy induced by a buried QD within the GaAs half-space substrate. The surface of the substrate is traction free. The QD is located at depth *d* below the surface (Figure 4.3) and the misfit strain is hydrostatic, i.e. $\gamma^*_{xx} = \gamma^*_{yy} = \gamma^*_{zz} = 0.07$. We point out that this misfit strain is relatively large and the corresponding nonlinear influence will be pursued using other methods, such as the multiscale meshless method [She04]. As for the QD shape, we assume it to be either cubic, pyramidal, truncated pyramidal, or point type. The QDs have the same height *h* (=4nm, except for point QD). To make all the QDs (including the point QD) have the same volume, we have the base length 2.155*h* for cubic QD, upper length 1.79*h* and lower length 2.5*h* for truncated pyramid QD, base length 3.732*h* for pyramid QD (Figure 4.3). For the point QD case, it is located at the middle height of the cubic QD (i.e.,

its vertical distance to the surface is $d+h/2$). We studied the effect of the QD shape and depth on the strain energy on the surface.

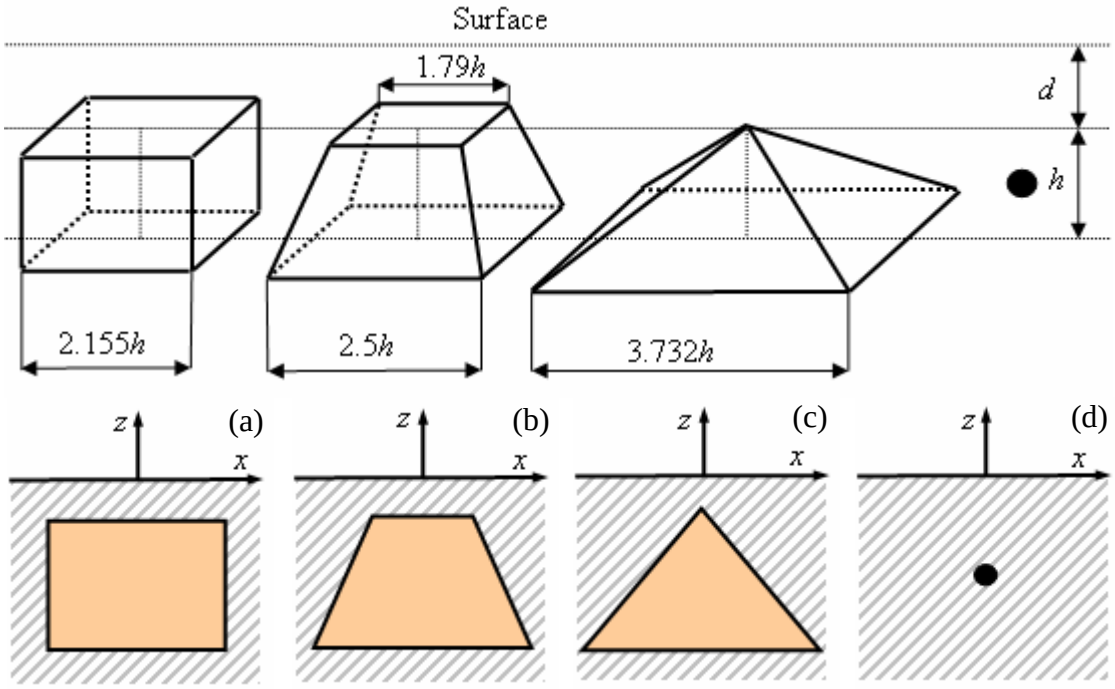

Figure 4.3 Geometry for (a) a cubic QD, (b) a truncated pyramid QD, (c) a pyramid QD, and (d) a point QD. Top row is the 3D view and bottom row is the vertical *x*-*z* plan view. All these QDs have the same volume.

Shown in Figures 4.4a-4.4d are, respectively, contours of the normalized strain energy on the surface of GaAs (001) (top row) and GaAs (111) (bottom row), induced by a buried cubic, truncated pyramidal, pyramidal or point type QD. In this example, the depth d=2nm, height h=4nm, and the strain energy is normalized by 118.8×10^{15}Nm (this normalization factor is also used below for the strain energy) (Table 4.1). It is clear that different QD shapes (including point QD) induce different strain energy distributions on the surface of the substrate. Besides the difference on the contour shape, the strain energy values are also different. For example, the contours with value 0.3, 0.6 and 0.9

(corresponding, respectively, to the heavy blue, red and black curves) move towards the center when the QD shape changes from left to right (i.e., cubic, truncated pyramid, pyramid, and point type). Table 4.1 lists the maximum strain energy values corresponding to different QD shapes at different depths within the GaAs substrate with both (001) and (111) orientations. It is clear, from Table 4.1, that while the induced maximum strain energy value decreases with increasing depth, its value on the substrate GaAs (001) is always larger than that of the corresponding inclined substrate GaAs (111). Furthermore, the effect of the QD shapes (cubic, truncated pyramid, pyramid, and point QD) on the strain energy is complicated, as can be seen from Figs. 4.3a-4.3d. Also from Figs. 4.4a-4.4d, it is observed, by comparing the top row to the bottom row, that the strain energy contour lines of equal value all move towards the center, and that the contours shapes of the strain energy over GaAs (001) are sharply different to those over GaAs (111).

Table 4.1 Maximum strain energy E_{max} on the surface of the substrate GaAs for different QD shapes with different depths (unit of energy=118.8×10^{15}Nm).

Depth			Cubic	Truncated pyramid	Pyramid
d=1nm	(001)	E_{max}	2.54	2.93	2.71
		(x,y)	$(\pm1,\pm1)$	$(\pm1,\pm1)$	(0,0)
	(111)	E_{max}	2.55	2.75	2.05
		(x,y)	(1,0)	(1,0)	(0,0)
d=2nm	(001)	E_{max}	1.77	1.99	0.96
		(x,y)	(0,0)	(0,0)	(0,0)
	(111)	E_{max}	1.31	1.34	0.75
		(x,y)	(0,0)	(0,0)	(0,0)
d=3nm	(001)	E_{max}	1.03	1.09	0.41
		(x,y)	(0,0)	(0,0)	(0,0)
	(111)	E_{max}	0.70	0.70	0.36
		(x,y)	(0,0)	(0,0)	(0,0)

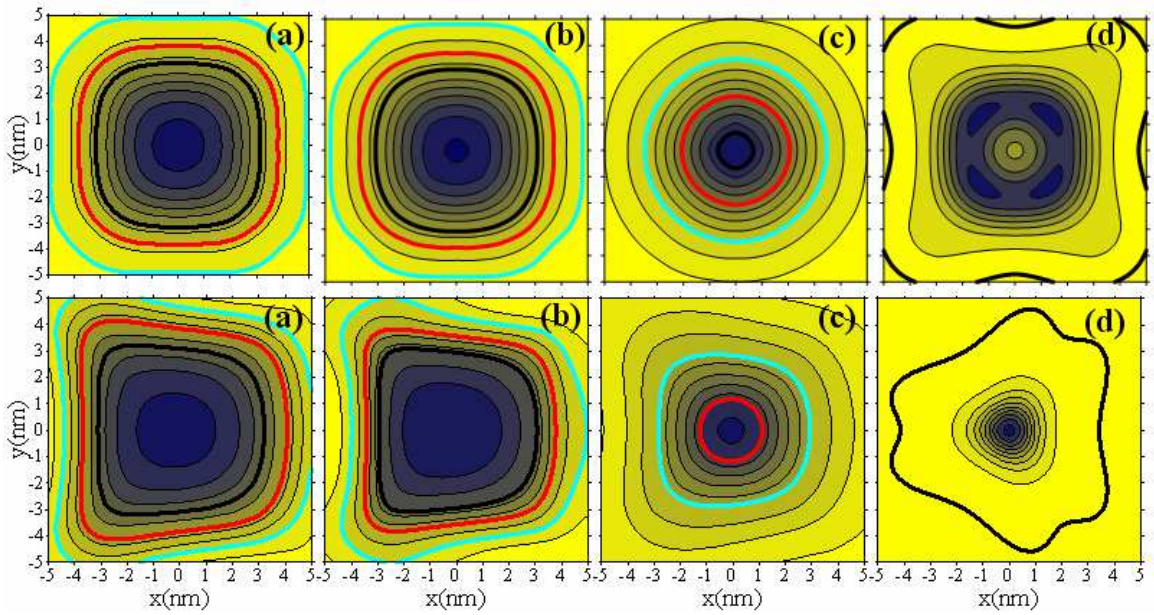

Figure 4.4 Normalized strain energy on the surface of the half-space substrate of GaAs (001) (top row) and GaAs (111) (bottom row) induced by (a) a cubic, (b) a truncated pyramid, (c) a pyramid, and (d) a point QD, where the heavy blue, red and black lines correspond to normalized strain energy of 0.3, 0.6 and 0.9 respectively. The QD is embedded within the substrate with its top side at a depth d=2nm from the surface.

We now study the effect of QD depth on the strain energy distribution on the surface. The top row of Fig. 4.5 shows the depths of cubic QD within the substrate where d=1nm, 2nm, and 3nm, whilst the strain energy distributions on the surface of GaAs (001) and (111) are shown, respectively, in the middle and bottom rows. Again, the heavy blue, red and black contour lines correspond, respectively, to the strain energy values of 0.3, 0.6, and 0.9. It is apparent from Fig. 4.5 that as the QD moves away from the surface, the strain energy contours approach to those due to a point QD with equal volume.

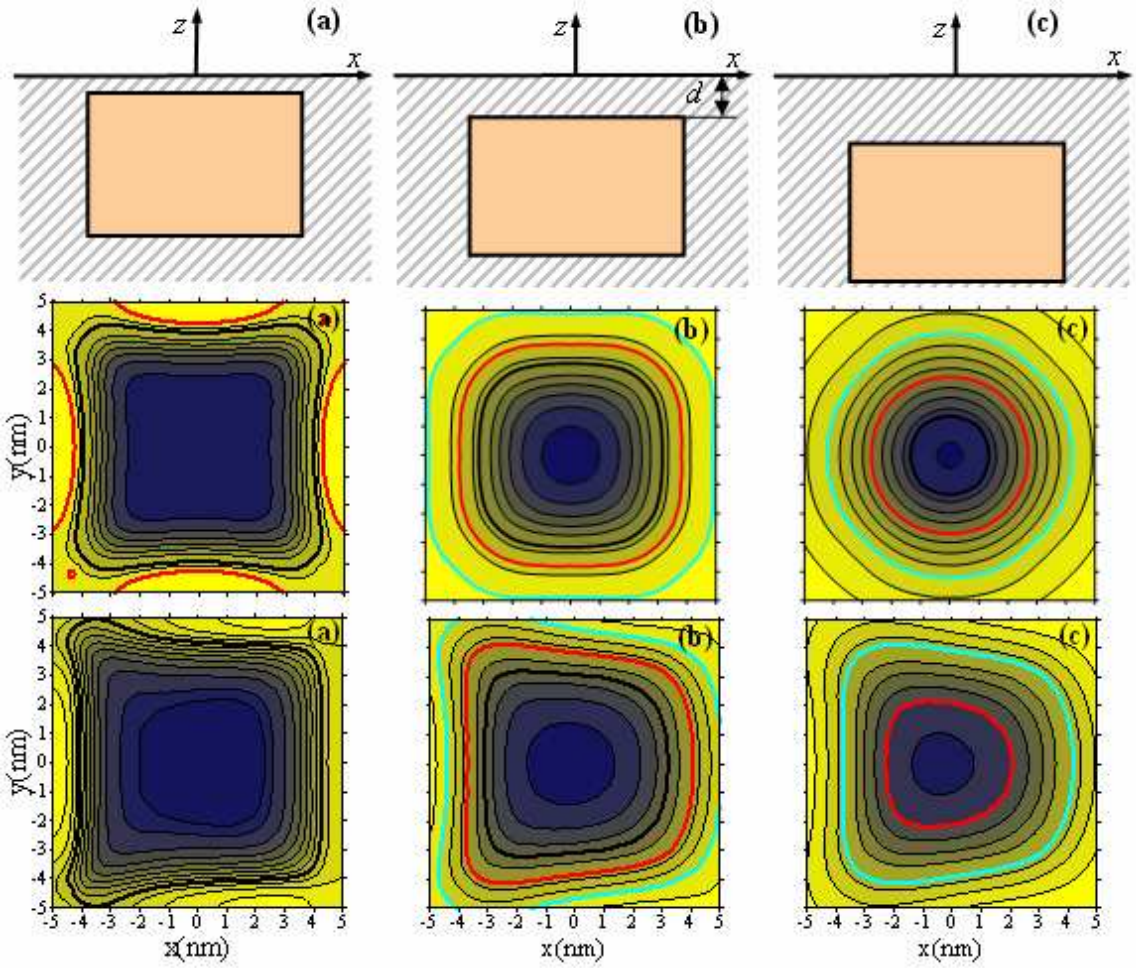

Figure 4.5 Geometry of a cubic QD within a half-space substrate with different depth *d*: the vertical *x*-*z* plan view (top row), and the strain energy induced by the cubic QD in substrate GaAs(001) (middle row) and GaAs (111) (bottom row): (a) *d*=1, (b) *d*=2, and (c) *d*=3. The heavy blue, red and black lines correspond to normalized strain energy of 0.3, 0.6 and 0.9 respectively.

Similar numerical results are shown in Figs. 4.6 and 4.7, respectively, for the truncated pyramidal and pyramidal QDs. While the strain energy distributions induced by the pyramidal QD are similar to those by an equivalent-volume QD, those by cubic and truncated pyramidal QD are different. These again demonstrate the effect of the QD shape and depth on the strain energy.

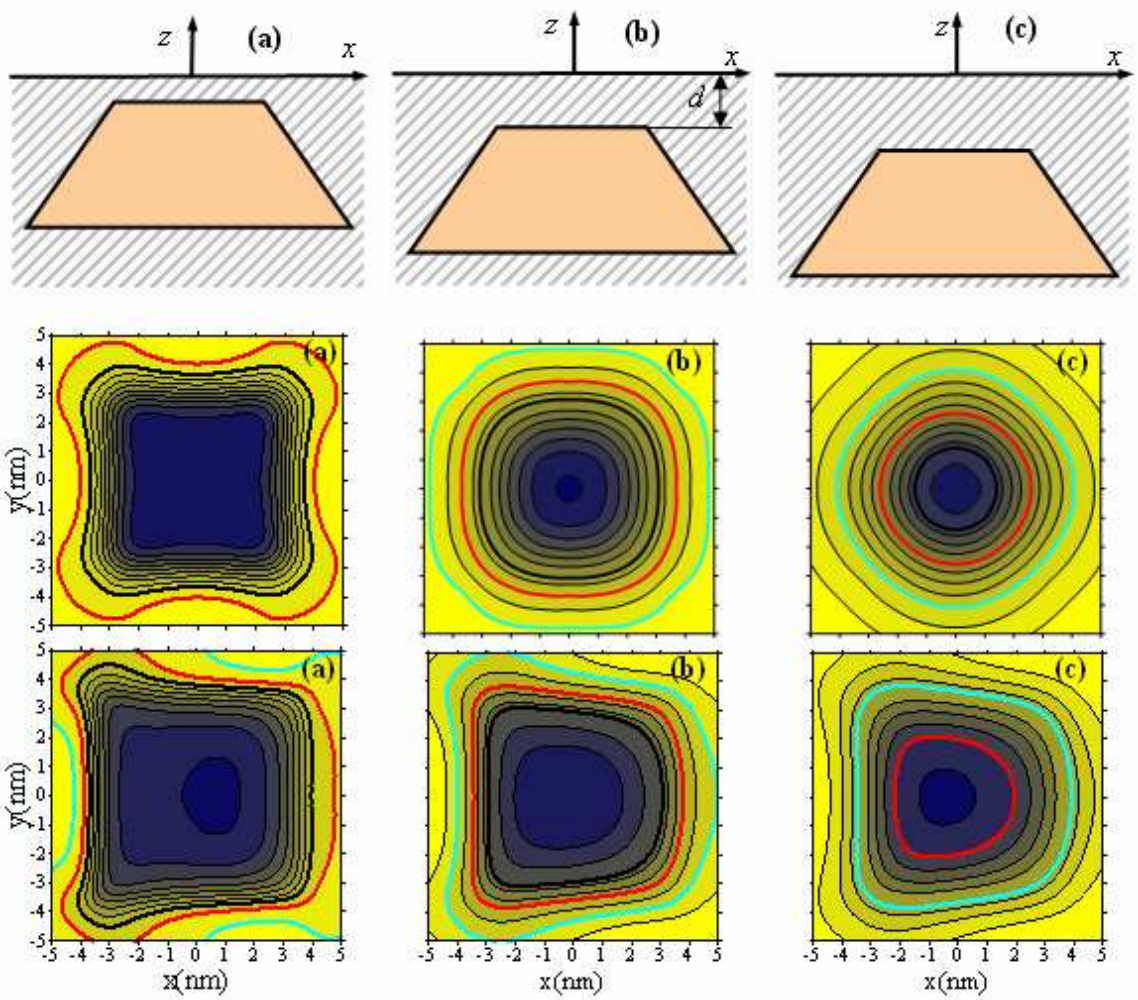

Figure 4.6 Geometry of a truncated pyramid QD within a half-space substrate with different depth *d*: the vertical *x*-*z* plan view (top row), and the strain energy induced by the truncated pyramid QD in substrate GaAs(001) (middle row) and GaAs (111) (bottom row): (a) *d*=1, (b) *d*=2, and (c) *d*=3. The heavy blue, red and black lines correspond to normalized strain energy of 0.3, 0.6 and 0.9 respectively.

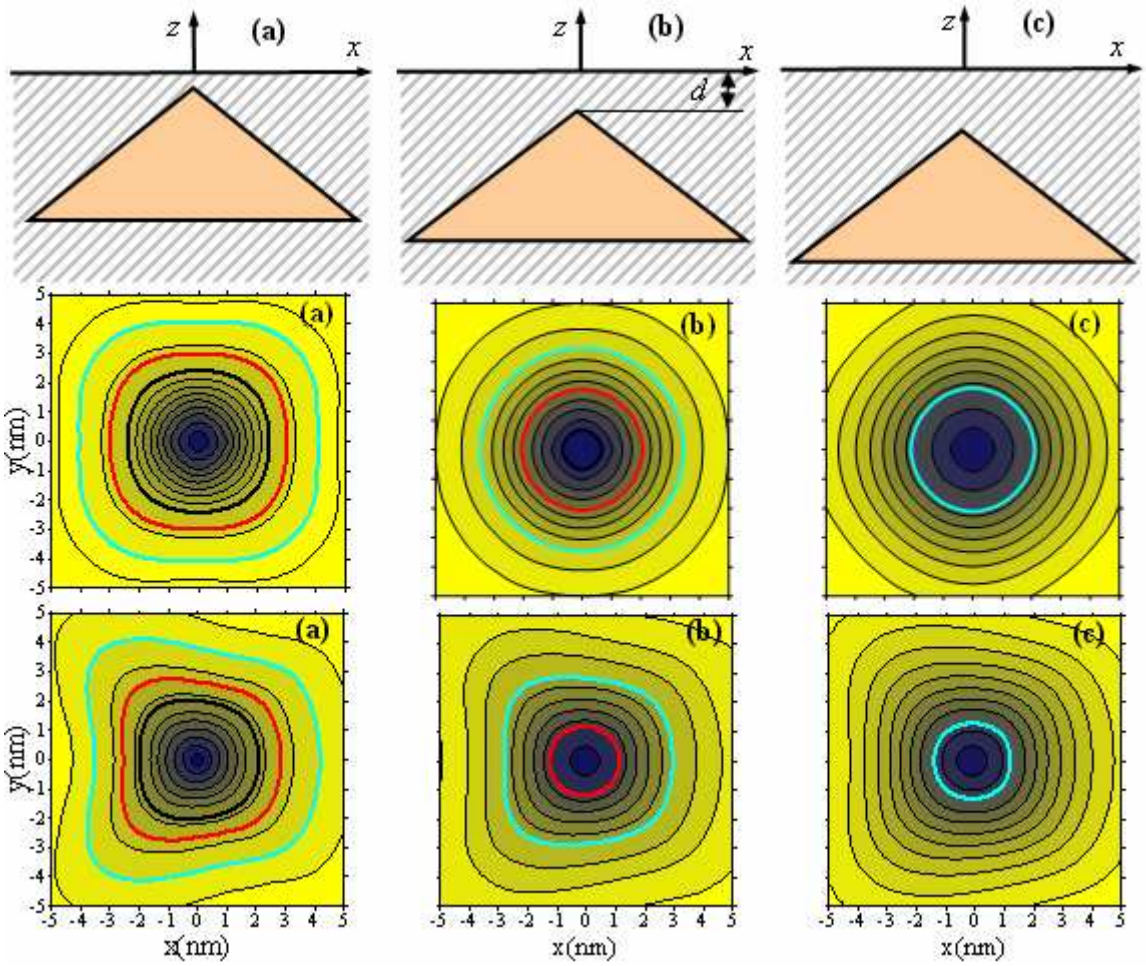

Figure 4.7 Geometry of a pyramid QD within a half-space substrate with different depth *d*: the vertical *x*-*z* plan view (top row), and the strain energy induced by the pyramid QD in substrate GaAs(001) (middle row) and GaAs (111) (bottom row): (a) *d*=1, (b) *d*=2, and (c) *d*=3. The heavy blue, red and black lines correspond to normalized strain energy of 0.3, 0.6 and 0.9 respectively.

4.5 Conclusions

In this chapter, we presented an analytical method for calculating the QD-induced strain fields in half-space semiconductor substrates. The QD is assumed to be of any polyhedral shape which can be efficiently approximated by a number of flat triangles. We studied cubic, pyramidal, truncated pyramidal and point QDs within the GaAs (001) and

GaAs (111) half-space substrates. The numerical results illustrate that the shape of the QDs has apparent influence on the strain energy distribution on the surface, so is the depth of the QDs. These results should be interesting to the overgrowth of QDs on the substrate where the long-range strain energy on the surface plays an important role in controlling the new QD patterns and shapes.

CHAPTER V

THREE-DIMENSIONAL STRAIN AND PIEZOELECTRIC FIELDS IN NITRIDE-BASED QUANTUM DOTS

5.1 Summary

Group III nitride-based quantum dots structures have been of major interest in recent years because of their ability to produce high-quality light emitting and laser diodes [Con00, Med02, Not95]. This has been largely stimulated by the progress in self-assembly quantum dot growth. In order to achieve uniform dots in size, shape and density, much work still needs to be done to understand the growth of these structures. Theoretical study of the elastic and electric fields in and around the quantum dots is now of the focus interest because it can serve as a useful tool to guide the QDs' growth and also to understand their properties [Jon06, Mak01, Zha05, Pan07, Pan08].

In this chapter, a simple and elegant method for the detailed analysis of the strain and piezoelectric field in electronic structure of AlN QDs is employed. It's based on the Green's function in terms of Stroh formalism with the corresponding exact integration of the Green's function over the QD surface. This method takes into account quantum dots of arbitrary shape with the most general class of anisotropy and piezoelectricity.

This chapter is organized as follows. In section 5.2, we develop the method to calculate the 3D fields distributions in and around single or multiple QDs. The results are

given in section 5.3. We first present the field distributions in single QD. The results are in good agreement with previous work. After that, a pair of QDs are studied. Conclusions are drawn in section 5.4.

5.2 Problem Description

Assume that the eigenstrain γ_{Ij}^{*} is uniform within the QD domain V, the induced displacement at point ***d*** can be expressed as boundary integration

$$u_K(d) = C_{iJLm}\gamma_{Lm}^{*}\int_{\partial V} U_J^K(x;d)n_i(x)dS(x) \tag{5.1}$$

Noted that Eq.(5.1) is similar as Eq.(4.1). The difference is that we use the extended notation (which is described in chapter II) to study both elastic and electric fields. $U_J^K(x;d)$ is the *J*-th Green's extended displacement and can be expressed as

$$U(x;d) = U^{\infty}(x;d) + \frac{1}{2\pi^2}\int_0^{\pi} \bar{A}G_1A^T d\theta \tag{5.2}$$

with

$$(G_1)_{IJ} = \frac{(\bar{B}^{-1}B)_{IJ}}{-\bar{p}_I x_3 + p_J d_3 - [(x_1 - d_1)\cos\theta + (x_2 - d_2)\sin\theta]} \tag{5.3}$$

Follow the same instruction in chapter IV, we approximate the surface of QD with a number of flat triangles and carry out the integration of the half-space Green's function over these triangles.

The integration of the complementary part over a flat triangle Δ can be expressed as

$$u_K(d) = C_{iJLm}\gamma_{Lm}^{*}n_i\int_{\Delta}(\frac{1}{2\pi^2}\int_0^{\pi} \bar{A}G_1A^T d\theta)d\Delta(x) \tag{5.4}$$

In order to find the extended strain, we take the derivatives of Eq. (5.1) with respect to the observation point ***d*** to obtain the QD induced strain field

$$\gamma_{kp}(d) = \frac{1}{2}\gamma^*_{Lm} C_{iJLm} \int_{\partial V} [U^k_{J,d_p}(x;d) + U^p_{J,d_k}(x;d)] n_i(x) dS(x) \tag{5.5}$$

and electric field

$$E_p(d) = \gamma^*_{Lm} C_{iJLm} \int_{\partial V} U^4_{J,d_p}(x;d) n_i(x) dS(x) \tag{5.6}$$

5.3 Results and Discussion

We now apply the above analytical solutions to investigate the elastic and electric fields induced by a buried QD within the AlN half-space substrate. We consider two different growth orientations: one is AlN (0001) growing along the (0001) axis and the other is AlN (1000) growing along the polar direction. The material parameters used are taken from [Jog01]. The boundary condition is assumed to be traction free on surface and the misfit strains are $\gamma^*_{xx} = \gamma^*_{yy} = 0.1375$, $\gamma^*_{zz} = 0.1267$ in AlN (0001), and $\gamma^*_{xx} = 0.1267$, $\gamma^*_{yy} = \gamma^*_{zz} = 0.1375$ in AlN (1000). A schematic 3D view of an AlN QD is shown in Fig. 5.1(a) with its cross section in *x*-*y* plane shown in Fig. 5.1(b). The QD size is determined by the top and base diameters of the pyramid, R_b=8.5nm and R_t=4nm. h=4.1nm is the QD height and d=6.9nm is the distance between top of QD and half space surface. The size of the QD is taken from experimental values [Arl99].

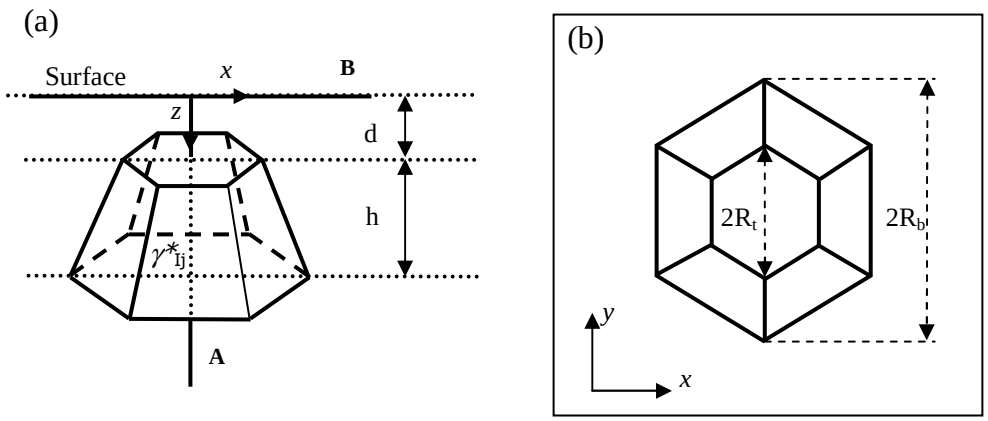

Figure 5.1 Schematic diagrams of hexagonal truncated-pyramidal QD showing dot shape and geometrical parameters. (a) 3D view of a single QD buried under half space substrate. Lines A and B parallel to *z*-axis and x-axis, respectively, denote two of the lines along which the strain field has been plotted; (b) View of the QD structure in *x*-*y* plane.

Before looking at multiple dots, a single isolated hexagonal truncated-pyramidal dot is studied to facilitate comparison with previously published calculations for point dot. The strain field on the surface is an important part of the overall structure, as it can provide valuable insights into the understanding of the growth of subsequent layer of QDs. Shown in the Fig. 5.2 are the contour plots of hydrostatic strain on the surface of substrates AlN (0001) and AlN (1000) due to a buried hexagonal truncated-pyramidal QD as described above. From Fig. 5.2, one can notice that the hydrostatic strain distributions are symmetric about the *z*-axis and the surface is highly strained. Directly above the QD, the AlN is under a large tensile strain.

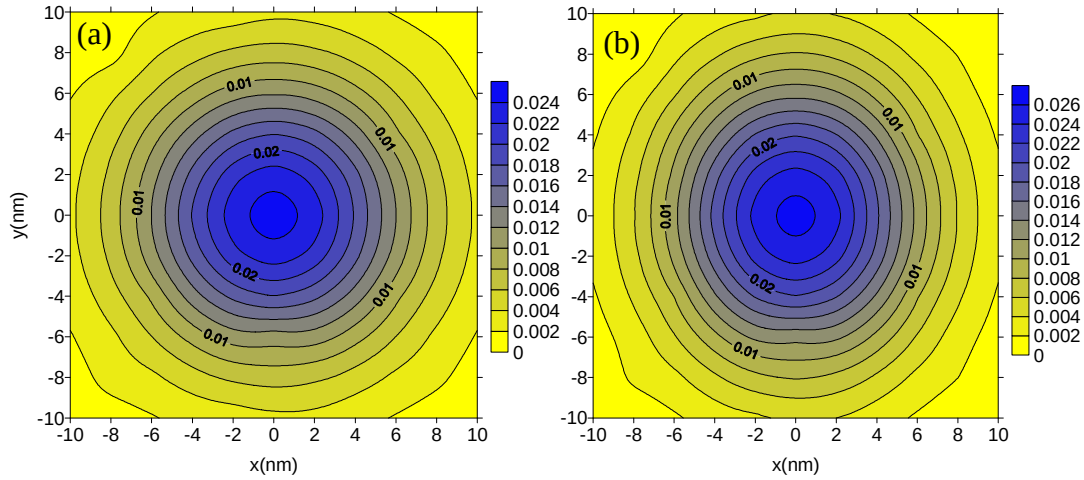

Figure 5.2 (a) Contour of the hydrostatic strain on the surface of AlN (0001) due to a hexagonal truncated-pyramidal QD. (b) Contour of the hydrostatic strain on the surface of AlN (1000) due to a hexagonal truncated-pyramidal QD.

Figs. 5.3(a) and (b) show, respectively, the contours of piezoelectric potential on the surface of substrate AlN (0001) and (1000) due to the same hexagonal truncated-pyramidal QD. It is observed that the contour of piezoelectric potential on the surface of AlN (0001) is rotationally symmetric about the *z* axis, and exhibits a large potential well in the center, which will contribute to the lateral carrier confinement in the dot, while the potential on the surface of AlN (1000) is symmetric about *x* axis but anti-symmetric about *y* axis. It can be also observed that the magnitude of potential on the surface of AlN (0001) is much larger than that on the surface of AlN (1000), i.e. 0.0065 VS. 0.0026. Those results in Figs. 5.2 and 5.3 are in good agreement with the previous published results for point QD [Pan03].

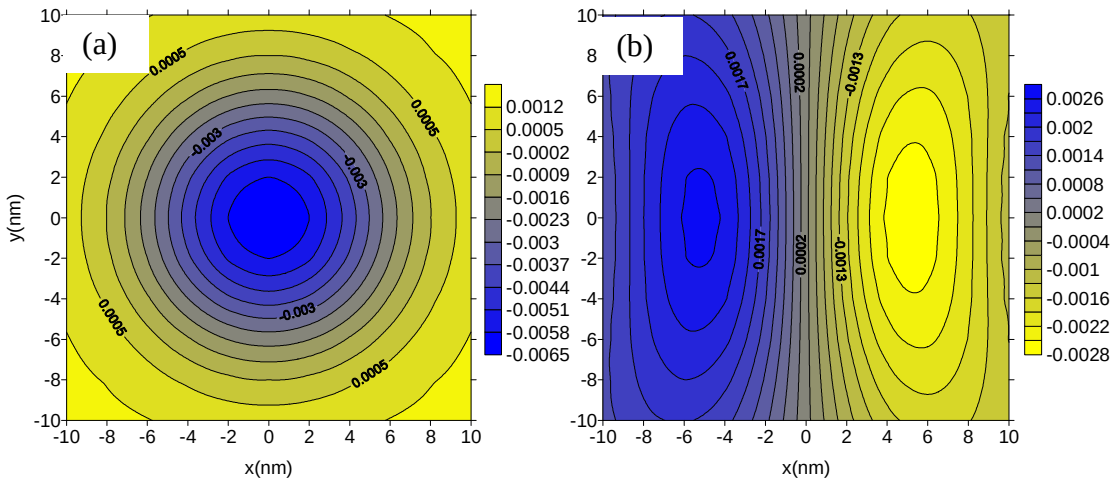

Figure 5.3 (a) Contours of the piezoelectric potential on the surface of AlN (0001) due to a hexagonal truncated-pyramidal QD. (b) Contours of the piezoelectric potential on the surface of AlN (1000) due to a hexagonal truncated-pyramidal QD.

The strain field γ_{xx}, γ_{yy} and γ_{zz} variation along line A of Fig. 5.1(a) are shown in Fig. 5.4(a). From Fig. 5.4(a), it is seen that γ_{xx}= γ_{yy}, which is because of rotational symmetry along line A. Generally, inside the QD, the forces are exerted primarily in the *x*-*y* plane. As the substrate tries to force the QD lattice constant to approach that of substrate, it induces compressive strains in the *x*-*y* plane and tensile strains along *z* axis. The signs of the strains are reversed in the surrounding substrate because of the opposing forces. These results are reflected in both Figs. 5.4(a) and (b), where 5.4(b) shows the strain variation along the surface line B of Fig. 5.1(b). From Fig. 5.4(b), we can see that γ_{xx}, γ_{yy} reach maximum directly above the top of QD which makes this location to be the most favorite for the incoming adatoms to nucleate. The maximum values of γ_{xx} and γ_{yy} are equal to each other due to the rotational symmetry. It is also observed that γ_{yy} does not remain tensile along the entire line. It changes sign and becomes compressive away from the top of QD due to energy conservation.

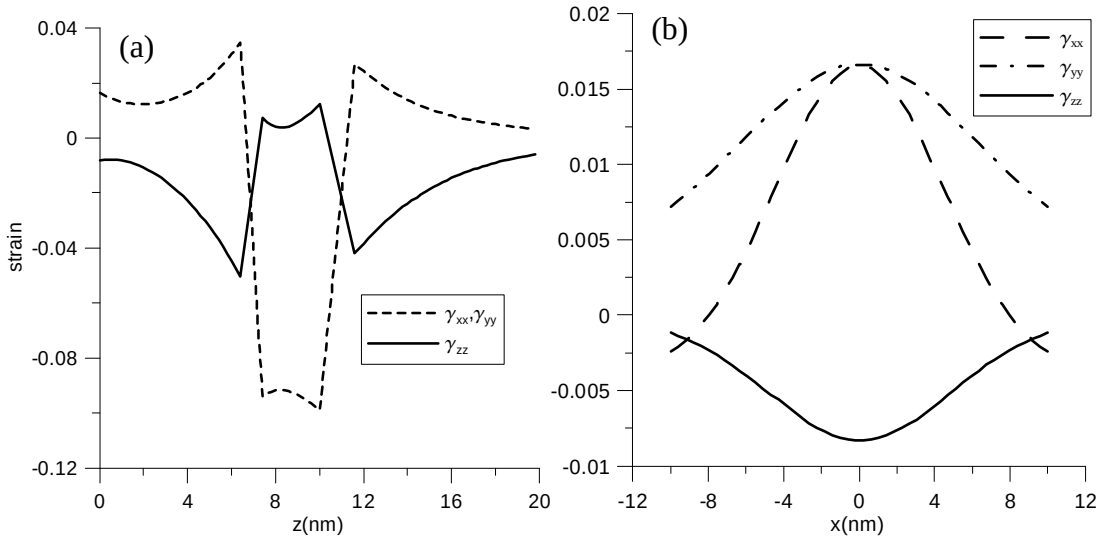

Figure 5.4 Line scans strain distributions in AlN (0001) along vertical line A (a) and surface horizontal line B (b) in Fig. 5.1.

The contours of piezoelectric potential in the *x*-*z* plane (*y*=0) due to the same hexagonal truncated-pyramidal QD are visualized in Fig. 5.5. The blue (or dark) areas show regions of low potential and the yellow (or light) areas regions of higher potential. It can be seen that there is a large potential well created by the potential difference between the pyramid base and top in AlN (0001) while large potential well shows along the left and right side in AlN (1000). The vertical profile of potential in AlN (1000) is anti-symmetric about *z* axis. We can also see that the potential in both structures are in same magnitude, unlike the potential on the surface in Fig. 5.3.

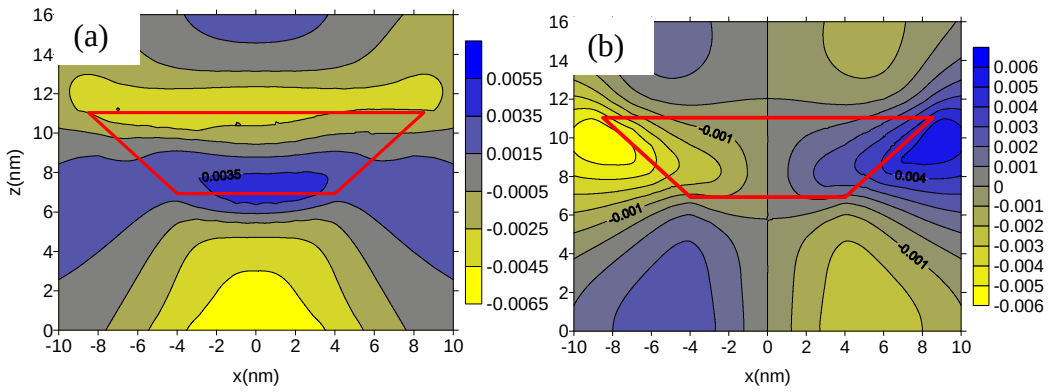

Figure 5.5 Contours of piezoelectric potential in the *x*-*z* plane (*y*=0) in (a) AlN (0001) (b) AlN (1000) half-space structures. The down trapezoid show the vertical profile of hexagonal truncated-pyramidal QD.

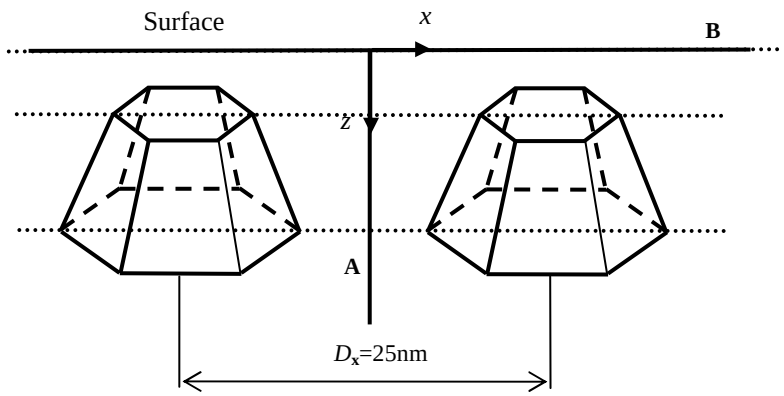

Figure 5.6 Schematic diagrams of two coupled hexagonal truncated-pyramidal QDs. D_x=25nm is the distance between the center of two QDs.

Fig. 5.7(a) shows strain distribution along the *z*-axis shown in Fig. 5.6. As we can see, γ_{xx} is compressive while γ_{yy} is tensile along the entire line. Fig. 5.7(b) shows strain distribution along the *x*-axis on the surface. It can be observed again that γ_{xx} does not remain tensile along the whole line. It is also noted that, unlike the single dot case, the maximum value of γ_{xx} is no longer equal to that of γ_{yy}, which means the rotational symmetry for a single dot along *x*-axis does not hold for multiple dots.

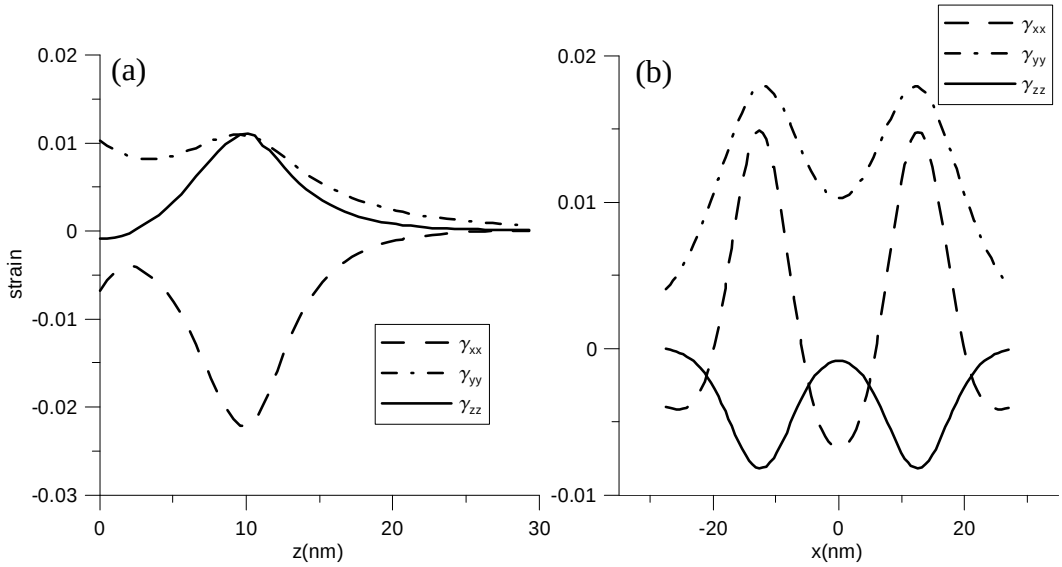

Figure 5.7 Line scans strain distributions in AlN (0001) structures due to coupled QDs along vertical line A (a) and surface horizontal line B (b) in Fig.5.6.

Figs. 5.8(a) and (b) show, respectively, the contours of piezoelectric potential on the surface of substrate AlN (0001) and (1000) due to the pair of QDs. It is observed that the contour of piezoelectric potential on the surface of AlN (0001) is no longer rotationally symmetric in the regions directly above the QD. It is further observed from Fig. 5.8(b) that a large potential well is created between the two QDs.

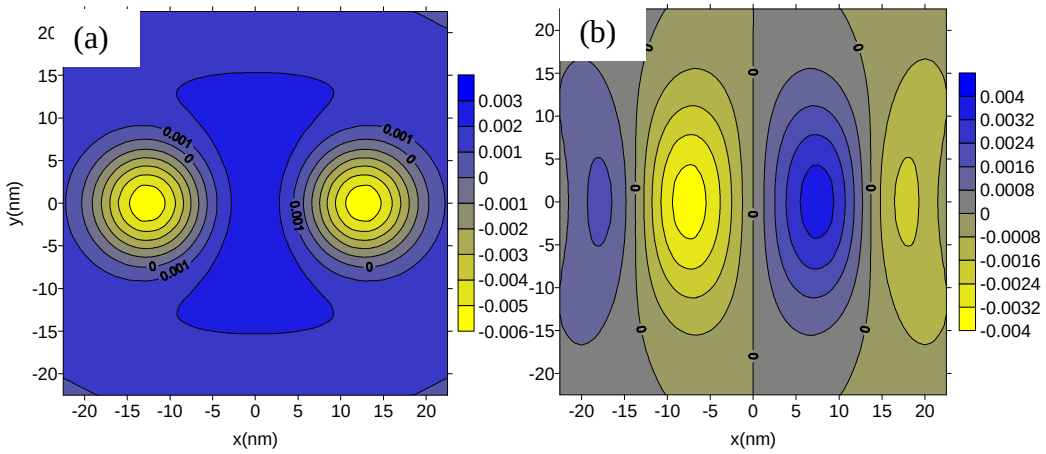

Figure 5.8 (a) Contours of the electric potential on the surface of AlN (0001) due to two hexagonal truncated-pyramidal QDs. (b) Contours of the electric potential on the surface of AlN (1000) due to two hexagonal truncated-pyramidal QD.

5.4 Conclusion

In this chapter, a detailed theoretical calculation of the strain and piezoelectric fields in and around nitride-based quantum dots buried in anisotropic half-space substrate is presented. The method is applied to study a specific example, AlN QDs in shape of hexagonal truncated-pyramidal. First, we present strain and electric potential distributions on the surface induced by single QD and compare the results with previous published ones for point QD. Good agreements are achieved. The vertical profile of piezoelectric potential in single QD, as well as the strain and potential in a pair of QDs is also studied. We find that the pair of QDs can affect the symmetry existed in isolated single QD and also the large piezoelectric potential leads to a strong lateral confinement in the QDs.

CHAPTER VI

CONCLUSIONS AND FUTURE WORK

6.1 Conclusion and Contributions

In this study, the elastic and electric fields in or around QWR embedded in anisotropic full-plane and QWR free-standing/embedded in bimaterial-plane are investigated by novel Green's functions and BEM. The strain energy on the free surface of half-space substrate induced by cubic, pyramidal, truncated pyramidal or point QD is also studied analytically. The main conclusions and contributions are summarized as following:

1. An accurate BEM modeling is presented for the strain and electric fields analysis in QWR structures. From this study, some important features are observed.
    1) Both the inclusion and inhomogeneity models predict very close strain field in the substrate far away from the QWR.
    2) For points inside or close to the QWR, the strain difference between the inclusion and inhomogeneity models can be as high as 10%, which can result in strong variations of the confined electronic states.
    3) The magnitude of strain inside the QWR is much larger than that outside, whilst the electric fields have the same magnitudes both inside and outside the QWR.

4) While the difference in the electric fields between the inclusion and inhomogeneity models is small in the nitride based system (InN/AlN), that in the InAs/GaAs (111) can be large.

5) It is observed that the electric fields in the QWR depend strongly on the QWR geometry shape. The electric field in triangle and square QWRs is sharply different from those in the polygons made of more than 4 sides.

2. The bimaterial Green's functions in anisotropic elastic media in terms of the Stroh formalism are derived. It is then applied to calculate the strain energy density and the relative strain energy in InAs (111) free-standing QWR or in QWR embedded in GaAs (111) substrate. Several interesting features are found:

   1) For the case of an isosceles triangle of InAs QWR on the substrate, the strain energy density within the QWR strongly depends on the base angle of the triangle.

   2) The magnitude of the relative strain energy for the case of an isosceles triangle QWR on the substrate increases with increasing base angle.

   3) For a square QWR either free standing on or embedded in the substrate, the magnitude of the relative strain energy increases with increasing depth of the QWR in the substrate, which represents the competition between the surface and bulk energies.

3. An analytical method for calculating the QD-induced strain fields in half-space semiconductor substrates is developed. The QD is assumed to be of any polyhedral shape which can be efficiently approximated by a number of flat triangles. We studied cubic, pyramidal, truncated pyramidal and point QDs within the GaAs (001) and GaAs (111) half-space substrates. It can be concluded that the shape of the QDs

has apparent influence on the strain energy distribution on the surface, so is the depth of the QDs.

4. A detailed theoretical calculation of the strain and piezoelectric fields in and around nitride-based quantum dots buried in anisotropic half-space substrate is presented. AlN QDs in shape of hexagonal truncated-pyramidal is studied. We find that the coupled QDs can affect the symmetry existed in isolated single QD and also the large piezoelectric potential leads to a strong lateral confinement in the QDs.

These results should be extremely useful in control of the QWR shape and size in epitaxial growth and simulating QWR semiconductor structures, and in the overgrowth of QDs on the substrate where the long-range strain energy on the surface plays an important role in controlling the new QD patterns and shapes.

6.2 Recommendations for Future Research

Self-assembled QDs can be grown layer by layer to form ordered nanostructures. Variations in sizes and shapes of self-assembled QDs have been a critical issue for device applications. Multi-layering of self-assembled QDs can provide a possible route for improving the size uniformity and lateral order of the dots. Theoretically as well as experimentally, in multilayer system, the elastic interaction of dots can lead to the formation of long-range spatial correlations, which may lead to a lateral ordering and size homogenization of the dots. This self-organization arises from the preferred nucleation of the islands at the local minima of the strain energy on the surface that is induced by previously buried dots.

In multi-layered system, different types of vertical correlations have been observed. Wang et.al. [Wan04] studied the vertical correlation (Figure 6.1a) and anticorrelation (Figure 6.1b) as a function of the spacer layer thickness, where vertical anticorrelation means that the subsequent QDs stack in the space between the underlying QDs and but not vertically aligned with the islands below. Springholz et.al. [Spr01] treated buried islands as point-like defects and observed the ABAB…stacking (Figure 6.2a) and ABCABC…stacking (Figure 6.2b) for different materials. They also concluded that the type of vertical stacking crucially depends on the elastic anisotropy of the matrix material as well as on the growth orientation.

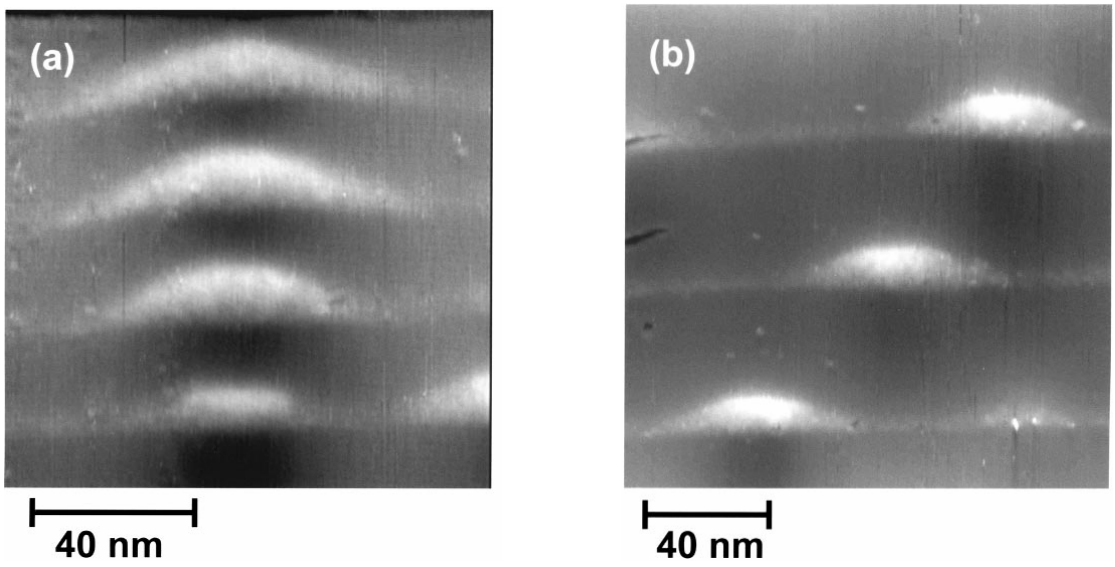

Figure 6.1 Cross-sectional STM images of the $In_{0.5}Ga_{0.5}As$ QDs. (a) A column of correlated QDs in the 75 ML region and (b) an array of anticorrelated QDs in the 150 ML region.

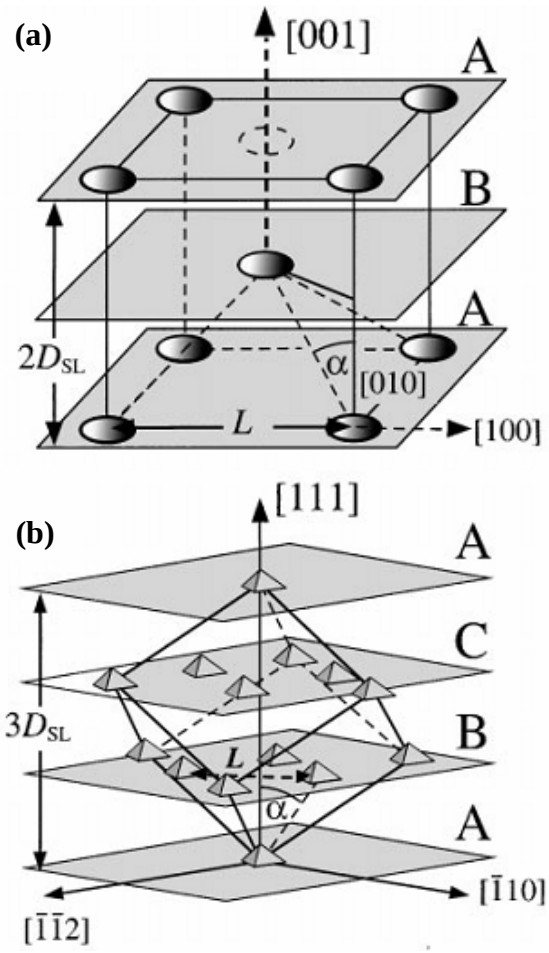

Figure 6.2 Schematic illustration of the possible 3D dot arrangement in self-organized dot superlattices (a) Centered tetragonal arrangement for the SiGe/Si (100) growth orientation, (b) trigonal dot arrangement with ABCABC: : : dot stacking for the PbSe/PbEuTe (111) growth orientation.

We have already carried out part of this research. Using our exact closed-form Green's function and taking integral over all the QDs surface, we calculated the strain energy density on the half-space surface induce by 2x2 QD arrays in InAs/GaAs (001) or (111) system. The QD is assumed to be cubic and has a size of 10x10x5 (Figure 6.3).

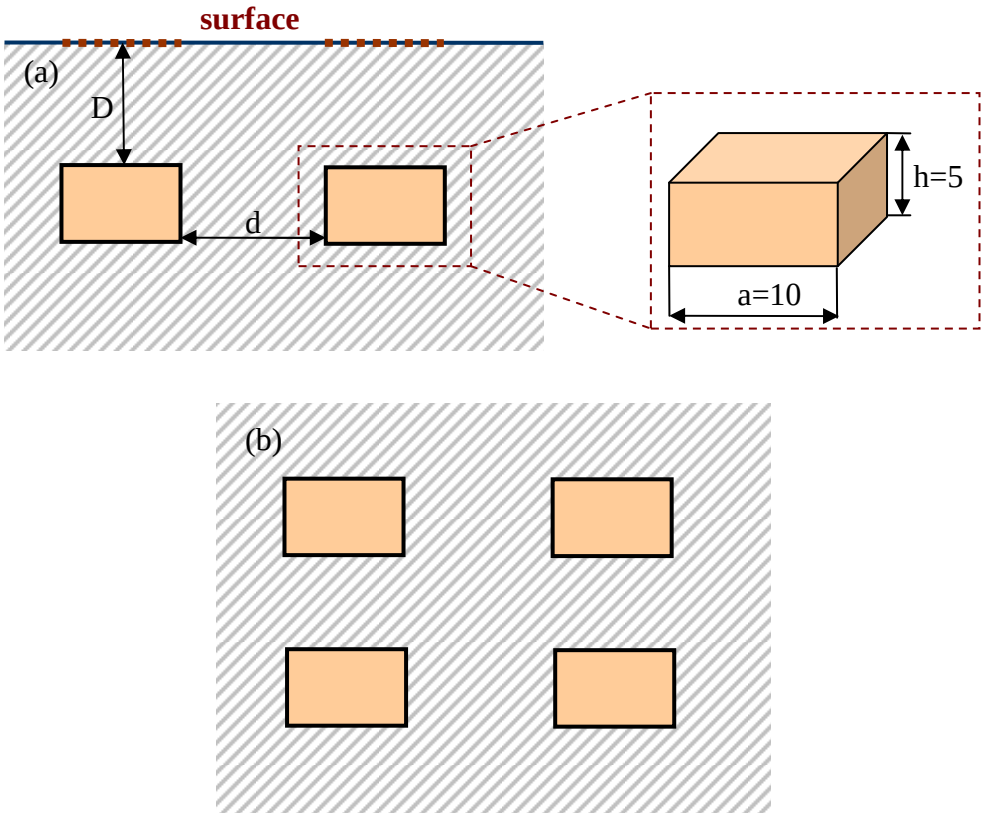

Figure 6.3 2 by 2 QD arrays in (a) *x*-*z* plane and (b) *x*-*y* plane

Figure 6.4 shows the strain energy density on the surface in both (001) and (111) systems. The inter-distance between QDs is d=10. The red squares show the location the buried QDs when looking topdown. We can observe that when the depth D is equal to 2, the preferred nucleation of the islands will be located exactly above the buried islands, as shown in Figures 6.4a and 6.4b; when the depth D is increased to 20, the preferred location for new QDs will be at the space between the buried islands, which means there would be a vertical anticorrelation, as shown in Figures 6.4c-6.4d.

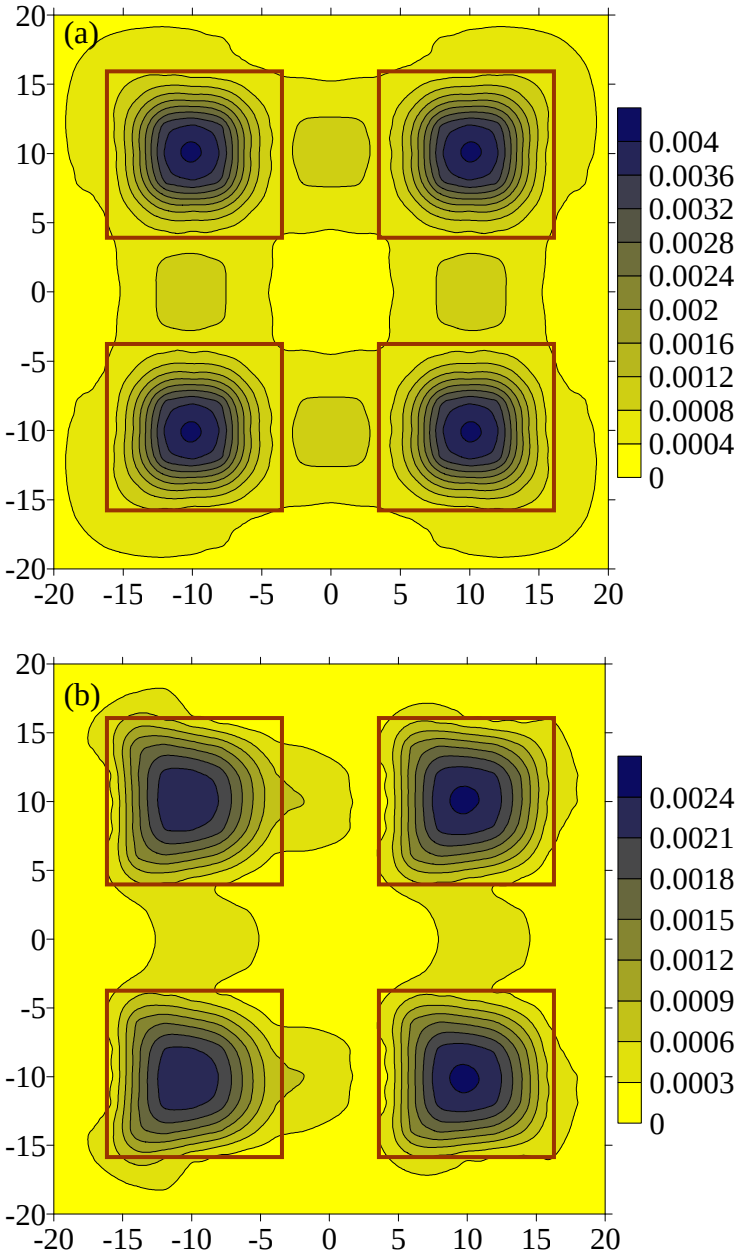
(a)
20
15
10
5
0
-5
-10
-15
-20
-20 -15 -10 -5 0 5 10 15 20
0.004
0.0036
0.0032
0.0028
0.0024
0.002
0.0016
0.0012
0.0008
0.0004
0
(b)
20
15
10
5
0
-5
-10
-15
-20
-20 -15 -10 -5 0 5 10 15 20
0.0024
0.0021
0.0018
0.0015
0.0012
0.0009
0.0006
0.0003
0

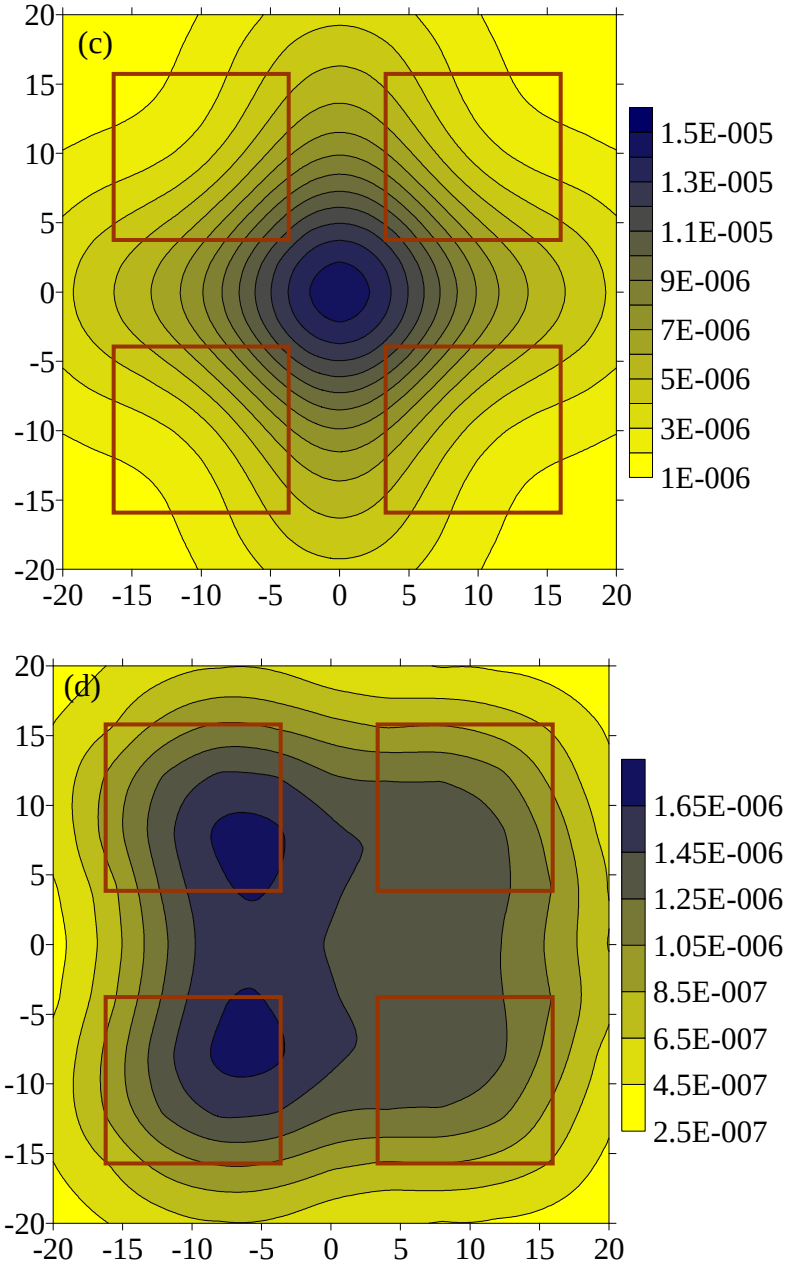

Figure 6.4 Strain energy density contour on the free surface. a) (001) direction, D=2; b) (111) direction, D=20; c) (001) direction, D=2; d) (111) direction, D=20.The distance between QDs is d=10.

If we the inter distance d between the QDs is decreased to 5, then when the depth of the QDs D=15, we can also observe the vertical anticorrelation (Table 6.1). It can thus be concluded that the vertical correlation and anticorrelation are function of the spacer layer thickness.

It is hoped that more calculation will be carried out on the elastic and electric fields induced by larger arrays QDs, such as 4x4 and 10x10 arrays within the multilayered QD systems.

Table 6.1 The QD depth D and inter distance between QDs when forming vertical anticorrelation

d (inter distance between QDs)	5	10
D (QD depth)	15	20

REFERENCES

[And99] Andreev, A. D.; Downes, J. R.; Faux, D. A.; O'Reilly, E. P., 1999. Strain distributions in quantum dots of arbitrary shape. *J. Appl. Phys.*, vol. 86, pp. 297-305.

[And00] Andreev, A. D.; O'Reilly, E. P., 2000. Theory of the electronic structure of GaN/AlN hexagonal quantum dots. *Physical Review B*, Vol. 62, pp. 15851-15870.

[Arl99] Arley, M.; Rouviere, J. L.; Widmann, F.; Daudin, B.; Feuillet, G.; Mariette, H., 1999. Quantitative characterization of GaN quantum-dot structures in AlN by high-resolution transmission electron microscopy. *Applied Physics Letters*, vol. 74, pp. 3287-3289.

[Bar75] Barnett, D.M.; Lothe, J., 1975. Dislocations and line charges in anisotropic piezoelectric insulators. *Phys Stat Sol B*, vol. 67, pp.105–111.

[Bax05] Baxter, J. B.; Aydil, E. S., 2005. Epitaxial growth of Zn0 Nanowires on a- and c-plane sapphire. *J. Cryst. Growth*, vol. 274, pp. 407-411.

[Ben96] Benabbas, T.; Francois, P.; Androussi, Y.; Lefebvre A., 1996. Stress relaxation in highly strained InAs/GaAs structures as studied by finite element analysis and transmission electron microscopy. *J. Appl. Phys.*, vol. 80, pp. 2763-2767.

[Bim98] Bimberg, D.; Grundmann, M.; Ledentsov, N.N., 1998. Quantum dot heterostructures. *Wiley, New York*.

[Bre92] Brebbia, C. A.; Dominguez, J., 1992. Boundary Elements: An Introductory Course. *Computational Mechanics Publications, Southampton*.

[Cal00] Califano, M.; Harrison P., 2000. Presentation and experimental validation of a single-band, constant-potential model for self-assembled InAs/GaAs quantum dots. *Phys. Rev. B*, vol. 61, pp. 10959-10965.

[Car95] Caro L. D.; Tapfer, L., 1995. Strain and piezoelectric fields in arbitrarily oriented semiconductor heterostructures. *Phys. Rev. B*, vol. 51, pp. 4381–4387.

[Con00] Constantin, C.; Martinet, E.; Leifer, K.; Rudra, A.; Lelarge, F.; Kapon, E.; Gayral, B.; Gerard, J.M., 2000. Strained V-groove quantum wires in multidimensional microcavities. *Mater. Sci. Eng. B*, vol. 74, pp. 158–164.

[Dar99] Daruka, I.; Tersoff, J.; Barabasi, A. L., 1999. Shape Transition in Growth of Strained Islands. *Physical Review Letters*, vol. 82, pp. 2753-2756.

[Dav98] Davies, J. H., 1998. Elastic and piezoelectric fields around a buried quantum dot: A simple picture. *Journal of Applied Physics*, vol. 84, pp. 1358-1365.

[Dav03] Davies, J. H., 2003. Elastic field in a semi-infinite solid due to thermal expansion or a coherently misfitting inclusion. *ASME J. Appl. Mech*., vol. 70, pp. 655-660.

[Din04] Ding, H. J.; Chen, W. Q.; Jiang, A. M., 2004. Green's functions and boundary element method for transversely isotropic piezoelectric materials. *Eng. Anal. Bound. Elements*, vol. 28, pp. 975-987.

[Dun93] Dunn, M. L.; Taya, M., 1993. An analysis of piezoelectric composite materials containing ellipsoidal inhomogeneities. *Proc R Soc Lond A*, vol. 443, pp. 265–287.

[Esh57] Eshelby, J. D., 1957. The determination of the elastic field of an ellipsoidal inclusion, and related problems, Proceedings of the Royal Society of London: Series A. *Mathematical and Physical Sciences*, vol. 241, pp. 376.

[Esh61] Eshelby, J. D., 1961. Elastic inclusions and inhomogeneities. *Prog. Solid Mech.*, vol. 2, pp. 89-140.

[Fau96] Faux, D. A.; Downes, J. R.; O'Reilly, E. P., 1996. A simple method for calculating strain distributions in quantum-wire structures. *J. Appl. Phys.*, vol. 80, pp. 2515-2517.

[Fer07] Ferdous, F.; Haque, A., 2007. Effect of elastic strain redistribution on electronic band structures of compressively strained GalnAsP/Inp membrane quantum wires. *J. Appl. Phys.*, vol. 101, pp. 093106-5.

[Fri07] Friedman, L. H., 2007. Anisotropy and order of epitaxial self-assembled quantum dots. *Phy. Rev. B*, vol. 75, pp. 193302-4.

[Gar05] Garcia, F.; Saez, A.; Dominguez, J., 2005. Anisotropic and piezoelectric materials fracture analysis by BEM. *Computers & Structures*, vol. 83, pp. 804-820.

[Gar07] Garcia, F.; Rojas-Diaz, R.; Saez, A.; Zhang, C. H., 2007. Fracture of magnetoelectroelastic composite materials using boundary element method (BEM). Theor. *Appl. Fract. Mech.*, vol. 47, pp. 192-204.

[Gia07] Giannopoulos, G. I.; Anifantis, N. K., 2007. A BEM analysis for thermomechanical closure of interfacial cracks incorporating friction and thermal resistance. *Comput. Meth. Appl. Meth. Eng.*, vol. 196, pp. 1018-1029.

[Gla01] Glas, F., 2001. Elastic relaxation of truncated pyramidal quantum dots and quantum wires in a half space: An analytical calculation. *J. Appl. Phys.*, vol. 90, pp. 3232-3241.

[Gla03] Glas, F., 2003. Elastic relaxation of a truncated circular cylinder with uniform dilatational eigenstrain in a half space. *Phys. Stat. Sol.*, vol. 237, pp. 599-610.

[Gos95] Gosling, T. J.; Willis, J. R., 1995. Mechanical stability and electronic-properties of buried strained quantum-wire arrays. *J. Appl. Phys.*, vol. 77, pp. 05601-05610.

[Gro05] Groh, U.; Kuna, M., 2005. Efficient boundary element analysis of cracks in 2D piezoelectric structures. *Int. J. Solids Struct.*, vol. 42, pp. 2399-2416.

[Gru95] Grundmann, M.; Stier, O.; Bimberg, D., 1995. InAs/GaAs pyramidal quantum dots: Strain distribution, optical phonons, and electronic structure. *Phy. Rev. B*, vol. 52, pp. 11969-11981.

[Hol99] Holy, V.; Springholz, G.; Pinczolits, M.; Bauer, G.,1999. Strain induced vertical and lateral correlations in quantum dot superlattices. *Physical Review Letters*, vol. 83, pp. 356-359.

[Jal05] Jalabert, D.; Coraux, J.; Renevier, H.; Daudin, B., 2005. Deformation profile in GaN quantum dots: Medium-energy ion scattering experiments and theoretical calculations. *Phy. Rev. B*, vol. 72, pp. 115301-5.

[Jia98] Jiang, H.; Singh, J., 1998. Strain Distribution and Electronic Spectra of InAs/GaAs Self-Assembled Dots: An 8-band Study. *Physical Review, B*, vol. 56, pp. 4696-4701.

[Jog00] Jogai, B., 2000. Three-dimensional strain field calculations in coupled InAs/GaAs quantum dots. *J. Appl. Phys.*, vol. 88, pp. 5050-5055.

[Jog01] Jogai, B., 2001. Three-dimensional strain field calculations in multiple InN/AlN wurtzite quantum dots. *Journal of Applied Physics*, vol. 90, pp. 699-704.

[Jon06] Jonsdottir, F.; Halldorsson D.; Beltz G. E.; Romanov A. E., 2006. Elastic fields and energies of coherent surface islands. *Modelling Simul. Mater. Sci. Eng.*, vol. 14, pp. 1167-1180.

[Kik01] Kikuchi, Y.; Sugii, H.; Shintani, K., 2001. Strain profiles in pyramidal quantum dots by means of atomistic simulation. *J .Appl. Phys.*, vol. 89, pp. 1191-1196.

[Lee02] Lee, K. Y.; Kwak, S.G., 2002. Determination of stress intensity factors for bimaterial interface stationary rigid line inclusions by boundary element method. *Int. J. Fract.*, vol. 113, pp. 285-294.

[Lei03] Lei, J.; Wang, Y.S.; Gross, D., 2003. Dynamic interaction between a sub-interface crack and the interface in a bi-material: time-domain BEM analysis. *Arch. Appl. Mech.*, vol. 73, pp. 225-240.

[Lei04] Lei, J.; Wang, Y. S.; Gross, D., 2004. Time-domain BEM analysis of a rapidly growing crack in a bi-material. *Int. J. Fract*., vol. 126, pp. 103-121.

[Lei07] Lei, J.; Wang, Y. S.; Gross, D., 2007. Two dimensional numerical simulation of crack kinking from an interface under dynamic loading by time domain boundary element method. *Int. J. Solids Struct.*, vol. 44, pp. 996-1012.

[Leo93] Leonard, D.; Krishnamurthy, M.; Reaves, C. M.; Denbaars, S.P.; Petroff, P. M., 1993. Direct formation of quantum-sized dots from uniform coherent islands of InGaAs on GaAs surfaces. *Appl. Phys. Lett.*, vol. 63, pp. 3203-3205.

[Lev07] Levine, M. S.; Golovin, A. A.; Davis, S. H., 2007. Self-assembly of quantum dots in a thin epitalxial film wetting and elastic substrate. *Phy. Rev. B*, vol. 75, pp. 205312-11.

[Liu02] Liu, G. R.; Quek Jerry S. S., 2002. A finite element study of the stress and strain fields of InAs quantum dots embedded in GaAs. *Semicond. Sci. Technol.*, vol. 17, pp. 630-643.

[Lu06] Lu, Y. W.; Cai, L.; Liang, S., 2006. Strained and piezoelectric charactreristics of Nitride Quantum Dots. *Chin. Phys. Lett.*, Vol. 23, pp. 956-959.

[Mak01] Makeev, M. A.; Madhukar, A., 2001. Simulations of atomic level stresses in systems of buried Ge /Si islands. *Phys. Rev. Lett.*, vol. 86, pp. 5542-5545.

[Mal03] Malachia, A.; Kycia, S.; Medeiros-Ribeiro, G.; Magalhaes-Paniago, R.; Kamins, T. I.; Williams, R. S., 2003. 3D Composition of Epitaxial Nanocrystals by Anomalous X-ray Diffractions: Observation of a Si-Rich Core in Ge Domes on Si(100). *Physical Review Letters*, vol. 91, pp. 176101-4.

[Mat00] Matagne, P.; Leburton, J. P.; Destine, J.; Cantraine, G., 2000. Modeling of the Electronic Properties of Vertical Quantum Dots by the Finite Element Method. *Computer Modeling in Engineering & Sciences*, vol. 1, pp. 1-10.

[Med02] Medeiros, R.G., 2002. Epitaxial growth of strained nanocrystals. *Phys. Stat. Sol*, vol. 230, pp. 443–450.

[Mur87] Mura, T., 1987. Micromechanics of Defects in Solids. *Dordrecht: Martinus Nijhoff*.

[Not95] Notomi, M.; Hammersberg, J.; Weman, H.; Nojima, S.; Sugiura, H.; Okamoto, M.; Tamamura, T.; Potemski, M., 1995. Dimensionality effects on strain and quantum confinement in lattice-mismatched InAsxP1 _ x/InP quantum wires. *Phys. Rev. B*, vol. 52, pp.11147–11158.

[Pan99a] Pan, E.; Amadei, B., 1999. Boundary element analysis of fracture mechanics in anisotropic bimaterials. *Eng. Anal. Bound. Elements*, vol. 23, pp. 683-691.

[Pan99b] Pan, E., 1999. A BEM analysis of fracture mechanics in 2D anisotropic piezoelectric solids. *Eng. Anal. Bound. Elements*, vol. 23, pp. 67-76.

[Pan01] Pan, E.; Yang, B., 2001. Elastostatic fields in an anisotropic substrate due to a buried quantum dot. *J. Appl. Phys.*, vol. 90, pp. 6190-6196.

[Pan02a] Pan, E., 2002. Elastic and piezoelectric fields around a quantum dot: Fully coupled or semi-coupled model. *Journal of Applied Physics*, vol. 91, pp. 3785-3796.

[Pan02b] Pan, E., 2002. Elastic and piezoelectric fields in substrates GaAs (001) and GaAs (111) due to a buried quantum dot. *Journal of Applied Physics*, vol. 91, pp. 6379-6387.

[Pan02c] Pan, E., 2002. Mindlin's problem for an anisotropic piezoelectric half-space with general boundary conditions. *Proc. R. Soc. Lond. A*, vol. 458, pp. 181-208.

[Pan03] Pan, E.; Yang, B., 2003. Elastic and piezoelectric fields in a substrate AlN due to a buried quantum dot. Journal of Applied Physics, vol. 93, pp. 2435-2439.

[Pan04a] Pan, E., 2004. Eshelby problem of polygonal inclusions in anisotropic piezoelectric full- and half-planes. *Journal of the Mechanics and Physics of Solids*, vol. 52, pp. 567-589.

[Pan04b] Pan, E.; Jiang, X., 2004. Effect of QWR Shape on the Induced Elastic and Piezoelectric Fields. *Computer Modeling in Engineering & Sciences*, vol.6, pp. 77-90.

[Pan05] Pan, E.; Han, F.; Albrecht, J. D., 2005. Strain Fields in InAs/GaAs Quantum Wire Structures: Inclusion vs. Inhomogeneity. *Journal of Applied Physics*, vol. 98, pp. 013534-12.

[Pan07] Pan, E.; Albrecht, J. D.; Zhang, Y., 2007. Elastic and piezoelectric fields in quantum wire semiconductor structures – a boundary integral equation analysis. *Phys. Stat. Sol.*, vol. 244, pp.1925-1939.

[Pan08] Pan, E.; Zhang, Y; Chung, P.W.; Denda M., 2008. Strain energy on the surface of an anisotropic half-space substrate: effect of quantum-dot shape and depth. *CMES*, Vol. 841, pp. 1-11.

[Pao06a] Pao, C. W.; Srolovitz, D.J., 2006. Stress and morphology evolution during island growth. Phys. Rev. Lett., vol.96, pp. 186103.

[Pao06b] Pao, C. W.; Srolovitz, D.J., 2006. Atomistic simulation of stress evolution during island growth. *J. Mech. Phys. Solids*, vol.54, pp. 2527-2543.

[Pea00] Pearson, G. S.; Faux, D. A., 2000. Analytical solutions for strain in pyramidal quantum dots. *J. Appl. Phys.*, vol. 88, pp. 730-736.

[Pei03] Pei, Q. X.; Lu, C.; Wang, Y. Y., 2003. Effect of elastic anisotropy on the elastic fields and vertical alignment of quantum dots. *J. Appl. Phy.*, vol. 93, pp. 1487-1492.

[Pet03] Petroff, P. M., 2003. Epitaxial growth and electronic structure of self-assembled quantum dots. *Top. Appl. Phys.*, vol. 90, pp. 1-25.

[Phi01] Phillips, R., 2001. Crystals, Defects, and Microstructures: Modeling Across Scales. *New York: Cambridge University Press*.

[Qin05] Qin, Q. H., 2005. 2D Green's functions of defective magnetoelectroelastic solids under thermal loading. *Eng. Anal. Bound. Elements*, vol. 29, pp. 577-585.

[Pry98] Pryor, C.; Kim, J.; Wang, L. W.; Williamson, A. J.; Zunger, A., 1998. Comparison of two methods for describing the strain profiles in quantum dots. *J. Appl. Phys.*, vol. 83, pp. 2548-2554.

[Rea07] Read, D. T.; Tewary, V. K., 2007. Multiscale model of near-spherical germanium quantum dots in silicon. *Nanotechnology*, vol. 18, pp.105402-12.

[Ros98] Ross, F. M.; Tersoff, J.; Tromp, R. M., 1998. Coarsening of Self-Assembled Ge Quantum Dots on Si (001). *Physical Review Letters*, vol. 80, pp. 984-987.

[Ru00] Ru, C.Q., 2000. Eshelby's problem for two-dimensional piezoelectric inclusions of arbitrary shape. *Proceedings of the Royal Society of London*, vol. 456, pp. 1051-1068.

[Sal03] Salvadori, A., 2003. A symmetric boundary integral formulation for cohesive interface problems. *Computational Mechanics*, vol. 32, pp. 381-391.

[She04] Shen, S. P.; Atluri, S. N., 2004. Multiscale Simulation Based on the Meshless Local Petrov-Galerkin (MLPG) Method. *Computer Modeling in Engineering & Sciences*, vol. 5, pp. 235-255.

[Smi86] Smith, D. L., 1986. Strain-generated electric fields in [111] growth axis strain-layer superlattices. *Solid State Commun*, vol.57, pp. 919-930.

[Spr01] Springholz G.; Pinczolits M.; Holy V.; Zerlauth S.; Vavra I.; Bauer G., 2001. Vertical and lateral ordering in self-organized quantum dot superlattices. *Physica E*, vol. 9, pp. 149-163.

[Sta04] Stangl, J.; Holy, V.; Bauer, G., 2004. Structural properties of self-organized semiconductor nanostructures. *Rev. Mod. Phys.*, vol. 76, pp.725-783.

[Sun06] Sun, Y.; Zhang, Z.; Kitipornchai, S.; Liew, K. M., 2006. Analyzing the interface between collinear interfacial cracks by an efficient boundary element-free method. *Int. J. Eng. Sci.*, vol. 44, pp. 37-48.

[Tew04a] Tewary, V. K., 2004. Multiscale Green's-function method for modeling point defects and extended defects in anisotropic solids: Application to a vacancy and free surface in copper. *Phys. Rev. B*, vol. 69, pp. 094109-13.

[Tew04b] Tewary, V. K.; Read, D. T., 2004. Integrated Green's Function Molecular Dynamics Method for Multiscale Modeling of Nanostructures: Application to Au Nanoisland in Cu. *Computer Modeling in Engineering & Sciences*, vol. 6, pp. 359-372.

[Tin96] Ting, T. C. T., 1996. Anisotropic Elasticity: Theory and Applications. *New York: Oxford University Press*.

[Wan04] Wang, X.D.; Liu N.; Shih C.K., 2004. Spatial correlation-anticorrelation in strain-driven self-assembled InGaAs quantum dots. *Appl. Phys. Letters*, vol. 85, pp. 1356-1358.

[Wan06] Wang, C. Y.; Denda, M.; Pan, E., 2006. Analysis of quantum-dot-induced strain and electric fields in piezoelectric semiconductors of general anisotropy. *International Journal of Solids and Structures*, vol. 43, pp. 7593-7608.

[Yan02] Yang, B.; Pan, E., 2002. Elastic Analysis of an Inhomogeneous Quantum Dot in Multilayered Semiconductors Using a Boundary Element Method. *Journal of Applied Physics*, vol. 92, pp. 3084-3088.

[Yan03a] Yang, B.; Pan, E., 2003. Elastic fields of quantum dots in multilayered semiconductors: A novel Green's function approach. *Journal of Applied Mechanics*, vol. 70, pp. 161-168.

[Yan03b] Yang, B.; Tewary, V. K., 2003. Formation of a surface quantum dot near laterally and vertically neighboring dots. Phys. Rev. B, vol. 68, pp. 035301.

[Yan05] Yang, B.; Tewary, V. K., 2005. Green's function-based multiscale modeling of defects in a semi-infinite silicon substrate. *International Journal of Solids and Structures*, vol. 42, pp. 4722-4737.

[Zha05] Zhang, X.; Sharma, P., 2005. Size Dependency of Strain in Arbitrary Shaped, Anisotropic Embedded Quantum Dots due to Nonlocal Dispersive Effects. *Physical Review B*, vol. 72, pp. 195345-16.

[Zhu06] Zhu, R.; Pan, E.; Chung, P. W.; Cai, X.; Liew, K. M.; Buldum, A., 2006. Atomistic Calculation of Elastic Moduli in Strained Silicon. *Semiconductor Science and Technology*, vol. 21, pp. 906-911.